

Department of Physics  
Indian Institute of Technology Guwahati  
Ph.D. Thesis



# Quantum Phases of Constrained Bosons in Low Dimensions

Sayan Lahiri

Thesis Supervisor: Dr. Tapan Mishra  
January, 2021



# Quantum Phases of Constrained Bosons in Low Dimensions

A

Thesis Submitted

in Fulfillment of the Requirements

for the Degree of

PHD

By

**SAYAN LAHIRI**

Under the Supervision of **Dr. TAPAN MISHRA**



Department of Physics

Indian Institute of Technology Guwahati

January, 2021



©Sayan Lahiri

# Declaration

This is to certify that the thesis entitled “**Quantum Phases of Constrained Bosons in Low Dimensions**”, submitted by me to the *Indian Institute of Technology Guwahati*, for the award of the degree of PhD, is a bonafide work carried out by me under the supervision of Dr. Tapan Mishra. The content of this thesis, in full or in parts, have not been submitted to any other University or Institute for the award of any degree or diploma. I also wish to state that to the best of my knowledge and understanding nothing in this report amounts to plagiarism.

Signed: \_\_\_\_\_

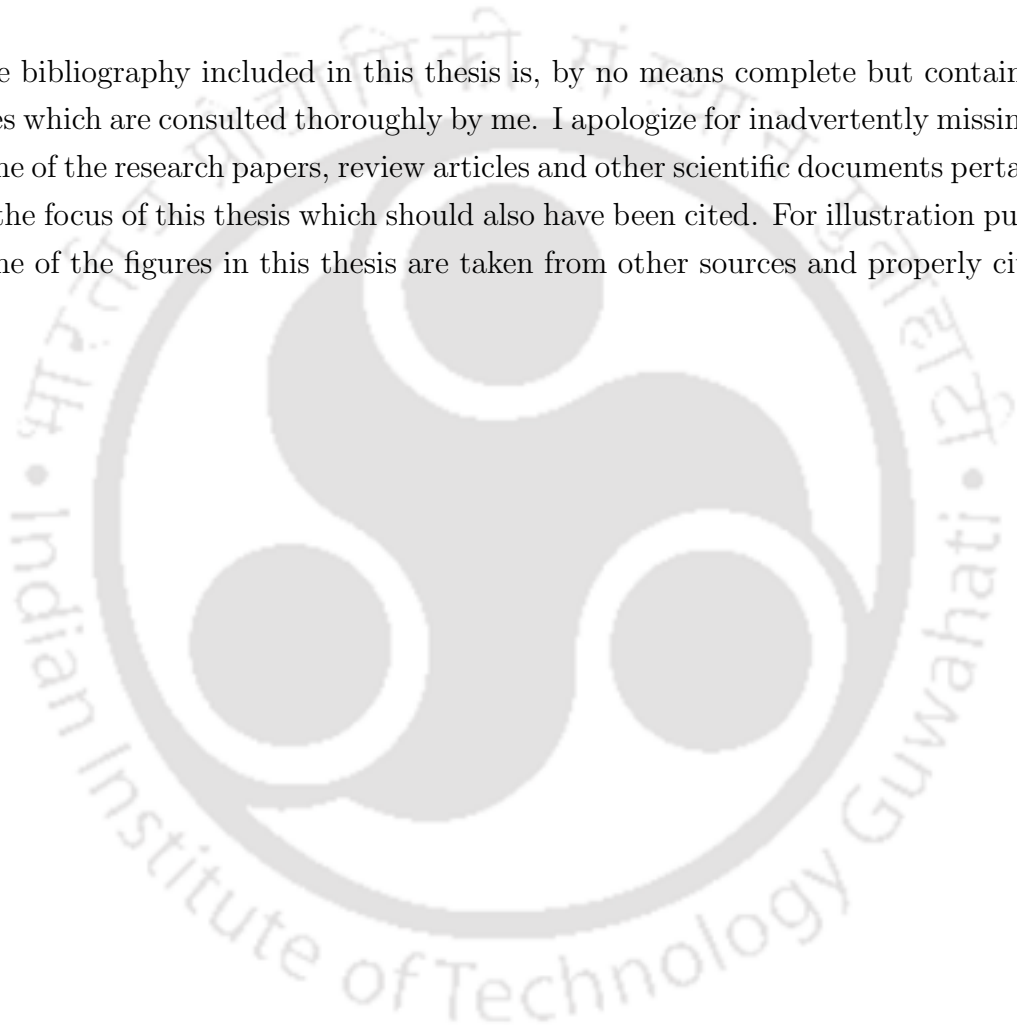
**Sayan Lahiri**  
Department of Physics,  
Indian Institute of Technology Guwahati,  
Guwahati-781039, Assam, India.

Date: \_\_\_\_\_



# Disclaimer

The bibliography included in this thesis is, by no means complete but contains the ones which are consulted thoroughly by me. I apologize for inadvertently missing out some of the research papers, review articles and other scientific documents pertaining to the focus of this thesis which should also have been cited. For illustration purpose some of the figures in this thesis are taken from other sources and properly cited.





# Certificate

This is to certify that the thesis entitled “**Quantum Phases of Constrained Bosons in Low Dimensions**”, submitted by Sayan Lahiri (166121102), a research scholar in the *Department of Physics, Indian Institute of Technology Guwahati*, for the award of the degree of PhD, is a record of an original research work carried out by him under my supervision and guidance. The thesis has fulfilled all requirements as per the regulations of the institute and in my opinion has reached the standard needed for submission. The results embodied in this thesis have not been submitted to any other University or Institute for the award of any degree or diploma.

Signed: \_\_\_\_\_

**Supervisor: Dr. Tapan Mishra**  
**Department of Physics,**  
**Indian Institute of Technology Guwahati,**  
**Guwahati-781039, Assam, India.**

Date: \_\_\_\_\_



*To my parents...*





# Acknowledgement

This thesis would not have been possible without the support of many people.. The list is endless, it is only possible to mention some of them.

I would like to express my sincere gratitude to my supervisor, Dr. Tapan Mishra, for his continuous guidance, support, enthusiasm and giving me freedom and motivation. I also thank him for introducing me to the collaborators and exciting new problems which helped me to learn and gain experience in the field of my research. His dedication, hard work and immense knowledge always inspire me to learn new things.

I wish to extend my special thanks to Dr. Manpreet Singh and Dr. Suman Mondal for collaborating in my projects and making them more effective and rich.

I would also like to show my deep appreciation to my doctoral committee members, Prof. Amarendra Kumar Sarma, Dr. Kanhaiya Pandey and Prof. Aditya Narayan Panda, for the useful suggestions and yearly evaluations of my research work. I acknowledge the academic help of HODs, Prof. Poulouse Poulouse, Prof. Subhradip Ghosh and Prof. Perumal Alagarsamy. I thank technical assistants, academic and non-academic staff of our department for various helps in my research period. I am also thankful to Param Ishan, IIT Guwahati for the supercomputer facility.

I gratefully acknowledge the support from our group members, Mrinal Kanti Giri, Ashirbad Padhan, Soumya Ranjan Padhi, Rajashri Parida and Biswajit Paul. I had wonderful learning sessions with them.

I am grateful for having beautiful friendships with Riajul, Rajesh, Subhajitda and Mandira. Also, during my Ph.D., I have learned a great deal of things from Dilip sir, Gagan sir, Charu sir, Bibhas sir, Debu sir, Uday sir and Saurabh Sir. I thank all my batch mates Rakesh, Manabendra, Dipti, Arghyajit, Pronoy, Samit, Sanket and Surojit for their friendship throughout the years. I also thank my juniors Shilpi, Sourav, Sahabub, Sudeshna, Gargi, Swarup, Soumen, Amit, Banashree, Sonali, Dipankar, Samik, Chinmoy, Lipika, Seshadri, Shantanu, Himanshu, Rajesh

---

and Sanu for supporting me in every possible way. I also like to mention some of my seniors Sunandoda, Aritrada, Ambareshda, Susmitadi, Srimoyda, Basabenduda, Krishnanjanda, Subhadeepda, Kallolda, Anirbanda, Rishavda, Nawazda and Sunilda for their guidance.

Last but not least, I want to thank my family specially my parents, Dr. Timir Kumar Lahiri and Mridula Lahiri for their love, support, sacrifices and patience.

January, 2021

Sayan Lahiri



# Abstract

Study of quantum phase transitions in artificial systems has attracted enormous attention in recent years. In this thesis, we study the quantum phase transitions in systems of constrained bosons in low dimensional lattices. We consider two different scenarios within this framework, (i) in the case of ultracold atoms in optical lattices and (ii) in the context of microwave photons in superconducting circuits. We have analyzed the ground state properties of such systems by using numerical methods such as the cluster mean-field theory (CMFT) approach and the density matrix renormalization group (DMRG) method.

We first explore the ground-state properties of a system of nonlocally coupled dipolar bosons in a bilayer optical superlattice by considering bosons in one layer to be of softcore in nature and separately allowing two- and three-body hard-core constraints on the other layer. We show how the presence of different constraints on bosons in one layer influences the overall phase diagram exhibiting various Mott insulator phases at incommensurate densities due to the presence of the superlattice potential apart from the usual Mott insulators at commensurate densities.

Then we investigate the quantum phase transitions of constrained bosons in a two-leg Bose-Hubbard ladder. We consider hardcore bosons in one leg and three-body constrained bosons in the other leg in the limit of two body attractive interaction. Here we find that depending on the ratio between the rung and leg hoppings of the bosons, rung insulator phases are stabilized at unit filling. Moreover, at incommensurate fillings we obtain signatures of the pair superfluid phase. We extend this work to the case where both the legs of the ladder have three-body constrained bosons with onsite two-body attractive interaction. We obtain the signatures of the dimer rung insulator phase apart from the pair superfluid phases.

In the last part of the thesis, we propose a method to achieve photon pair propagation in an array of three-level superconducting circuits. Assuming experimentally accessible three-level artificial atoms with strong anharmonicity coupled via microwave transmission lines in both one and two dimensions, we analyze the cir-

---

cuit quantum electrodynamics (QED) of the system. We explicitly show that, for a suitable choice of the coupling ratio between different levels, the single-photon propagation is suppressed, and the propagation of photon pairs emerges.



# List of Publications

## Publications included in the thesis

1. **Sayan Lahiri**, Suman Mondal, Manpreet Singh, Tapan Mishra, *Mott insulator phases of nonlocally coupled bosons in bilayer optical superlattices*, Phys. Rev. A **101**, 063624(2020).
2. **Sayan Lahiri**, Suman Mondal, Kanhaiya Pandey, Tapan Mishra, *Correlated photon pair propagation in circuit QED with superconducting processors*, Phys. Rev. A **102**, 043710 (2020).

## Schools/Workshops/Conferences attended

1. Attended *SERB School on Frontiers in Quantum Optics*, December 2017, Department of Physics, IIT Guwahati, India.
2. Attended *Recent Trends in Cold and Ultracold Matter*, March 2018, Department of Physics, IIT Guwahati, India.
3. Presented poster at, *2nd Annual conference on quantum condensed matter*, July 2019, Department of Physics, IISc Bangalore, India.
4. Presented talk at, *Young Investigators Meet on Quantum Condensed Matter Theory*, December 2020, NISER Bhubaneswar, India.



# Contents

List of publications	xiii
<b>1 Introduction</b>	<b>1</b>
1.1 Quantum phase transitions . . . . .	1
1.2 QPT in optical lattices . . . . .	2
1.3 Optical lattice . . . . .	2
1.3.1 Ultracold bosons in optical lattice: The Bose-Hubbard model . . . . .	5
1.3.2 Superfluid to Mott-insulator transition . . . . .	8
1.4 QPT in superconducting circuits . . . . .	11
1.4.1 Qubits . . . . .	12
1.4.2 Charge Qubit . . . . .	13
1.4.3 Circuit QED for transmons . . . . .	14
1.5 Chapterwise outline of the thesis . . . . .	18
<b>2 Methods</b>	<b>19</b>
2.1 Mean Field approach . . . . .	19
2.2 Cluster Mean-field Theory (CMFT) approach . . . . .	22
2.2.1 Exact Diagonalization (ED) . . . . .	24
2.3 Density matrix renormalization group (DMRG) . . . . .	26
<b>3 Mott insulator phases of non-locally coupled bosons in bilayer optical superlattices</b>	<b>29</b>
3.1 Introduction . . . . .	29
3.2 Method . . . . .	33
3.3 Results and Discussion . . . . .	35
3.3.1 Hardcore constraint for bosons in layer-B . . . . .	35
3.3.2 Three-body constraint for bosons in layer-B . . . . .	41
3.3.3 Phase diagram in one dimension . . . . .	45

## CONTENTS

---

3.4	Conclusions . . . . .	49
<b>4</b>	<b>Constrained bosons in two-leg Bose-Hubbard ladder</b>	<b>51</b>
4.1	Introduction . . . . .	51
4.2	Model and approach . . . . .	52
4.3	Results . . . . .	54
4.3.1	The HCB-TBC system . . . . .	54
4.3.1.1	CMFT results . . . . .	54
4.3.1.2	DMRG results . . . . .	57
4.3.2	The TBCs-TBCs system . . . . .	62
4.4	Conclusions . . . . .	63
<b>5</b>	<b>Correlated photon pair propagation in circuit QED with superconducting processors</b>	<b>67</b>
5.1	Introduction . . . . .	67
5.2	Model and method . . . . .	69
5.3	Results . . . . .	71
5.3.1	Phase diagram in 1D . . . . .	71
5.3.2	The PSF phase . . . . .	74
5.3.3	Phase diagram in 2D . . . . .	77
5.4	Conclusions . . . . .	79
<b>6</b>	<b>Conclusions and Future Directions</b>	<b>81</b>
6.1	Future Directions . . . . .	82
	<b>Bibliography</b>	<b>85</b>

# List of Figures

1.1	(a) Formation of an optical lattice by superimposing two laser beams. The nodes or antinodes of the optical lattice behaves as a periodic array for trapping the atoms. (b) Formation of a two dimensional lattice potential by the superimposition of three orthogonal standing waves. The figure is obtained from Ref. [1]. . . . .	4
1.2	Figure depicts the significance of different parameters in the BH model given in Eq. 1.16. . . . .	7
1.3	The mean-field phase diagram of the BH model (1.16) in $\mu/U - zt/U$ plane. Here MI(n) is the MI with density $n$ . . . . .	9
1.4	Experimental result of the first observation of SF-MI transition (taken from [2]). The figure shows the absorption images of matter-wave interference pattern for different initial states prepared for different lattice depth ( $V_0$ ). Here $V_0$ are, in (a) $0E_r$ , (b) $3E_r$ , (c) $7E_r$ , (d) $10E_r$ , (e) $13E_r$ , (f) $14E_r$ , (g) $16E_r$ and (h) $20E_r$ . . . . .	10
1.5	Schematic layout of superconducting circuits and its equivalent lumped circuit representation for implementing cavity QED using them [3]. . . . .	11
1.6	The charge qubit formed by the Josephson Junction (JJ) with charging energy $E_J$ and a capacitor $C$ . . . . .	13
1.7	Circuit diagram of a transmon qubit consisting of two JJs with capacitances $C_J$ and Josephson energy $E_J$ , a biasing capacitor $C_B$ and a gate capacitor $C_g$ connected to a resonator with capacitance $C_r$ and inductance $L_r$ . A voltage $V_g$ is applied to the circuit through the coupling capacitor $C_{in}$ [4] . . . . .	15
1.8	JCH model for two cavities representing the atomic transition operators $\sigma^+$ , $\sigma^-$ and photon hopping strength $\kappa$ . . . . .	16

LIST OF FIGURES

---

1.9 The mean-field phase diagram of superconducting circuits using transmon as a qubit (1.16) in  $\tilde{\mu} - \tilde{\kappa}$  plane. Here MI(n) is the MI lobes with  $n$  polaritons. . . . . 17

2.1 Division of a two-dimensional square lattice into  $2 \times 2$  clusters. A unit cluster is represented by a dotted box which by repeating in two dimensions forms the entire lattice. We apply the ED method for solid lines and MF approach for dashed lines. . . . . 23

2.2 MI-SF phase boundaries for two dimensional square lattice, calculated using SDMFT(black line), CMFT( $2 \times 2$ , red line), and the exact( $2 \times 2$ , blue and  $3 \times 3$ , green). . . . . 24

3.1 (a)Illustration of a bilayer superlattice having periodicity equal to two showing the intra-layer and inter-layer interactions. (b) The possible alignment of the dipoles in this bilayer system. In the inset we have shown one dipole placed in the origin in such a way that it makes an angle  $\phi$  with the  $x$  and  $y$  axes and  $\theta$  with the  $z$  axis. (c) Two leg optical superlattice with leg-A and leg-B containing the softcore bosons and constrained bosons respectively. These two legs interact among themselves via the non-local interaction  $U_{AB}$ . . . . . 31

3.2 The CMFT phase diagram when bosons in layer-A are softcore and in layer-B are HCBs. Here  $U_A = 80$  and  $U_{AB} = 40$ . . . . . 34

3.3 Variation of  $\rho$ (solid blue curve) and  $|\psi|^2$ (dashed green curve) with respect to  $\mu/t$  for  $\lambda = 10, 70, 140$  shows the gapped and gapless phases when layer-B has HCBs. The plateaus in  $\rho$  correspond to the gap in the MI phases whereas the shoulders around the plateaus (where the values of  $|\psi|^2$  are finite) indicate the gapless SF phase. We also plot the individual layer densities as  $\rho_A$ (dot dashed curve) and  $\rho_B$ (dotted curve) for clarity. Due to the hardcore nature  $\rho_B$  saturates at one. The fluctuations in  $\rho_A$  and  $\rho_B$  are due to the degenerate states in the CMFT calculation. . . . . 36

3.4 CMFT phase diagram in the  $\mu/t$  vs.  $U/t$  plane when bosons in layer-A are softcore and in layer-B are hardcore in nature. Here  $U_A = U = 80, U_{AB} = 40$  and  $\lambda = 60$ . Since  $U_A$  is fixed in the case, we vary  $t$  in order to tune the ratio  $U/t$ . . . . . 38

3.5 CMFT phase diagram when bosons in layer-A are softcore and in layer-B are TBCs. Here  $U_A = U_B = 80$  and  $U_{AB} = 40$ . . . . . 39

3.6	CMFT phase diagram in the $\mu/t$ vs. $U/t$ plane when bosons in layer-A are softcore and in layer-B are three-body constrained. Here $U_A = U_B = U = 80, U_{AB} = 40$ and $\lambda = 60$ . Since $U_A$ is fixed in the case, we vary $t$ in order to tune the ratio $U/t$ . . . . .	42
3.7	DMRG phase diagram when bosons in leg-A are softcore in nature and bosons in leg-B are HCBs. . . . .	43
3.8	DMRG phase diagram when bosons in leg-A are softcore in nature and bosons in leg-B are TBCs. . . . .	44
3.9	Finite size scaling of chemical potentials for $\rho = 1.5$ for different values of $\lambda$ corresponding to the phase diagram of Fig. 3.7 when bosons in leg-A are softcore in nature and bosons in leg-B are HCBs. The solid and dashed lines represent the fitted functions to $\mu^+$ and $\mu^-$ respectively. . . . .	46
3.10	Density distribution of the system when $\lambda = 12$ (top) and $\lambda = 28$ (bottom) for $\rho = 1.5$ corresponding to the phase diagram of Fig. 3.7. The black circles and red squares represent the density distribution of leg-A and leg-B respectively. . . . .	47
3.11	Density distribution of the system when $\lambda = 22$ (top) and $\lambda = 38$ (bottom) for $\rho = 1.75$ corresponding to the phase diagram of Fig. 3.8. The black circles and red squares represent the density distribution of leg-A and leg-B respectively. . . . .	48
4.1	Schematic diagram of a BH ladder with intraleg and interleg hoppings.	52
4.2	Phase diagram for HCB-TBC system in $\mu/ U  - J/ U $ plane using the CMFT method for $J_{\perp}/J = 3.0$ . . . . .	54
4.3	(a) $\rho, \rho_s$ vs $\mu$ plot, (b) and (c) are the single and pair correlations for bosons respectively along legwise and rungwise direction in a BH ladder using CMFT method for $J/ U =0.04$ . . . . .	56
4.4	Phase diagram of HCB-TBC system in $\mu/ U  - J/ U $ plane for different $J_{\perp}/J$ ratios. . . . .	57
4.5	DMRG phase diagrams for (a) $J_{\perp}/J = 1.0$ , (b) $J_{\perp}/J = 2.0$ and (c) $J_{\perp}/J = 3.0$ . The phase boundaries represent the extrapolated values of $\mu^+$ and $\mu^-$ (see text) with $L = 40, 80, 120$ and $160$ . . . . .	58

LIST OF FIGURES

---

4.6	A TBCs+HCBs ladder consisting of $L = 16$ sites showing the single-particle correlation along each bond (represented by its thickness) and density of particles corresponding to each lattice site (represented by the colorbar on the right) for $J_{\perp}/J = 3$ . . . . .	58
4.7	Single- and two-particle correlations averaged over all the rungs on a system of size $L = 240$ for $J_{\perp}/J = 3$ . . . . .	59
4.8	DMRG data showing the $\rho$ vs $\mu/ U $ plot for $J/ U  = 0.04$ indicating the PSF and SF regions for $L=80$ . The regions marked by the green squares are enlarged in the insets which show the signatures of the SF phase (upper inset) and the PSF phase (lower inset). . . . .	61
4.9	$\Gamma_1(r)$ and $\Gamma_2(r)$ for leg-a are plotted as a function of $r =  i - j $ in log-log scale at $\rho = 0.833$ for $J/ U  = 0.04$ . We consider the lattice sites in the range $L/4$ to $3L/4$ on a system of size $L = 240$ . . . . .	62
4.10	DMRG data shows the $\rho$ vs $\mu/ U $ plot for $J/ U  = 0.04$ indicating the PSF and DRI regions for $L=80$ sites. The regions marked by the green squares are enlarged in the insets indicating the PSF phases. . . . .	63
4.11	DMRG phase diagram of a TBCs+TBCs system showing a gapped-gapless transition from DRI phase to SF phase. The phase boundaries are obtained by extracting the extrapolated values of $\mu^+$ and $\mu^-$ with system sizes $L = 40, 80, 120$ and $160$ . . . . .	64
4.12	Single- and two-particle correlations averaged over all the rungs on a system of size $L = 240$ for $J_{\perp}/J = 3$ . . . . .	65
5.1	(a) Schematic layout of an array of coupled cavity QED system using transmons(not to scale) [3–6]. (b) Equivalent lumped circuit representation of a single transmon coupled to a single transmission line resonator by the coupling capacitors. (c) Shows the energy levels with only one driving frequency $\omega$ . We set $\omega = \varepsilon_{01}$ ( $\hbar=1$ ) and $\alpha = \varepsilon_{12} - \omega$ . . . . .	69
5.2	Phase diagram of the JCH model using the DMRG method in $1d$ for the anharmonicity $\alpha/\beta_{01} = -0.4$ . In this figure the red solid curve demarcates the boundary of the MI(2) phase, the green circles show the PSF-SF phase boundary and the black dashed curve is the vacuum state or the MI(0) phase. For the DMRG method in Fig. 5.2 all boundaries are calculated by extrapolating the chemical potential to thermodynamic limit using maximum system size of $L = 80$ cavities. . . . .	72

- 5.3 (a) DMRG data shows the  $\rho$  vs  $\mu/\beta_{01}$  plot for parameters  $\kappa/\beta_{01} = 0.025$  and  $\kappa/\beta_{01} = 0.05$  when  $\alpha/\beta_{01} = -0.4$  indicating the SF and PSF regions for  $L = 60$  sites. The regions marked by the green boxes are enlarged in Figs. 5.3(c) and (d) which shows the signatures of the PSF and the SF phases respectively. (b)  $\chi_{FS}(\tilde{\kappa})$  vs.  $\kappa/\beta_{01}$  plots for different system sizes of  $L = 20, 40$  and  $60$  to see the phase transition point. (Inset) Shows that the peak heights diverge with system size indicating the phase transition. The dashed vertical line corresponds to the critical point of transition determined by extrapolating the peak position to thermodynamic limit. . . . . 73
- 5.4 Figure shows the pair and single polariton correlation functions  $\Gamma(i, j)$  with distance  $|i - j|$  for  $\rho = 1$  with (a)  $\kappa/\beta_{01} = 0.01$  and (b)  $\kappa/\beta_{01} = 0.06$ . Figs. (c) and (d) shows the two photon and single photon tunneling processes respectively. . . . . 75
- 5.5 Phase diagram of the JCH model using the CMFT method in  $2d$  for the anharmonicity  $\alpha/\beta_{01} = -0.4$ . In this figure the red solid curve demarcates the boundary of the MI(2) phase, the green circles show the PSF-SF phase boundary and the black dashed curve is the vacuum state or the MI(0) phase. In the inset of Fig. 5.5 we show the enlarged PSF region. . . . . 76
- 5.6 (a)  $\rho - \mu/\beta_{01}$  plot at  $\kappa/\beta_{01} = 0.01$  and  $0.02$  of Fig. 5.5. (b) Different correlation functions such as  $\Gamma_{atom-pair}(i, j)$ (Green solid),  $\Gamma_{photon}(i, j)$ (blue dot-dashed),  $\Gamma_{photon-pair}(i, j)$ (black dots) and  $\Gamma_{atom}(i, j)$ (red dashed) are plotted for  $\kappa/\beta_{01} = 0.01$  (see text). . . . . 77
- 5.7 The polariton energies  $E_n$ (bottom to top for  $n = 1 \rightarrow 5$  at the origin) for  $\mu/\beta_{01} = -1$  with respect to  $\beta_{12}/\beta_{01}$  for  $\alpha/\beta_{01} = -0.4$ . . . . . 78
- 5.8 (a) DMRG data shows the  $\rho$  vs.  $\mu/\beta_{01}$  plot (black solid) for parameters  $\kappa/\beta_{01} = 0.01$  when  $\alpha/\beta_{01} = -0.4$  indicating the PSF and SF regions for  $L = 60$  sites in 1d. The regions marked by the green boxes are enlarged in Figs. 5.8 (b) and (c) which shows the signatures of the PSF and the SF phases respectively. (d) CMFT data for the  $\rho$  vs  $\mu/\beta_{01}$  plot (red solid) for  $\kappa/\beta_{01} = 0.01$  and  $\alpha/\beta_{01} = -0.4$  indicating the PSF phase for 4 sites in 2d. . . . . 79



# Chapter 1

## Introduction

### 1.1 Quantum phase transitions

Phase transition is a very important phenomenon of nature which is marked by an abrupt change of any thermodynamic system from one phase of matter to another phase belonging to the same substance. A typical example is ice turning into water with an increase in temperature. This is an example of classical or thermal phase transition, where the transition is driven by temperature. In thermal phase transition, the order of the phase transition is defined in terms of the discontinuity in the order of derivative of Helmholtz free energy with respect to thermodynamic variables. For example, if the first order derivative of Helmholtz free energy is discontinuous, then it is called the first-order transition (e.g. liquid-gas transition at constant pressure), and if the second-order derivatives are discontinuous, it is called second-order phase transition or continuous phase transition (e.g., liquid-vapour transition at constant pressure at the critical point). On the other hand, another form of phase transition is the quantum phase transition (QPT), that takes place at absolute zero temperature. The QPTs are governed by the Heisenberg uncertainty principle and are driven by quantum fluctuations which are triggered by some non-thermal parameters such as the magnetic field, pressure, etc. The QPTs occur in different systems and are observed in various tabletop experiments involving condensed matter and atomic, molecular, and optical physics (AMO) systems.

The study of complex many-body systems using QPTs has become a topic of immense interest in recent years due to the presence of the various rich quantum phases, which in general arises under the influence of periodic potentials. These QPTs appear in the condensed matter systems due to the competition between interparticle interactions and strong correlations. In our conventional solid-state

system, there are several difficulties due to the existence of defects and disorders in the lattice. On top of that, the solid-state systems lack the flexibility in tuning the geometries of the lattice and interparticle interactions, which are essential for observing a broad range of QPTs. To circumvent this problem, various unique quantum simulators have been theoretically suggested and experimentally perceived in recent years to imitate the QPTs in condensed matter systems.

The ultracold atoms in optical lattices are an emerging quantum simulator which can overcome the shortcomings of conventional condensed matter systems.

The first experimental observation of quantum phase transition in systems of ultracold atoms in a three-dimensional (3D) optical lattice was made by the group of I. Bloch [7] and later by the group of T. Esslinger [8] in a one dimensional (1D) optical lattice system. These seminal discoveries have paved the path for a new field of research where the artificial system can be used to study the physics of complex many-body systems [7, 9–11]. The unparalleled control over the system parameters using the sophisticated experimental techniques in such simulators has revealed a wealth of novel physics in recent years.

## 1.2 QPT in optical lattices

### 1.3 Optical lattice

An optical lattice is a set of spatially periodic potentials formed by the interference of coherent counter-propagating laser beams; thus, the resulting periodic potential may trap ultracold atoms. Once the ultracold atoms get localized, they can interact with the external laser field due to their internal degrees of freedom. For scheming an optical lattice potential in those systems, the decisive point is to manipulate the light-matter interaction. Due to the light-matter interaction, the electric dipole moment induced in the atom is proportional to the applied electric field of the laser,  $d_E = \eta(\omega)E$  where the constant of proportionality  $\eta(\omega)$  is called the polarizability. When the frequency of laser  $\omega$  lies in the neighborhood of transition frequency ( $\omega_0$ ), between the ground state ( $|0\rangle$ ) and the excited state ( $|1\rangle$ ), the polarizability gets modified as:

$$\eta(\omega) \approx \frac{|\langle 1|d_E|0\rangle|^2}{\hbar(\omega_0 - \omega)} \quad (1.1)$$

$\eta(\omega)$  is in general a complex quantity with its real part gives rise to the dipole potential, which is the time average of the dipole moment

$$V_{dip}(r) = -\frac{1}{2\epsilon_0 c} \text{Re}(\eta)I \quad (1.2)$$

and its imaginary part come up with the spontaneous scattering given as

$$\Gamma_{sc} = -\frac{1}{\hbar\epsilon_0 c} \text{Im}(\eta)I \quad (1.3)$$

where  $I$  is the intensity of the laser beam  $I = \frac{1}{2}\epsilon_0 c |E|^2$ . The dipolar force which is responsible for atomic trapping and cooling comes from the dipole potential and is written as

$$\mathbf{F} = \frac{1}{2}\eta(\omega) \nabla (|\mathbf{E}(r)|^2) \quad (1.4)$$

Now, from Eqs. 1.4 and 1.1, it is obvious that the sign of  $\eta(\omega)$  plays a decisive role for determining the direction of the dipolar force  $\mathbf{F}$ . Therefore the positive sign of  $\mathbf{F}$  for red detuned laser ( $\omega > \omega_0$ ) specify the attraction of atoms towards the intensity maxima while the negative sign of  $\mathbf{F}$  for blue detuned laser ( $\omega < \omega_0$ ) repels atom out of intensity maximum.

Now for a two-level system, using the rotating wave approximation, the dipole potential and the scattering rate gets modified in terms of the damping rate,  $\Gamma$  [12] as

$$V_{dip}(r) \approx \frac{3\pi c^2}{2\omega_0^3} \frac{\Gamma}{\Delta} I(r) \quad \Gamma_{sc}(r) \approx \frac{3\pi c^2}{2\hbar\omega_0^3} \frac{\Gamma^2}{\Delta} I(r) \quad (1.5)$$

where  $\Delta = \omega - \omega_0$  is the detuning associated to the atomic transition. Therefore a simple relation can be established between the dipole potential and the scattering rate.

$$\frac{V_{dip}}{\Gamma_{sc}} = \frac{\hbar\Delta}{\Gamma} \quad (1.6)$$

Now the intensity or the spatial intensity of a Gaussian laser beam propagating along the  $z$ -axis is a function of  $r$  and  $z$  where  $r$  is the radial distance from the axis of the beam and  $I_0$  is the beam intensity at  $r = 0, z = 0$ . Therefore, for a one-dimensional optical lattice, formed by the interference of two counter-propagating laser beams having wavelength twice of the lattice constant, the potential profile close to the trap center for a sufficiently strong optical lattice is given by [12]

$$V_{lat}(x) = -V_{lat,0} \cos^2(kx) \quad (1.7)$$

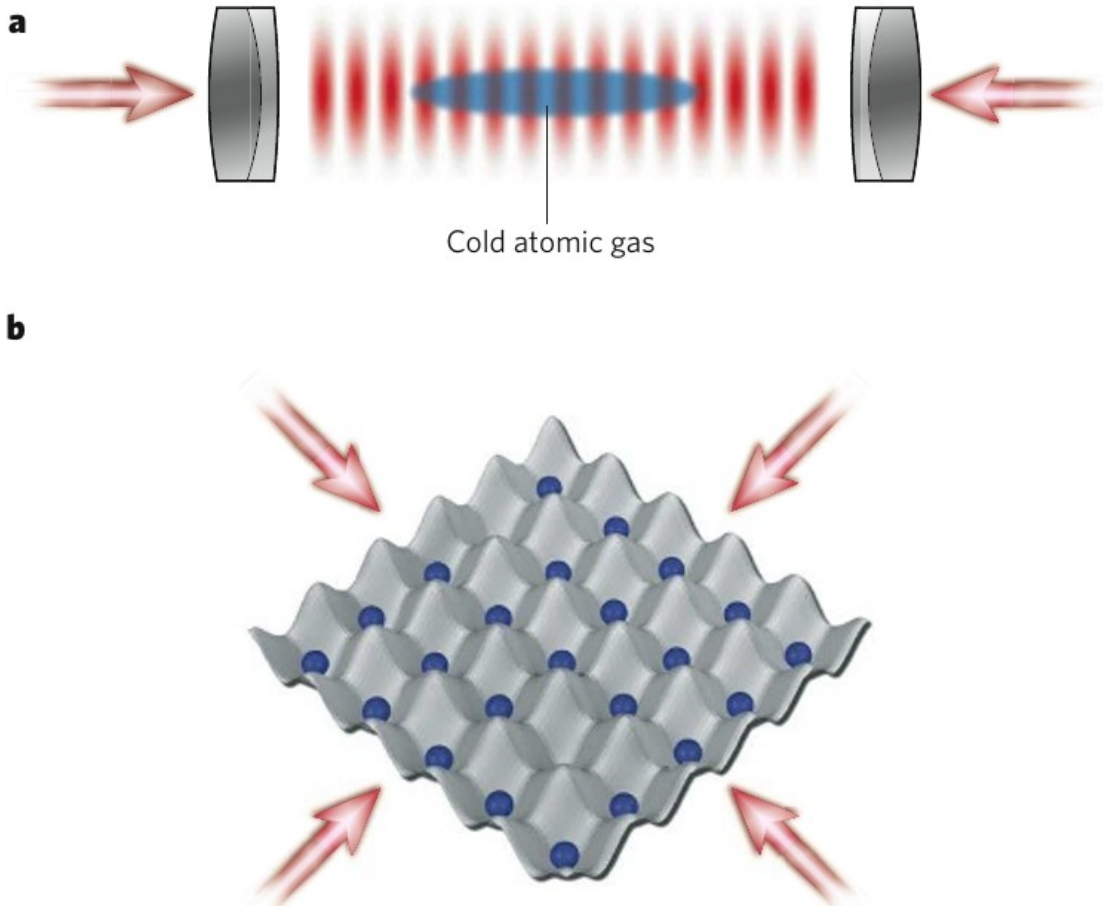


**Figure 1.1:** (a) Formation of an optical lattice by superimposing two laser beams. The nodes or antinodes of the optical lattice behaves as a periodic array for trapping the atoms. (b) Formation of a two dimensional lattice potential by the superimposition of three orthogonal standing waves. The figure is obtained from Ref. [1].

where  $V_{lat,0} \sim 4I_0$ .

Generally with the help of two or more pairs of counter propagating laser beams one can construct optical lattice in two and three-dimensions (Fig. 1.1). The equation of a three-dimensional optical lattice potential, in general, can be described as,

$$V_{lat}(x, y, z) = -V_{lat,0}[\cos^2(k_x x) + \cos^2(k_y y) + \cos^2(k_z z)]. \quad (1.8)$$

It is to be noted that the one- and two-dimensional optical lattices can be mimicked from a three-dimensional one by constructing deep lattices in one and two directions, respectively.

Apart from the cubic and square lattices, we can engineer several fascinating lattice geometries like kagome [13] and triangular structures, by applying a suitable

number of laser beams oriented in proper directions. Also the procedure of holographic projections in the framework of the single-site microscopy [14] can be applied for the generation of optical lattices. The SF to MI phase transition of bosonic particles, both in theory and experiments [2] have been successfully speculated by the optical lattice [15, 16].

### 1.3.1 Ultracold bosons in optical lattice: The Bose-Hubbard model

As mentioned already, the systems of ultracold atoms in optical lattices are one of the most successful platforms to simulate various physical problems. The ease to control of the geometry and strong correlation in the system has resulted in many novel findings. In recent years, it has also been possible to manipulate different types of particles such as bosons, fermions, and mixtures of different types of atoms and molecules in optical lattices. These Experimental progress and theoretical studies have broadened our physical understanding in the context of ultracold atoms in an optical lattice.

The simplest system which was first explored in this context is the ultracold bosons in optical lattices. The physics of such systems can be explained by the famous Bose-Hubbard(BH) model, which was first proposed by Gersch and Knollman [17] in 1962. This is considered as the bosonic version of the Fermi Hubbard model that has been successful in explaining the behavior of strongly correlated fermions like high-temperature superconductors. Initially, the BH model was applied for explaining the phase transition of superfluid Helium absorbed in disorder systems like Vycor [15] which was a complex system to formulate experimentally. However, the seminal work of Greiner et al. experimentally demonstrated the superfluid to Mott insulator transition of bosons by simulating the BH model using the ultracold atoms in optical lattice setup.

In the following we briefly discuss the BH model and the SF-MI phase transition. In second quantized notation, the Hamiltonian for interacting bosons can be written as

$$\begin{aligned} \mathcal{H} = & \int \Phi^\dagger(\vec{x}) \left[ -\frac{\hbar^2}{2m} \nabla^2 + V(\vec{x}) \right] \Phi(\vec{x}) d^3x \\ & + \frac{1}{2} \int \int d^3x d^3y \Phi^\dagger(\vec{x}) \Phi^\dagger(\vec{y}) U(|\vec{x} - \vec{y}|) \Phi(\vec{y}) \Phi(\vec{x}) \end{aligned} \quad (1.9)$$

where  $V(x)$  is the trapping potential, which is a combination of the external confining

potential for trapping of atoms and the lattice potential.  $U(|\vec{x} - \vec{y}|)$  is the interaction between two bosons.  $m$  represents the atomic mass and  $\Phi$ 's are the field operators of bosons that satisfy the standard bosonic commutation relations of bosons

$$[\Phi(\vec{x}), \Phi^\dagger(\vec{x}')] = \delta^3(\vec{x} - \vec{x}'), \quad [\Phi(\vec{x}), \Phi(\vec{x}')] = [\Phi^\dagger(\vec{x}), \Phi^\dagger(\vec{x}')] = 0 \quad (1.10)$$

The interaction  $U(|\vec{x} - \vec{y}|)$  between two bosons is governed by the  $s$ -wave scattering process [18]. In this limit one can safely assume  $U(|\vec{x} - \vec{y}|)$  as an effective contact potential written in terms of the  $s$ -wave scattering length  $a_0$  and is given as

$$U(|\vec{x} - \vec{y}|) = U_0 \delta^3(\vec{x} - \vec{y}), \quad U_0 = \frac{4\pi\hbar^2 a_0}{m} \quad (1.11)$$

For a system having periodic potential, the localized Wannier functions are more suitable to use instead of the Bloch wavefunctions that are delocalized in the lattices. By applying the Fourier transform over the Bloch states, one can find the Wannier functions of the following form:

$$W_{ni}(\vec{x}) = \frac{1}{\sqrt{M}} \sum_{k=1}^M e^{i\vec{k} \cdot (\vec{x} - \vec{R}_i)} u_{nk}(\vec{x}) \quad (1.12)$$

Here, the  $\{W_{ni}(\vec{x})\}$  forms a complete set of orthonormal basis, named as Wannier basis, that satisfies the condition of orthonormality

$$(W_{mj}(\vec{x}), W_{ni}(\vec{x})) = \int_V d^3x W_{mj}^*(\vec{x}) W_{ni}(\vec{x}) = \delta_{mn} \delta_{ji} \quad (1.13)$$

The bosonic field operators can then be expanded in terms of the Wannier basis as follows:

$$\Phi(\vec{x}) = \sum_{n,i} W_{ni}(\vec{x}) a_{ni} \quad \Phi^\dagger(\vec{x}) = \sum_{n,j} W_{nj}(\vec{x}) a_{nj}^\dagger \quad (1.14)$$

Here, the operators  $a_i^\dagger$  and  $a_i$  are respectively known as the bosonic creation and annihilation operators at site  $i$  and they follow the standard commutation relations of bosonic particles as:

$$[a_{ni}, a_{nj}^\dagger] = \delta_{ij} \quad [a_{ni}, a_{nj}] = 0 = [a_{ni}^\dagger, a_{nj}^\dagger] \quad (1.15)$$

Ensuring the lattice to be deep enough and the Wannier functions to be well localized, the Hamiltonian shown in Eq. 1.9 can be written in the tight-binding

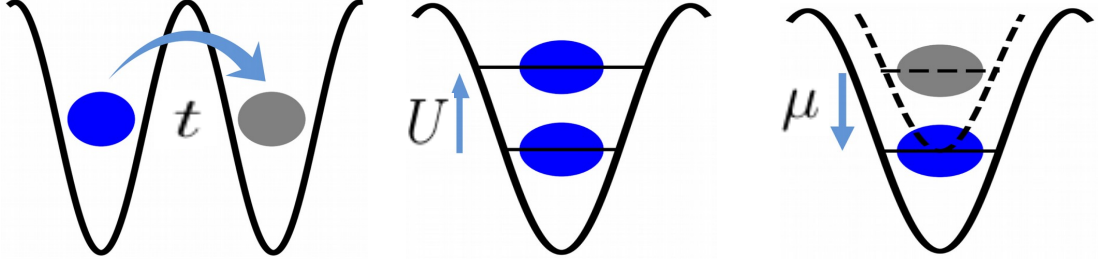


**Figure 1.2:** Figure depicts the significance of different parameters in the BH model given in Eq. 1.16.

approximation as;

$$H = - \sum_{\langle i,j \rangle} t_{i,j} (a_i^\dagger a_j + H.c.) + \frac{U}{2} \sum_i n_i (n_i - 1) - \sum_i \mu_i n_i \quad (1.16)$$

The Hamiltonian shown in Eq. 1.16 is known as the BH model and is widely used to study the physics of ultracold bosons in optical lattices. The parameters appearing in this BH model such as  $t_{i,j}$  is the hopping amplitude between the sites  $i$  and  $j$ ,  $U$  is the onsite two particle interaction energy and  $\mu$  is the chemical potential of the system that controls the particle number. The significance of these parameters are depicted in Fig. 1.2.

Using the Wannier functions, the individual parameters appearing in Eq. 1.16 can be written as:

$$t_{i,j} = - \int d^3x W^*(x - x_i) \left[ \frac{\hbar^2}{2m} \nabla^2 + V(x) \right] W(x - x_j) \quad U = a_0 \frac{4\pi\hbar^2}{m} \int d^3x |W(x)|^4 \quad (1.17)$$

Since the Wannier functions are well localized in the lowest band, we can drop the band index from it. Using a deep lattice with lattice of depth  $V_0$  and with the help of one dimensional Mathieu equation [19], the hopping amplitude and two-particle interaction can be rewritten as:

$$t \approx \frac{4}{\sqrt{\pi}} \left( \frac{V_0}{E_R} \right)^{3/4} e^{-2\sqrt{\frac{V_0}{E_R}}} E_R \quad U_{har} = \sqrt{\frac{8}{\pi}} \left( \frac{V_0}{E_R} \right)^{3/4} E_R \quad (1.18)$$

where  $E_R$  is the recoil energy of the atom.

As mentioned earlier, by tuning the lattice depth, it is possible to adjust the ratio between the two-body interaction  $U$  and the hopping strength  $t$  in optical lattices.

On the other hand, one can independently tune the two-particle interaction by applying the techniques of Feshbach resonances, introduced initially in the context of nuclear reactions [20]. These control parameters are the key to study the effect of strong correlation and associated phase transitions in the BH model. In the following, we will discuss the well-known SF-MI phase transition in this context.

### 1.3.2 Superfluid to Mott-insulator transition

The many-body physics of the BH model relies on the relative strengths of the parameters such as the  $U$  and  $t$ . Depending on the this two different scenarios arise such as

1. Weak Lattice ( $U/t \approx 0$ ) limit, when the atoms are highly mobile.
2. Strong Lattice ( $t/U \approx 0$ ) limit when the atoms are localized.

For a given system with a fixed number of particles per site, a quantum phase transition from delocalized to localized phase takes place as the ratio  $t/U$  is varied. The delocalized phase is termed as the superfluid phase whereas the localized phase is termed as the Mott insulator (MI) phase. The MI phase is characterized by the existence of a non-vanishing energy gap i.e., a finite amount of energy is required for adding a particle or hole excitation. This phase is said to be incompressible i.e.,  $\partial n/\partial\mu = 0$ , here  $n = N/L$  is the number of particles per site, also known as the particle density.

On the other hand, the SF phase is determined by the large density fluctuation per site, which is associated with the reduction in phase fluctuation, forming a coherent state. In the SF phase, the energy gap vanishes, and the compressibility remains finite. This phenomenon was first predicted by Fisher *et al.*[15] for a system of bosons in periodic potentials. It was shown that the SF-MI phase transition could occur in two different ways.

1. For fixed integer densities and by varying the ratio of  $t/U$ .
2. For a fixed value of  $t/U$  and by varying the density of the system.

For large hopping strengths  $t/U \gg 1$ , the wavefunction of individual particles overlap due to the presence of excessive kinetic energy in the system, resulting in an unrestricted motion of atoms throughout the entire lattice. In that case, the ground

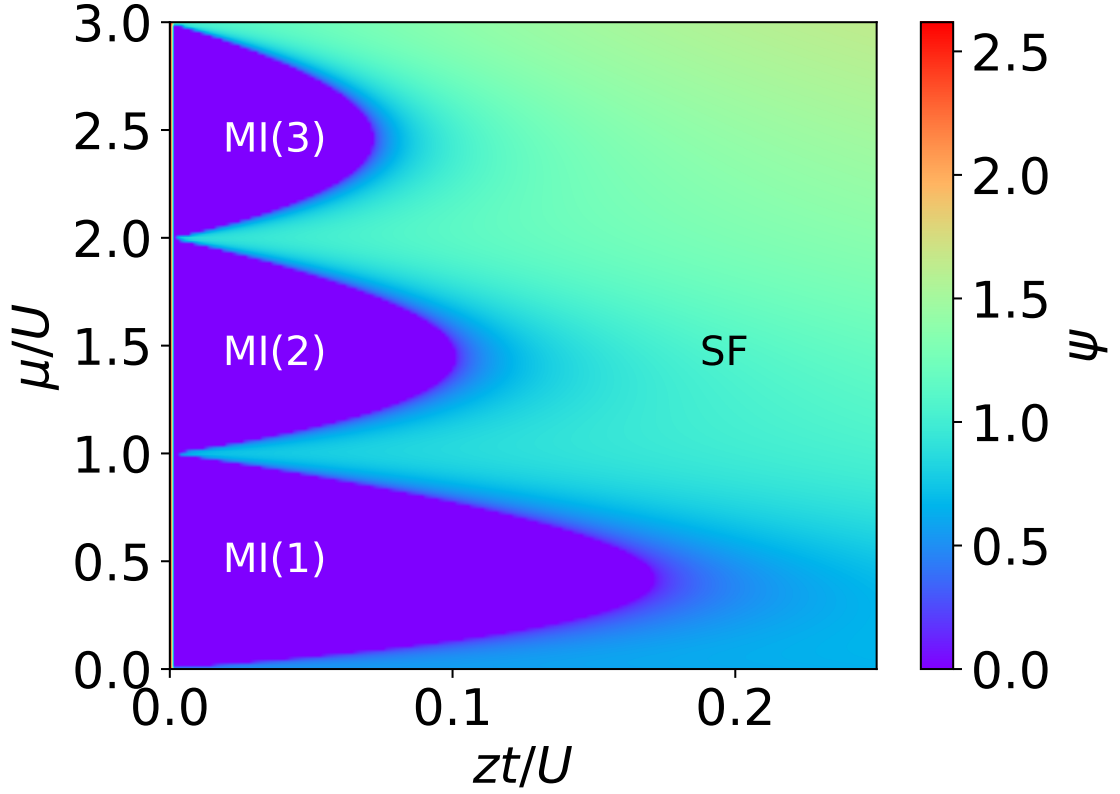


**Figure 1.3:** The mean-field phase diagram of the BH model (1.16) in  $\mu/U - zt/U$  plane. Here MI( $n$ ) is the MI with density  $n$ .

state of a system of  $N$  number of bosons and size  $L$  can be written as

$$|\Phi_{SF}\rangle_{U/t=0} \propto \left( \sum_i^L a_i^\dagger \right)^N |0\rangle \quad (1.19)$$

where  $|0\rangle$  corresponds to the vacuum state. Eq. (1.19) represents the wavefunction of the system in the SF phase, which is characterized by the off-diagonal long-range order (ODLRO). In the other limit, when  $t/U \ll 1$ , the two body onsite energy dominates over the kinetic energy resulting in a state of vanishing onsite number fluctuation. As a consequence, the system localizes into a many-body ground state for which the wave function can be written as the product state which is given by

$$|\Phi_{MI n}\rangle_{t/U=0} \propto \prod_i^L (a_i^\dagger)^n |0\rangle \quad (1.20)$$

Here MI( $n$ ) represents the MI phase with fixed boson density  $n = N/L$ . The system

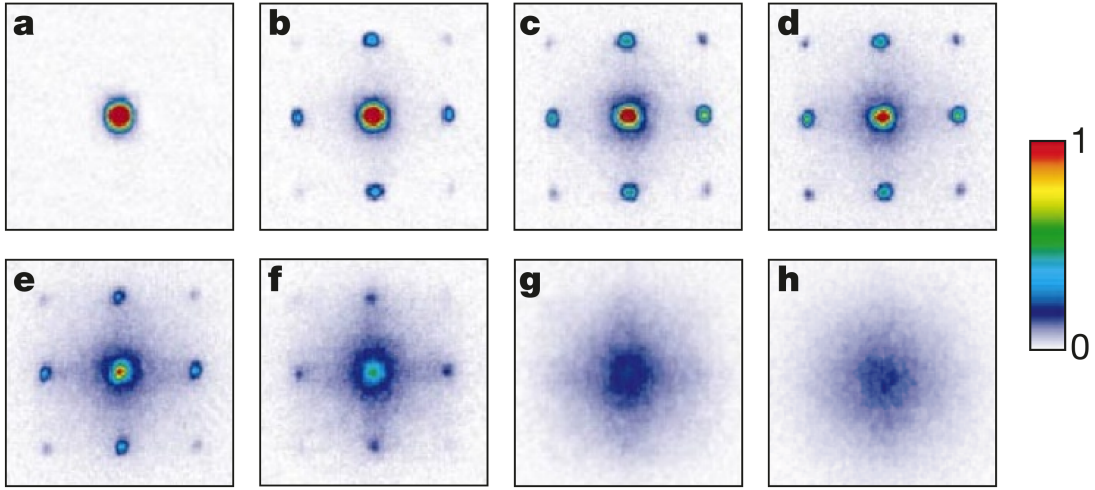


**Figure 1.4:** Experimental result of the first observation of SF-MI transition (taken from [2]). The figure shows the absorption images of matter-wave interference pattern for different initial states prepared for different lattice depth ( $V_0$ ). Here  $V_0$  are, in (a)  $0E_r$ , (b)  $3E_r$ , (c)  $7E_r$ , (d)  $10E_r$ , (e)  $13E_r$ , (f)  $14E_r$ , (g)  $16E_r$  and (h)  $20E_r$ .

undergoes a phase transition from SF to MI state when the ratio ( $t/U$ ) approaches a critical value  $(t/U)_c$ . The phase diagram of QPT is depicted in Fig. 1.3 for a  $d$ -dimensional lattice system [15] obtained using the site decoupled mean-field theory (SDMFT). Fig. 1.3 shows several MI( $n$ ) lobes with fixed integer density  $n$  in the  $\mu/U - zt/U$  plane in the strong interaction limit (or weak hopping) with  $z$  being the coordination number. However, in the weak interaction limit (or strong hopping), the system exhibits the SF phase (white area). The SF-MI transition takes place at a critical value of the ratio  $t/U$ , which according to SDMFT is  $U = 5.8zt$  for  $n = 1$  where  $U$  is the onsite interaction energy,  $t$  is the hopping strength and  $z$  is the coordination number (Fig. 1.3) [15, 21, 22].

Since this QPT is unattainable in a conventional solid-state system, Jaksch *et al.* [16] in 1998 had made a new proposal to simulate this fascinating phenomenon using ultracold bosonic atoms trapped in optical lattices. Later on, this was experimentally verified by Greiner *et al.* [2] in 2002 using a cubic optical lattice in three-dimension where BEC is formed with the help of  $^{87}\text{Rb}$  atoms. The SF-MI transition is observed by studying the absorption images achieved by expanding the atoms ballistically from a lattice with several potential depths  $V_0$ , shown in Fig. 1.4. The interference pattern exhibits a sharp peak for small values of  $V_0 \leq 13E_r$ , indicating the presence of coherence nature in the system leading to the formation of the SF phase. On the other hand, as  $V_0$  becomes larger than  $13E_r$ , the interference

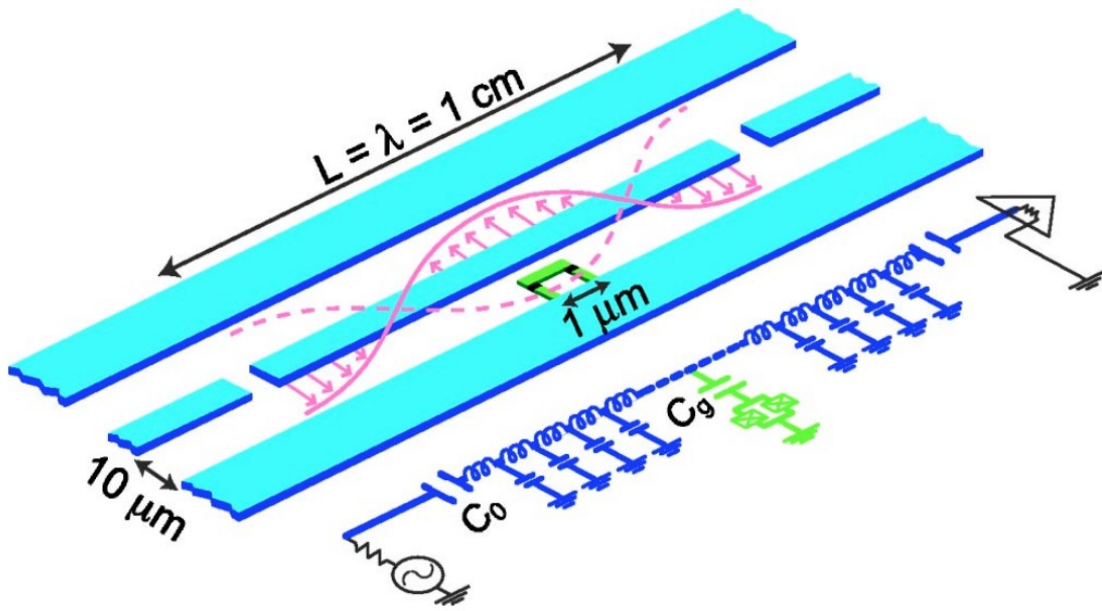


**Figure 1.5:** Schematic layout of superconducting circuits and its equivalent lumped circuit representation for implementing cavity QED using them [3].

pattern becomes faded, resulting in an MI phase which is incoherent in nature.

## 1.4 QPT in superconducting circuits

The study of QPTs using optical lattices involves some challenging problems such as cooling and trapping atoms down to a temperature of the order of nano-Kelvin and complications to access and control single sites individually. Also, during experiments using ultracold atoms, one has to turn off the trap in order to observe the actual quantum phase of the system. As a consequence, the system under observation is completely destroyed. Although, recent experimental progress has allowed for fluorescence imaging [23] and single-site addressing techniques [24], these methods have their own complexities.

These shortcomings of optical lattices for studying QPT can be overcome by using other experimental methods such as the experimental schemes of cavity quantum electrodynamics (QED). In cavity QED, a lattice is developed by fabricating and manipulating microcavities [25–27] or by some other experimental methods like using trapped atoms, manipulating Rydberg states [28], using two- or three-dimensional photonic band-gap cavities [29–32] and light is coupled to the atoms of the lattice.

The intrinsic nonlinearity present in the atoms (also known as Kerr nonlinearity) gives rise to the so-called photon blockade effect [33–37] which in turn produces an attractive or repulsive type of interaction. The presence of such Kerr type nonlinearity induced interactions has made it possible for the experimental observation of BECs [38–40], superfluids [41, 42] etc. in semiconductor cavities.

Although the cavity QED systems have several advantages over the optical lattice systems for studying QPT, these systems have two major shortcomings. One is the intrinsic dipole moment of natural atoms, which is usually very small, and the atom-photon coupling strength, which is fixed for a given system. These problems can be resolved by using artificial atoms formed by the Josephson Junction (JJ) [43] which takes the place of natural atoms. Once we couple the artificial atom with a quantum-mechanical LC oscillator operating in the microwave regime, we can achieve similar physics as that of the cavity-QED system. The study of such couplings, which occurs in the presence of the superconducting circuits, is known as the circuit QED [3, 44]. The circuit QED systems are much preferred over the cavity QED system due to their flexibility in fabrication and their usefulness in the non-equilibrium situation. Using the superconducting circuits, we can achieve relatively high coherence times roughly a few microseconds [45]. We will elaborate on the circuit QED section below.

### 1.4.1 Qubits

A quantum mechanical LC oscillator can be formed with one inductor and one capacitor. However, the quantum energy levels of the harmonic oscillator are equally spaced, which makes the selective transition between two levels an impossible task. In order to address a specific pair of levels, we need to introduce some anharmonicity in the system like the JJ [43] which is a nonlinear dissipationless circuit element. The JJ can be used for the construction of qubits, which is the acronym for quantum bits, is a device where we can achieve a selective transition between two levels. The sufficient anharmonicity present in the qubit system makes it an effective two-level system for circuit QED operations despite the fact that the qubit possesses all possible energy levels. Depending on the quantized variable, one can construct different types of qubits: namely the flux qubits [46, 47], phase qubits [48] and charge qubits [49–51]. The qubits are also called artificial atoms from circuit QED's viewpoint since they play a similar role to real atoms in cavity QED.

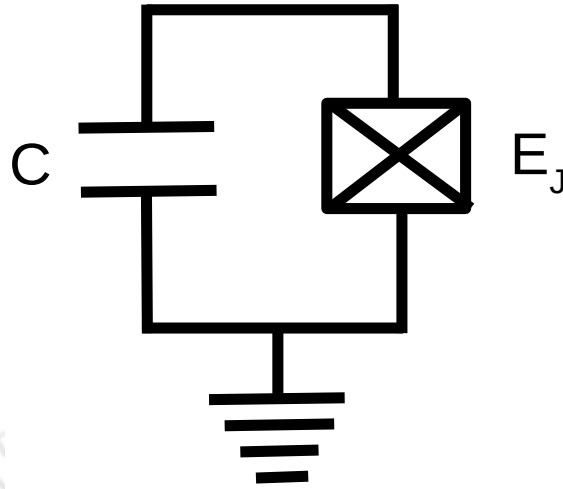


**Figure 1.6:** The charge qubit formed by the Josephson Junction (JJ) with charging energy  $E_J$  and a capacitor  $C$ .

### 1.4.2 Charge Qubit

A charge qubit is a special type of qubit formed when we replace the linear inductor by a JJ in a quantum mechanical LC circuit shown in Fig. 1.6. It mainly operates in two regimes depending on the amount of anharmonicity present in the circuit. These regimes are

1. One is the Cooper Pair Box (CPB) regime [50, 52] where anharmonicity is very large.
2. Another is the transmon [4] regime, where one can approximate the anharmonicity as a small perturbation to the harmonic oscillator Hamiltonian.

In the later part of the thesis, we will mostly focus on the transmon regime of charge qubit.

The Hamiltonian corresponding to a charge qubit is given by:

$$H = \frac{q^2}{2C} - E_J \cos \varphi \quad (1.21)$$

where  $C$  is the total capacitance,  $q$  is the total charge in the circuit,  $\varphi$  is the gauge invariant dimensionless phase  $\varphi = \phi/\phi_0$  with  $\phi_0$  is the superconducting flux quanta i.e.,  $\phi_0 = h/2e$ . Now for charge qubits it is more convenient to work with the number operator  $n$  rather than the charge operator  $q$  i.e.  $n = -q/2e$ , which counts the number of cooper pairs crossing the junction. We define  $E_C = q^2/2C$  as the

charging energy. Therefore Eq. 1.21 gets modified as:

$$H = 4E_C n^2 - E_J \cos \varphi \quad (1.22)$$

Now the presence of the gate electrode coupled to the qubits via coupling capacitors and operating at a fixed voltage introduces some offset in the circuit. This offset reduces the total charge of the system and Eq. 1.22 gets modified as:

$$H = 4E_C (n - n_g)^2 - E_J \cos \varphi \quad (1.23)$$

Here  $n_g = Q_r/2e + C_g V_g/2e$  is the effective offset charge after subtracting the offset charge due to the gate electrode plus the offset charge due to the environmental sources represented as  $Q_r$ . The operators  $\varphi$  and  $n$  are canonically conjugate, defined by the following relation:

$$[\varphi, n] = -i \quad (1.24)$$

The analytical solution of the Hamiltonian in Eq. 1.23 is given as:

$$E_p(n_g) = E_C a_{2[n_g + k_{(p, n_g)}]} \left( -\frac{E_J}{2E_C} \right) \quad (1.25)$$

where  $a_\nu(q)$  represents Mathieu characteristic value and  $k_{(m, n_g)}$  is a integer valued function which orders the  $n$  discrete eigenvalues [4]. Since the evaluation of  $a_\nu(q)$  turns out to be a tedious task, we rewrite the Hamiltonian in a more convenient way, in terms of the reduced charge basis  $|n\rangle$  as follows:

$$H = 4E_C \sum_{k=-N}^N (k - n_g)^2 |k\rangle \langle k| - E_J \sum_{k=-N}^{N-1} (|k+1\rangle \langle k| + |k\rangle \langle k+1|) \quad (1.26)$$

### 1.4.3 Circuit QED for transmons

In Fig. 1.7 we have shown a transmon placed at the centre of a coplanar waveguide type Transmission Line Resonator (TLR). The circuit shown in the figure satisfies the open boundary condition and the net Hamiltonian of the system can be written as the sum of Hamiltonian of the transmon plus the Hamiltonian of the TLR and the Hamiltonian containing the dipole coupling term between the transmon and the resonator:

$$H = 4E_C (n - n_g)^2 - E_J \cos \varphi + \omega_r b^\dagger b + 2\beta e V_{rms}^0 n (b^\dagger + b) \quad (1.27)$$

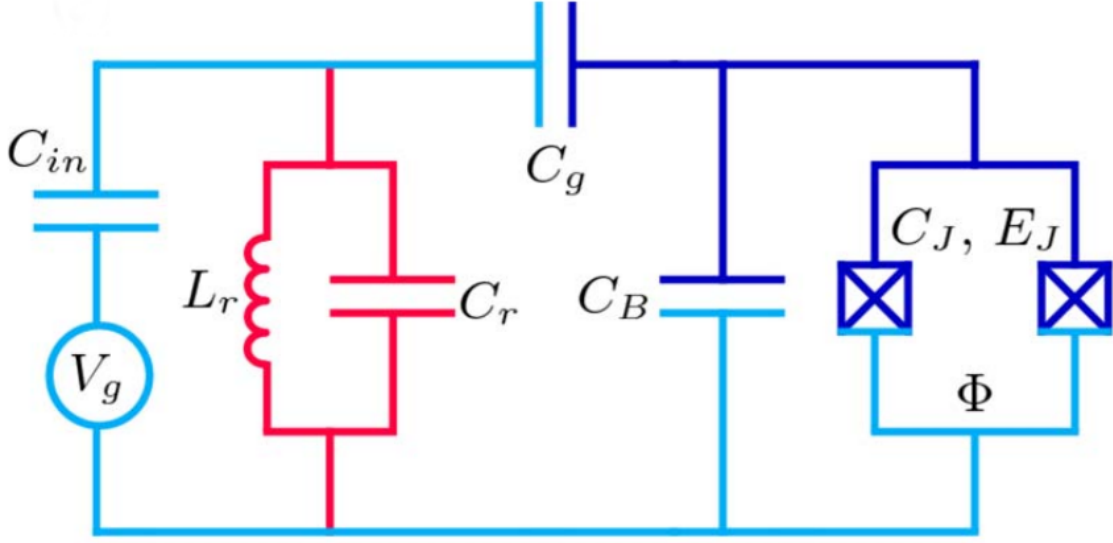


**Figure 1.7:** Circuit diagram of a transmon qubit consisting of two JJs with capacitances  $C_J$  and Josephson energy  $E_J$ , a biasing capacitor  $C_B$  and a gate capacitor  $C_g$  connected to a resonator with capacitance  $C_r$  and inductance  $L_r$ . A voltage  $V_g$  is applied to the circuit through the coupling capacitor  $C_{in}$  [4]

where,  $\omega_r = 1/\sqrt{L_r C_r}$  is the frequency of the resonator,  $V_{rms}^0 = \sqrt{\omega_r/2C_r}$  is the root mean square voltage,  $\beta = C_g/C_\Sigma$  is ratio of two capacitances,  $C_g$  and  $C_\Sigma = C_J + C_B + C_g$ ,  $2e$  is the charge of a Cooper pair,  $b^\dagger(b)$  is the creation (annihilation) operator corresponding to the photonic excitations. We define the atom-photon coupling term as

$$g_{jk} = 2\beta e V_{rms}^0 \langle j|n|k \rangle \quad (1.28)$$

Now rewriting the above mentioned Hamiltonian of Eq. 1.27 in terms of the eigenkets forming the basis of transmon and using the expression for atom-photon coupling term given in Eq. 1.28, we obtain the generalized Jaynes-Cummings (JC) Hamiltonian:

$$H = \sum_k \omega_k |k\rangle \langle k| + \omega_r b^\dagger b + \sum_k (g_{j,k} |j\rangle \langle k| (b + b^\dagger)) \quad (1.29)$$

Now we simplify the above Hamiltonian in Eq. 1.29 by applying the rotating wave approximation [4] ( $|g_k| \ll \omega_k, \omega_r$ ) and the selection rule of electric dipole transition:

$$H = \sum_k \omega_k |k\rangle \langle k| + \omega_r b^\dagger b + \sum_k (g_{k,k+1} |k\rangle \langle k+1| b^\dagger + H.C.) \quad (1.30)$$

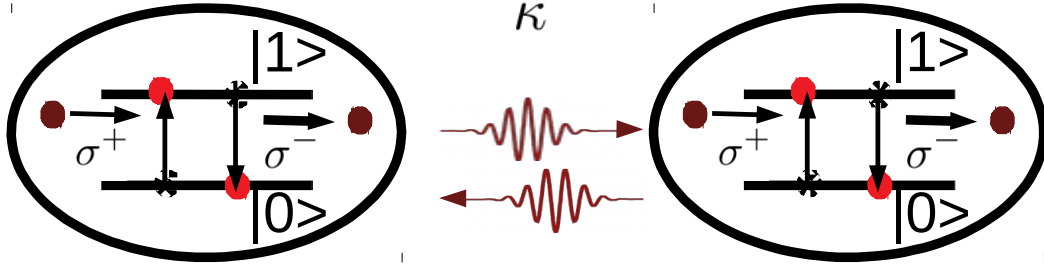


**Figure 1.8:** JCH model for two cavities representing the atomic transition operators  $\sigma^+$ ,  $\sigma^-$  and photon hopping strength  $\kappa$ .

Now we consider a series of coupled-cavity-array with each cavity containing a two-level system (transmon). These cavities are coupled capacitively to one another and also to the TLR. The Hamiltonian for such a system can be written with the help of Eq. 1.30 by adding the nearest-neighbor photon hopping term and the chemical potential term,

$$\begin{aligned}
 H = & \omega \sum_i \sigma_i^+ \sigma_i^- + \omega_r \sum_i b_i^\dagger b_i + \beta \sum_i (\sigma_i^- b_i^\dagger + \sigma_i^+ b_i) \\
 & - \kappa \sum_{i,j} (b_i^\dagger b_j + H.C.) - \mu \sum_i n_i
 \end{aligned} \quad (1.31)$$

where  $\beta = g_{01}$ ,  $\omega = \omega_1 - \omega_0$  and  $\sigma_i^+$  and  $\sigma_i^-$  is the atomic transition operator for a two level system or qubit at the  $i^{\text{th}}$  cavity,  $|0\rangle_i$  and  $|1\rangle_i$ , as shown in Fig. 1.8 is given as

$$\begin{aligned}
 \sigma_i^+ &= |1\rangle_i \langle 0|_i \\
 \sigma_i^- &= |0\rangle_i \langle 1|_i \\
 \sigma_i^+ \sigma_i^- &= |1\rangle_i \langle 1|_i
 \end{aligned} \quad (1.32)$$

The Hamiltonian mentioned in Eq. 1.31 is known as the Jaynes-Cummings-Hubbard (JCH) Hamiltonian. We can modify Eq. 1.31 as follows

$$\tilde{H} = -\tilde{\mu} \sum_i n_i - \tilde{\Delta} \sum_i \sigma_i^+ \sigma_i^- + \sum_i (\sigma_i^- b_i^\dagger + \sigma_i^+ b_i) - \tilde{\kappa} \sum_{i,j} (b_i^\dagger b_j + H.C.) \quad (1.33)$$

where  $\tilde{\mu} = (\mu - \omega)/\beta$ ,  $\tilde{\Delta} = \Delta/\beta$  and  $\tilde{\kappa} = \kappa/\beta$ . Here we define a quantity which is the sum of number of atoms and number of photons in a single cavity, also known as the polariton number  $n_i$  of the  $i^{\text{th}}$  cavity, written as  $n_i = \sigma_i^+ \sigma_i^- + b_i^\dagger b_i$ .

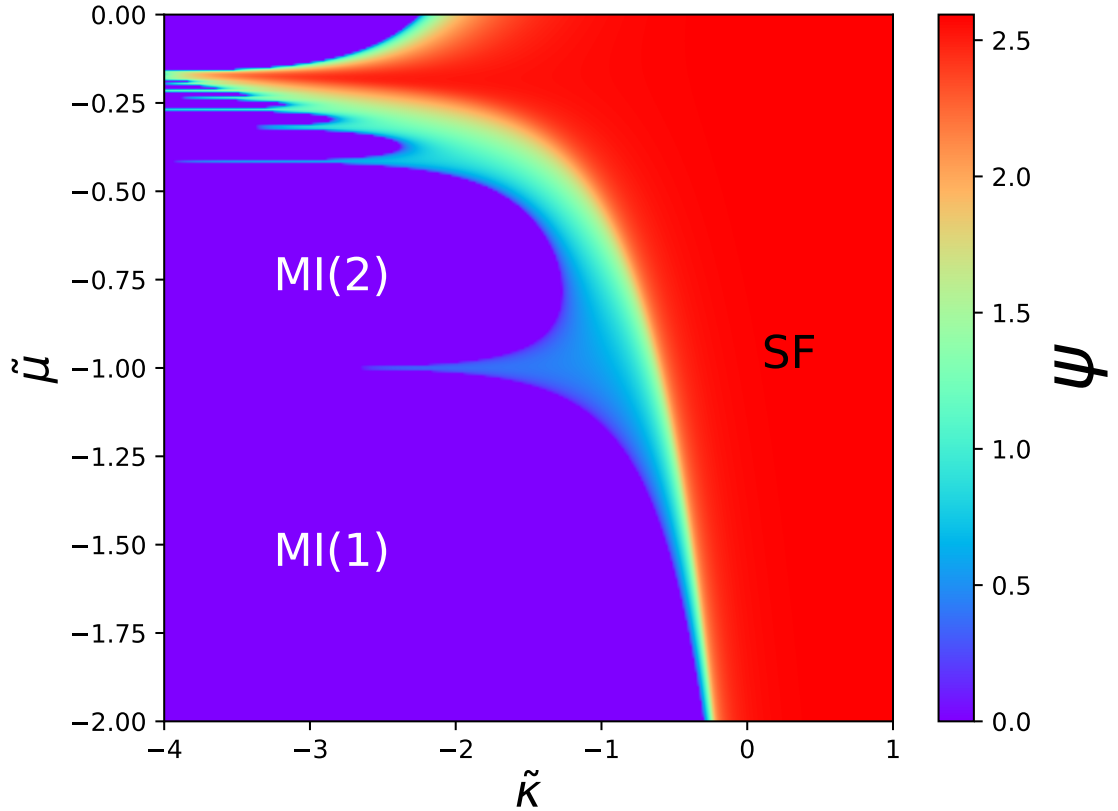


**Figure 1.9:** The mean-field phase diagram of superconducting circuits using transmon as a qubit (1.16) in  $\tilde{\mu} - \tilde{\kappa}$  plane. Here MI( $n$ ) is the MI lobes with  $n$  polaritons.

The polariton number is a conserved quantity of the system as it commutes with the Hamiltonian given in Eq. 1.33. Like the BH model mentioned earlier, the JCH model can also be solved using the single site mean-field approach to obtain the quantum phase transition of polaritons. The mean-field phase diagram is shown in Fig. 1.9 where we observe the phase diagram depicting different Mott lobes of polaritons with integer filling. In recent years several quantum phase transitions have been achieved in the context of superconducting circuits and various experiments have been performed. We will use the Hamiltonian in Eq. 1.33 for studying the QPT in circuit QED systems using transmon.

Motivated by all the recent progress, in this thesis, we explore some of the interesting problems involving interacting bosons in low dimensional lattices. The primary focus of the thesis is to study the ground-state properties of a certain many-body system using different numerical methods. In the following, we provide the outline of the thesis.

## 1.5 Chapterwise outline of the thesis

In Chapter 2, we provide the numerical methods employed to carry out the thesis work. This includes the discussion on the self-consistent cluster mean-field theory (CMFT) approach, exact diagonalization, and the density matrix renormalization group (DMRG) method in the framework of the matrix product states (MPS).

In Chapter 3, we discuss the ground state properties of interacting bosons in bilayer superlattice systems in low dimensions in the presence of interlayer interaction. After briefly introducing the multi-body interacting BH model in a bilayer system and the associated phase transitions, we discuss the details of our findings using the CMFT method. We have further complemented our findings by repeating the calculations in a one-dimensional nonlocally coupled ladder superlattice system using the DMRG method.

In Chapter 4, we study the ground-state properties of constrained bosons in two-leg ladder systems. By assuming different constraints on the legs of the ladder, we explore different phases that may arise due to the competing interactions and hopping strengths along with different constraints. We employ both the CMFT as well as DMRG approach for our exploration.

In Chapter 5, we propose a scheme to study the process of spontaneous photon pair creation and propagation by manipulating an array of coupled transmons mimicking a three-level artificial atom of the  $\Xi$  type. We have used the corresponding Jaynes-Cummings-Hubbard model in one- and two-dimensional arrays using the DMRG and the CMFT approach, respectively, to establish the emergent photon pair propagation in the system.

Chapter 6 highlights the conclusions drawn from our work. This also includes the possible extension of the results discussed in the thesis, as well as a list of new problems that can be done in the future.

## Chapter 2

### Methods

The problems discussed in the thesis involves many particle systems. The exact analytical approach fails to predict the ground state properties accurately. In such a scenario, appropriate numerical methods provide useful insights about such many-body interacting systems. In this chapter, we briefly discuss different numerical methods employed in this thesis. One of the well known numerical methods to solve the Schrodinger equation for many body systems is the exact diagonalization (ED) method. However, the ED method is not suitable for the study of sufficiently large many body system having intricate quantum correlations because the size of the Hilbert space grows exponentially with increasing system sizes. To get rid of this problem, different powerful numerical methods have been formulated for studying QPT, such as the Quantum Monte Carlo (QMC) and the Density Matrix Renormalization Group (DMRG) methods. In this thesis we have employed the DMRG method to study the 1D problems and for the 2D systems, the self-consistent cluster mean field theory (CMFT) approach has been used. As we will discuss below, both the CMFT and DMRG approaches use exact diagonalization as an intermediate step. Therefore, in the following we will discuss the CMFT, ED and the DMRG approaches.

#### 2.1 Mean Field approach

Before proceeding for the CMFT approach, we first highlight the simple site decoupled mean-field theory (SDMFT) approach which is one of the simplest method to capture the qualitative physics of the models with local interaction such as the BH model.

As introduced in Chapter 1, the BH model that describes the systems of inter-

acting bosons on a periodic lattice is given by the following Hamiltonian,

$$H = - \sum_{\langle i,j \rangle} t_{i,j} (a_i^\dagger a_j + H.c.) + \frac{U}{2} \sum_i n_i (n_i - 1) - \sum_i \mu_i n_i \quad (2.1)$$

The ground state of the BH model is known to exhibit the SF-MI phase transition as a function of the ratio  $t/U$  as already mentioned in Chapter 1. Here, we discuss how this can be captured by the SDMFT approach.

In the limit  $U \gg t$ , the hopping term become negligible and the BH Hamiltonian reduces to,

$$H = \sum_i H_i^{(0)} \quad (2.2)$$

where,

$$H_i^{(0)} = \frac{U}{2} n_i (n_i - 1) - \mu_i n_i \quad (2.3)$$

Clearly we can see the eigenstates of the Hamiltonian  $H_i^{(0)}$  are Fock states  $|n\rangle$  with definite number of atoms per site. In absence of tunneling the ground state is provided by the fixed number of atoms per site.

Now we shall employ the standard mean field approximation by introducing the superfluid order parameter,

$$\psi = \langle a_i \rangle \quad (2.4)$$

Using mean-field approximation the offsite terms can be decoupled as [21]

$$a_i^\dagger a_j \approx a_i^\dagger \psi + a_j \psi^* - \psi^* \psi \quad (2.5)$$

With this the BH model takes the form

$$H = \sum_i H_i^{MF}, \quad (2.6)$$

where

$$H_{MF} = \sum_i \left[ \frac{U}{2} n_i (n_i - 1) - \mu n_i - z t (a_i^\dagger \psi + a_i \psi^* - \psi^* \psi) \right] \quad (2.7)$$

is the mean-field Hamiltonian. Here  $z$  is the number of nearest neighbour sites i.e. the lattice co-ordination number. The Hamiltonian  $H^{MF}$  can be solved perturbatively by considering  $H_i^{(0)}$  as the unperturbed part and the rest as the perturbation. Using the second order perturbation theory we obtain the ground state energy of

the system as,

$$\begin{aligned}
 E_g &= \frac{U}{2}n(n-1) - \mu n + tz\psi^2 \left( 1 + tz \left( \frac{n}{U(n-1) - \mu} + \frac{n+1}{\mu - Un} \right) \right) + O(\psi^4) \\
 &= \frac{U}{2}n(n-1) - \mu n + \gamma_n \psi^2 + O(\psi^4)
 \end{aligned} \tag{2.8}$$

Using the Landau theory for phase transition one can arrive at

$$\begin{aligned}
 1 + tz \left( \frac{n}{U(n-1) - \mu} + \frac{n+1}{\mu - Un} \right) &= 0 \\
 \implies \left( \frac{\mu}{zt} \right)^2 + \frac{\mu}{zt} \left[ \frac{U}{zt}(1-2n) + 1 \right] + \left( \frac{U}{zt} \right)^2 n(n-1) + \frac{U}{zt} &= 0
 \end{aligned} \tag{2.9}$$

By simplifying the above quadratic equation one can get,

$$\frac{\mu_{\pm}}{U} = \frac{1}{2} \left[ (2n-1) - \frac{zt}{U} \right] \pm \frac{1}{2} \sqrt{1 - 2\frac{zt}{U}(1+2n) + \left( \frac{zt}{U} \right)^2} \tag{2.10}$$

which gives the behaviour of the chemical potential  $\mu$  as a function of  $zt/U$ . The phase diagram of a  $d$ -dimensional lattice can be obtained by setting appropriate  $z$  in the equation.

Although, the perturbative solution of the MF Hamiltonian is simple, it is also convenient to diagonalize  $H^{MF}$  numerically to obtain the phase diagram. The ground state energy can be obtained as a function of the order parameter  $\psi$  by diagonalizing Eq. 2.7 with truncation on number of bosons per site.

In the numerical approach, we apply an iterative process to obtain the self-consistent value of the superfluid order parameter  $\psi$  for obtaining the ground state of the system. While the presence of non zero superfluid order parameter,  $\psi$  in the system indicates the existence of the SF phase, the zero value of  $\psi$  indicates the system is in the MI phase. One interesting point to notice that the Hamiltonian in Eq. 2.7 breaks the  $U(1)$  global gauge symmetry for any non zero value of  $\psi$ . The resulting phase diagram for the BH model has already been shown in Fig. 1.3 of Chapter 1. The MF theory for the BH model estimates the critical point of the SF-MI transition as  $(U/zt)_c \approx 5.83$ . Note that the simple MF approach is based on dividing the entire Hamiltonian into single site Hamiltonian and as we increase the dimension of the system, the accuracy of the results also increases. The computational complexity of this method is very less since it is formulated from the single site Hamiltonian. However, the single site approach overlooks the off-site correlations which provide many valuable information about the system. Also this

method is not useful in predicting the quantum phase transitions of low-dimensional systems. To circumvent this problem, we implement a modified version of MF theory, known as the Cluster Mean-Field Theory method, which we will discuss in the following section.

## 2.2 Cluster Mean-field Theory (CMFT) approach

In this section we discuss about the CMFT approach in detail. In this approach, the entire many-body system is divided into clusters which are usually small and have finite sizes, as shown in Fig. 2.1 [53]. After dividing the system into small clusters, we apply the ED method for the individual clusters and the MF method [21] for the couplings between the small clusters (dashed links) to solve the Hamiltonian of the entire system.

We divide the hopping term into two parts, one is hopping within the cluster and another part is hopping between the clusters. we treat the hopping within cluster as a part of the exact Hamiltonian and decouple the inter-cluster hopping term. If we divide the entire system into  $N_c$  number of clusters with cluster size  $L$ , then the BH Hamiltonian can be written as,

$$H \approx \sum_{j=0}^{N_c-1} H_{cluster}^j + H_{MF}^j \quad (2.11)$$

The Hamiltonian for a single cluster (taking  $j = 0$ ) can be written as,

$$H_{cluster}^0 = - \sum_{i=0}^{L-1} t_{i,i+1} (a_i^\dagger a_{i+1} + H.c.) + \frac{U}{2} \sum_i^{L-1} n_i (n_i - 1) - \sum_i \mu_i n_i \quad (2.12)$$

Now we look into the mean field part of the Hamiltonian. After applying the transformation  $a_i = \psi_i + \delta a_i$ , the inter-cluster hopping term takes the form,

$$a_i^\dagger a_{j'} + a_{j'}^\dagger a_i \approx a_i^\dagger \psi_{j'} + a_{j'} \psi_i^* - \psi_i^* \psi_{j'} + a_{j'}^\dagger \psi_i + a_i \psi_{j'}^* - \psi_{j'}^* \psi_i \quad (2.13)$$

Here  $i$  denote boundary site of a cluster and  $j'$  denote the boundary sites of the adjacent cluster, boundary site of two different cluster connected via hopping strength  $t_{i,j'}$ . Therefore, the mean field part of the Hamiltonian (4) can be written as,

$$H_{MF} = - \sum_{\langle i,j' \rangle} t_{i,j'} (a_i^\dagger \psi_{j'} + \psi_i^* a_{j'} - \psi_i^* \psi_{j'}) \quad (2.14)$$

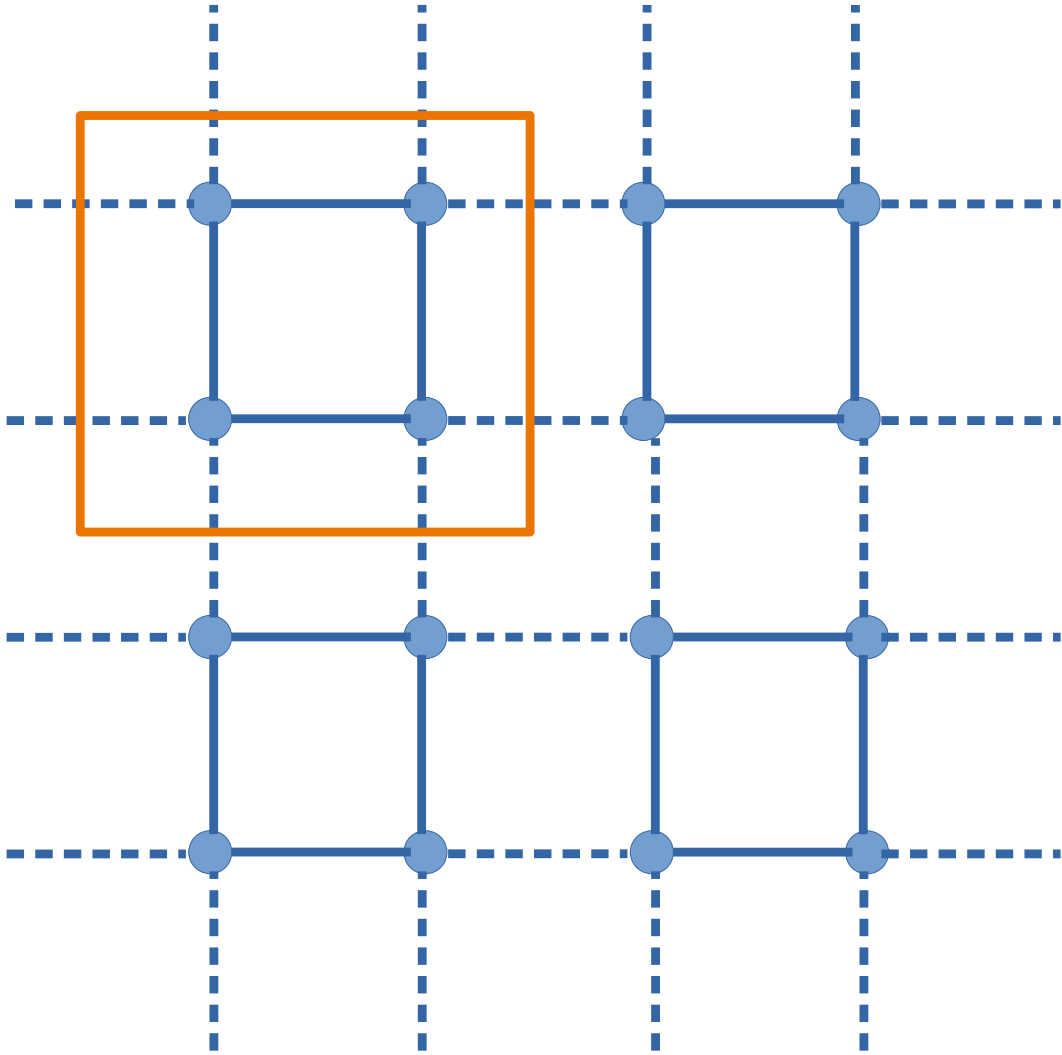


**Figure 2.1:** Division of a two-dimensional square lattice into  $2 \times 2$  clusters. A unit cluster is represented by a dotted box which by repeating in two dimensions forms the entire lattice. We apply the ED method for solid lines and MF approach for dashed lines.

By construction the CMFT approach provides improved accuracy as compared to the SDMFT approach. The former approach incorporates off site correlations which are absent in the latter. This enables to calculate the off-site correlations. Therefore the CMFT method is more powerful than the MF method and one can in principle apply this method to get a qualitative idea of the system. Also it is extremely useful approach to study the simple models like the BH model compared to the sophisticated methods like the Quantum Monte Carlo method as it is simple to implement and requires less computing resources [53–57].

The accuracy of the CMFT approach improves by increasing the cluster size. Since the cluster is treated exactly, efficient ED routine is necessary to achieve larger cluster size and better accuracy. In the following section we will discuss ED approach used in the CMFT method.

### 2.2.1 Exact Diagonalization (ED)

Here we discuss about the ED approach. In principle, the ED method provides us a way to calculate the entire energy spectrum of the Hamiltonian representing a

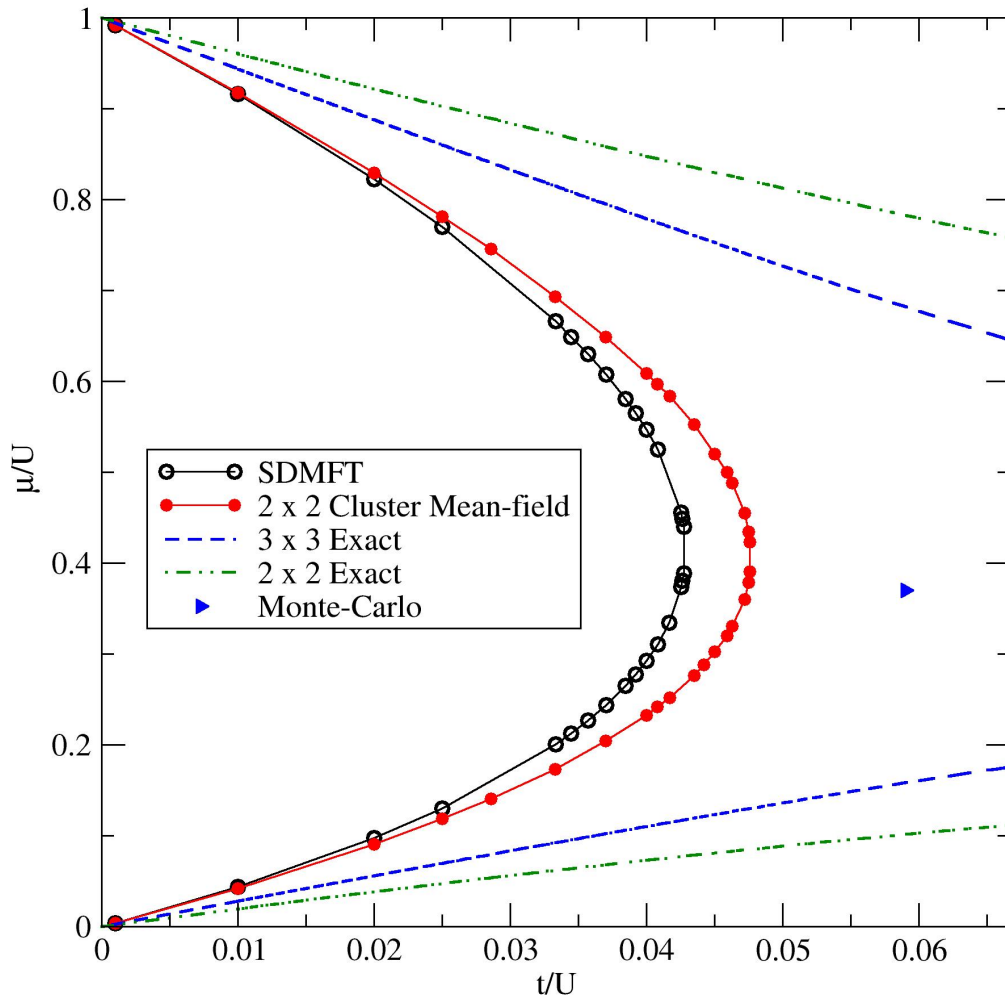


**Figure 2.2:** MI-SF phase boundaries for two dimensional square lattice, calculated using SDMFT(black line), CMFT( $2 \times 2$ , red line), and the exact( $2 \times 2$ , blue and  $3 \times 3$ , green).

particular system with truncation on number of lattice sites and maximum number of particles allowed per site. In ED method we study the models in a canonical ensemble, where total number of particles are fixed. We can define the number operator for total number of particles on lattice as,

$$N_{total} = \sum_i n_i^b \quad (2.15)$$

Where  $n_i^b$  is the number operator for  $i^{th}$  lattice site. The method is formulated in three major steps, first step is to create a suitable basis. For example, if we have a bosonic system in 1D having  $L$  number of lattice sites, then the basis vector can be written as,

$$\{|n_1^b, n_2^b, n_3^b, \dots, n_L^b\rangle\} \equiv |n_1^b\rangle \otimes |n_2^b\rangle \otimes |n_3^b\rangle \otimes \dots \otimes |n_L^b\rangle \quad (2.16)$$

where  $n_i^b$  is the number of particles at  $i^{th}$  site. We use the Fock state basis which spans the complete Hilbert space of the system. And the next steps are to compute the Hamiltonian in the form of a matrix using the basis states and diagonalize the matrix corresponding to the Hamiltonian to obtain the entire eigenspectrum.

Assuming the maximum number of states per site to be  $m$ , the dimension of the entire Hilbert space is  $D = m^L$ , disregarding any symmetry in the system. Due to this exponential growth of  $D$ , storing a single vector representing a large system becomes an impossible task. For example, if we consider  $m = 2$  and  $L = 30$ , it takes about 8GB of memory to store a single vector having  $2^{30}$  dimensions with “double” precision. On the other hand, the order of computational complexity for getting all the eigenstates goes up to  $\mathcal{O}(D^3)$ .

However, with the help of good quantum numbers of the system, one can substantially reduce the dimension of the basis. For example, the total number of particles  $N_{total} = \sum_j n_j^\alpha$  is a conserved quantity because it commutes with the Hamiltonian (1.16) and hence  $N$  is a good quantum number. This assumption enables us to write the Hamiltonian in a block diagonal form so that we can separately solve each block of the Hamiltonian. Although, this process substantially reduces the effective memory and computational cost required for the calculation, but it transforms the Hamiltonian matrix into a matrix with less number of sparse elements. As a consequence, the Hamiltonian takes more time to diagonalize.

To overcome these shortcomings and to make the ED process more efficient, we can use the Lanczos or Arnoldi method. The only constraint of the Lanczos or

Arnoldi method is that it works well only for low-lying states, which is often adequate for essential studies. In this process, we take the Hamiltonian ( $H$ ) and approximate in a  $p$ -dimensional orthonormal basis space which is generated from Krylov space: a vector space that is created by an arbitrary vector  $v$  and the Hamiltonian  $H$ , defined as

$$\{v, Hv, H^2v, H^3v, \dots, H^{p-1}v\}. \quad (2.17)$$

In this newly formed orthonormal basis, the Hamiltonian  $H$  becomes  $\tilde{H}$ . As we increase the value of  $p$ , the largest eigenvalue of  $\tilde{H}$  converges rapidly to the eigenvalues of  $H$ . In general, as long as  $p \ll D$ , the first eigenstate can be obtained with high accuracy. Now, if we increase the value of  $p$  further, we can improve the accuracy of the excited states.

Finally we compare the different methods in the context of the phase diagram of the BH model in Fig. 2.2. Here we only show the first Mott lobe ( $0 \leq \mu/U \leq 1$ ). We have obtained this result by considering the BH model in a 2D square lattice. It can be seen that the phase boundary obtained by using the CMFT approach (red filled circles) with a  $2 \times 2$  cluster is more accurate compared to the SDMFT result (black open circles) method. This accuracy increases with increase in cluster size. For comparison the tip of the Mott lobe from the QMC simulation is depicted as a triangle. We also show the ED results with  $2 \times 2$  (green dot-dashed) and  $3 \times 3$  (blue dashed) lattices which are far from the QMC result due to finite system sizes.

## 2.3 Density matrix renormalization group (DMRG)

The exponential growth in the Hilbert space dimensions with increasing system size makes the computations with ED method intractable. The numerical renormalization group (NRG) [58] method proposed by Wilson and Steve White's density matrix renormalization group (DMRG) [59, 60] method reduce the Hilbert space size significantly, yet retain the low energy properties. The NRG method traces out the high energy information and keeps the low lying states. Although this method is successful in studying the Kondo impurity problem, it fails to work well for other lattice models like Heisenberg model. Steve White's idea was to do the truncation with ground state density matrix instead since the low lying information for one-dimensional systems lies in the density matrix projection. The DMRG algorithm splits into two approaches, infinite DMRG and finite DMRG. The idea with infinite DMRG is to grow the superblock (system block + environment block) to the same

size as the lattice to compute the ground state energy whereas in the finite DMRG, the superblock is acted upon to make further improvements in the ground state properties. The infinite DMRG for a system of size  $L$  is performed follows:

1. Define all the operators for single-site Hamiltonian having Hilbert space of dimension  $d$ .
2. Construct the system and environment blocks by adding single sites to each block with the use of two-site connection operators. The respective Hamiltonian take the forms of  $H_{l+1}^S$  and  $H_{l+1}^E$ , where  $H_l$  is the Hamiltonian corresponding to  $l$  number of sites.
3. Form the superblock by connecting  $H_{l+1}^S$  and  $H_{l+1}^E$ .
4. Find out the ground state eigenvector  $|\psi\rangle$  by diagonalizing the superblock Hamiltonian.
5. Determine the reduced density matrix corresponding to the system and environment blocks.
6. Diagonalize the density matrix and construct the matrix  $O$  with lowest  $m$  eigenvectors  $V$  as

$$\begin{pmatrix} \vdots & \vdots & & \vdots \\ V_1 & V_2 & \dots & V_m \\ \vdots & \vdots & & \vdots \end{pmatrix}.$$

7. Transform the Hamiltonian and other operators using  $O$  as  $\tilde{H}_{l+1}^S = O^\dagger H_{l+1}^S O$  and  $\tilde{A}_{l+1}^S = O^\dagger A_{l+1}^S O$  respectively.
8. Create a new superblock by adding two sites in each iteration and repeat from step 3 until the desired superblock size is achieved.

The finite DMRG starts with infinite DMRG algorithm to cover the full system size. Here the superblock is constructed from a system block of size  $l$ , an environment block of size  $l'$  and two sites in the middle. The algorithm runs as follows:

1. Perform the infinite DMRG algorithm and store all the  $\tilde{H}_l^S$  and  $\tilde{H}_l^E$  matrices in each step until you reach to the desired system size  $L$ .

2. When the system size is  $L = l + 2 + l'$ , grow the system block in expense of the environment block. This step starts with  $l = L/2$  and  $l' = L/2 - 2$ .
3. Follow step 3-7 of the infinite DMRG algorithm until you reach to the right edge where  $l' = 1$ . This is known as right sweep.
4. Now start growing the environment block in expense of the system block until you reach to the left edge where  $l = 1$ . This is known as left sweep.
5. Sweep back and forth until the desired accuracy of the ground state energy is achieved or the specified number of sweeps is performed completely.

The DMRG method is a successful method to study the ground state properties of one-dimensional systems. Östlund and Rommer discovered that DMRG can be represented in terms of matrix product states (MPS) [61, 62] formalism which provides much more flexibility to the algorithm. One can write the most general wavefunction for a one-dimensional system having  $L$  sites as

$$|\Psi\rangle = \sum_{s_1, \dots, s_L} c_{s_1 \dots s_L} |s_1, \dots, s_L\rangle \quad (2.18)$$

where  $\{s_i\}$  are the local state spaces spanned in  $d$ -dimensions and  $i$  is the site index. The idea with this formalism is to write a general wavefunction in terms of an MPS. One can write the coefficients in Eq. 2.18 as a product of matrices  $A$  represented in Eq. 2.19.

$$|\Psi\rangle = \sum_{s_1, \dots, s_L} \sum_{a_1, \dots, a_{L-1}} A_{a_1}^{s_1} A_{a_1, a_2}^{s_2} \dots A_{a_{L-2}, a_{L-1}}^{s_{L-1}} A_{a_{L-1}}^{s_L} |s_1, \dots, s_L\rangle. \quad (2.19)$$

Here  $a_i$  are known as a bond or virtual or auxiliary indices. Similarly, the Hamiltonian of a system can be written in terms of matrix product operators (MPOs) and the ground state energy is computed using the variational approach by contracting the MPOs with an MPS and its conjugate.

The algorithm based on MPS is versatile for computation of quantum many body states where one can introduce enough entanglement to create a local Hamiltonian by playing with the size of the matrices but keeping the matrix dimensions small enough to make the computations easy. This can be done by fixing the bond dimension,  $\chi$ , which is equivalent to  $m$  in the classical DMRG method.

## Chapter 3

# Mott insulator phases of non-locally coupled bosons in bilayer optical superlattices

### 3.1 Introduction

As discussed in Chapter 1, the study of quantum phase transitions in systems of ultracold quantum gases in optical lattices have revealed a host of new phenomena in recent years. The state-of-the-art experimental setups and the flexibility to control the system parameters in such systems have provided a new platform to explore interesting phenomena in nature which has led to a plethora of novel and exciting physics. While the dominant interaction in such ultracold systems is the two-body contact interactions, it has been shown that there exist higher order local interactions as well, which have non-negligible effects on the ground state properties [63, 64]. Recently it was shown that the leading multi-body interactions, such as the three-body interaction, can be engineered under suitable conditions in optical lattices [65–68] which can play important roles in discovering many-body induced quantum phases, especially at higher densities [69–76]. Such many-body interactions can drastically modify the behaviour of the system. For instance, the three-body interaction can become very large leading to the three-body hardcore constrained where not more than two particles can occupy a single site. This feature is crucial in studying the systems of attractive bosons in optical lattices by preventing the collapse of bosons. These three-body constrained bosons (TBCs) are shown to exhibit the superfluid to pair-superfluid (PSF) phase transition in optical lattice [77]. Similar situation is also seen in the regime of large onsite two-body repulsion where no

two bosons can simultaneously occupy a single site. In such a situation the bosons are called the hardcore bosons(HCBs) or the Tonk's gas [78].

On the other hand long-range dipolar interactions in atoms, molecules and Rydberg atoms have culminated into a completely new realm of physics where several novel phenomena have been predicted and observed in recent experiments such as the CDW phases, the exotic supersolid phases and self-bound quantum droplets [79–83]. Interestingly, these non-local interactions have shown to couple systems which are spatially separated from each other such as the bilayer systems and two leg ladders. In such a scenario one can drive the two decoupled systems together with the help of the long-range dipole-dipole interaction [84–87]. Moreover, the bilayer systems with inter-layer interactions resemble systems of two component atomic mixtures in optical lattices. A new area of research has evolved in the context of the dual species bosons, fermions as well as Bose-Fermi mixtures due to the recent advancement in cooling and trapping of binary mixtures in experiments [88–97]. The creation and manipulation of such dual-species mixtures with completely two different species of atoms or two hyperfine states of a particular species in optical lattices to achieve strong correlations have opened up various avenues in addressing complex many-body systems. The presence of different types of interactions compared to the single species systems have made the binary mixture a topic of great interest, as a result several theoretical predictions and experimental observations have been made in various context [92, 94–96, 98–108]. At the same time the creation of optical superlattices [109, 110] have proven to provide an additional flexibility to manipulate lattice potentials and periodicity which results in different interesting applications. A great deal of research has been done on optical superlattices and several new phases have been predicted in theory and observed in experiments on various context [73, 109–120]. Although various investigations have been made in systems of ultracold quantum gases in optical superlattices, the study of bilayer superlattice or binary mixture in superlattices may lead to novel phenomena. As the systems of dual species mixture can be mapped to the spin systems under proper conditions, it promises a direct connection to the many-electron systems and magnetism [121]. One such recent studies on multi-component bosons in optical superlattices has predicted various gapped phases using the single site mean-field approximation where the bosons are assumed to be softcore in nature and the intra-species interactions are considered to be of identical strength [122]. As a result the influence of one species of atoms on the other and vice-versa is similar in nature.

In this chapter we consider a bilayer bosonic system in optical superlattice as

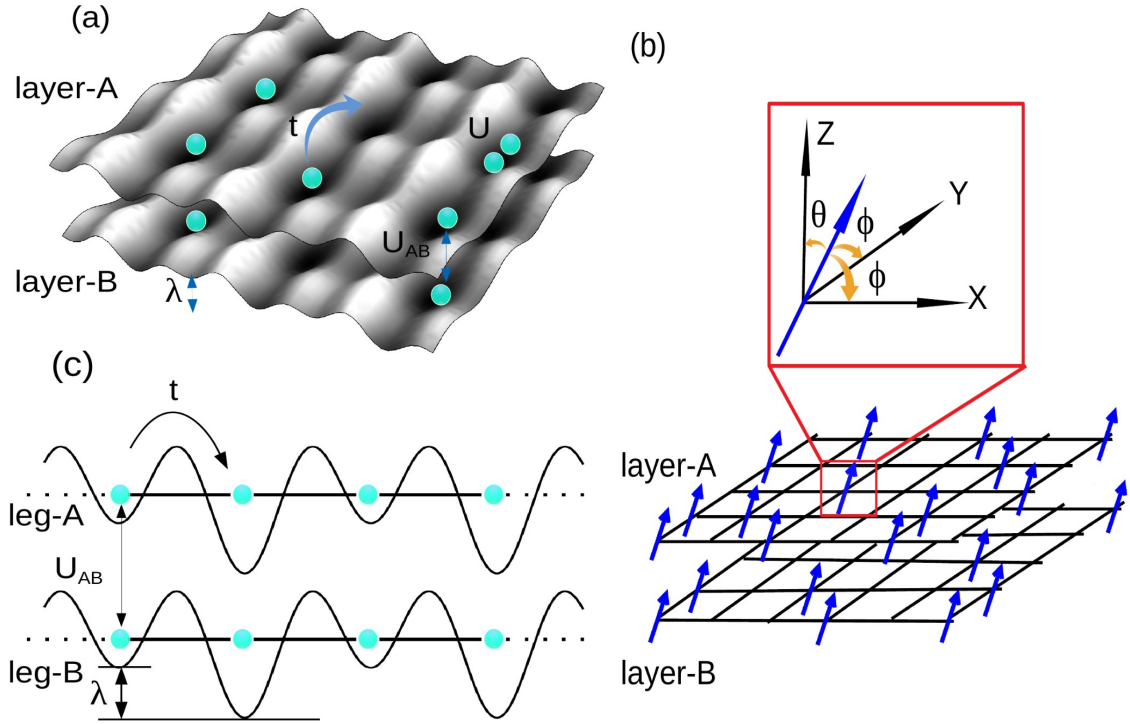


**Figure 3.1:** (a) Illustration of a bilayer superlattice having periodicity equal to two showing the intra-layer and inter-layer interactions. (b) The possible alignment of the dipoles in this bilayer system. In the inset we have shown one dipole placed in the origin in such a way that it makes an angle  $\phi$  with the  $x$  and  $y$  axes and  $\theta$  with the  $z$  axis. (c) Two leg optical superlattice with leg-A and leg-B containing the softcore bosons and constrained bosons respectively. These two legs interact among themselves via the non-local interaction  $U_{AB}$ .

depicted in Fig. 3.1 (a). The construction of the bilayer system is in such a way that both the layers are identical to each other in terms of lattice translation and a two-period superlattice potential is present only along the  $x$ -direction. As a result, the lattice periodicity is doubled in the  $x$ -direction whereas along the  $y$ -direction there is no change in the periodicity. In principle, one can consider the superlattice potential along both the directions which is expected to exhibit similar particle dynamics in both the directions. However, the choice made in this work provides a situation where the particles tend to localise in every alternate sites due to the superlattice potential along one direction whereas they are free to move on the other direction. In such a system we consider the bosons in layer-A to be of softcore in nature whereas bosons in layer-B experience two or three-body hardcore constraint.

We assume the particles are dipolar in nature in both the layers and there exist only inter-layer interactions and the intra-layer interactions are suppressed. This situation can be achieved by orienting the dipoles in such a way that they are at

magic angles with the line joining two nearest neighbour dipoles along both  $x$ - and  $y$ -directions of the layer. In such a scenario, the angle made with the line joining the dipoles sitting in two different layers are different from the magic angle resulting in a finite repulsive interaction which is proportional to  $(1 - 3\cos^2\theta)$  as depicted in Fig. 3.1(b). Moreover, the distance between the layers can also be varied to tune the inter-layer interaction. Since intra-layer (contact) and inter-layer (long-range) interactions originate from different physical phenomenon, it is possible to tune them independently. The model which describes such system is the modified Bose-Hubbard model given as:

$$H = -t \sum_{\langle i,j \rangle, \sigma \in [A, B]} (a_{i\sigma}^\dagger a_{j\sigma} + H.c.) + \sum_{i, \sigma \in [A, B]} \left[ \frac{U_\sigma}{2} n_{i\sigma} (n_{i\sigma} - 1) - (\mu_\sigma - \lambda_i) n_{i\sigma} \right] + \frac{W_\sigma}{6} \sum_{i, \sigma \in [A, B]} n_{i\sigma} (n_{i\sigma} - 1) (n_{i\sigma} - 2) + U_{AB} \sum_i n_{iA} n_{iB} \quad (3.1)$$

Here,  $a_{i\sigma}^\dagger$  ( $a_{i\sigma}$ ) is the creation (annihilation) operator which creates (destroys) a boson in layer  $\sigma$  ( $= A, B$ ) and at site  $i$ ,  $n_{i\sigma} = a_{i\sigma}^\dagger a_{i\sigma}$  is the number operator and  $t$  is the hopping amplitude between any two nearest neighbour sites  $i$  and  $j$ . While  $U_\sigma$  represents the local two-body intra-layer interactions,  $W_\sigma$  represents the local three-body intra-layer interactions,  $U_{AB}$  represents the inter-layer two body interaction.  $\mu_\sigma$  is the chemical potential and  $\lambda_i$  is the superlattice potential along the  $x$ -direction which is  $0$  ( $\lambda$ ) for odd (even) site indices as shown in Fig. 3.1(a). The two- and three-body constraints in layer-B are achieved by considering  $(a^\dagger)^2 = 0$  and  $(a^\dagger)^3 = 0$  respectively. Note that for the HCBs in layer-B,  $U_{\sigma=B} \rightarrow \infty$  and the terms associated to  $U_{\sigma=B}$  will vanish in model(3.1) due to the hardcore constraint. It is to be noted that the presence of a finite local three-body interaction mainly modifies the superfluid-Mott insulator transition critical points and it has been investigated in detail in other works. Therefore, we discuss the case in which the contribution from the three-body and higher order terms is neglected in layer-A. The three-body hardcore constraint is achieved by considering  $W_\sigma \rightarrow \infty$  in layer-B. For a large superlattice potential each two-site unit cell can effectively behave like a single-site. In such a scenario, depending on the number of particles in the deep site and the effective repulsive interaction, the on-site Wannier orbitals get affected leading to effective modification of the tunneling and on-site interaction. However, in our calculations we do not include these modifications and limit our analysis to the standard Bose-Hubbard model.

## 3.2 Method

We investigate the ground state properties of the model given in Eq. (3.1) by considering softcore bosons in layer-A whereas loading layer-B with HCBs and TBCs separately in two different scenarios. In both the cases we study the phase diagram of the system and obtain various gapped phases which appear at commensurate as well as incommensurate densities. We also show how the tip positions of these gapped phases or in other words the gapped to gapless phase transitions behave by changing the constraint on the bosons in layer-B. To this end we implement the CMFT approach to analyse the physics of Eq. (3.1). It is to be noted that this problem can also be analysed using the simple mean-field decoupling approximation [21] which can capture the qualitative physics of the system. However, in order to achieve better accuracy we employ the CMFT approach. For the models like the one shown in Eq. (3.1), the CMFT method works fairly well with less computational complexities and may approach in the thermodynamic limit the Quantum Monte Carlo results for some specific situations [87, 123, 124]. In the end we investigate the scenario for the one dimensional case to examine the fate of quantum phases in reduced dimension. In this regard, we utilise the well known density matrix renormalization group (DMRG) method for the two-leg ladder model to examine the features in one dimension.

With the CMFT approximation the original Hamiltonian of Eq. (3.1) can be written as

$$H = H_C + H_{MF} \quad (3.2)$$

where  $H_C(H_{MF})$  is the cluster(mean-field) part of the Hamiltonian.  $H_C$  is same as Eq. (3.1) but is limited to the cluster only. Introducing the two layer-dependent SF order parameters as  $\psi_{i\sigma} = \langle a_{i\sigma}^\dagger \rangle = \langle a_{i\sigma} \rangle$  and using the mean-field decoupling approximation as introduced in Chapter 1, we write  $H_{MF}$  as

$$H_{MF} = -t \sum_{\sigma, \langle i, j \rangle} [(a_{i\sigma}^\dagger + a_{i\sigma})\psi_{j\sigma} - \psi_{i\sigma}^* \psi_{j\sigma}] \quad (3.3)$$

In our calculation we have set  $t = 1$  to make all the physical quantities dimensionless. For the CMFT calculation we use a four sites cluster which consists of two sites from both the layers. We call this a supercell in the following discussion. We define the quantity  $n = \sum_{\sigma \in [A, B]} \sum_{i=1}^2 n_{i\sigma}$  and  $\rho = \frac{1}{4}n$  which are the total particle number and density in one supercell to distinguish various phases. We also assume equal

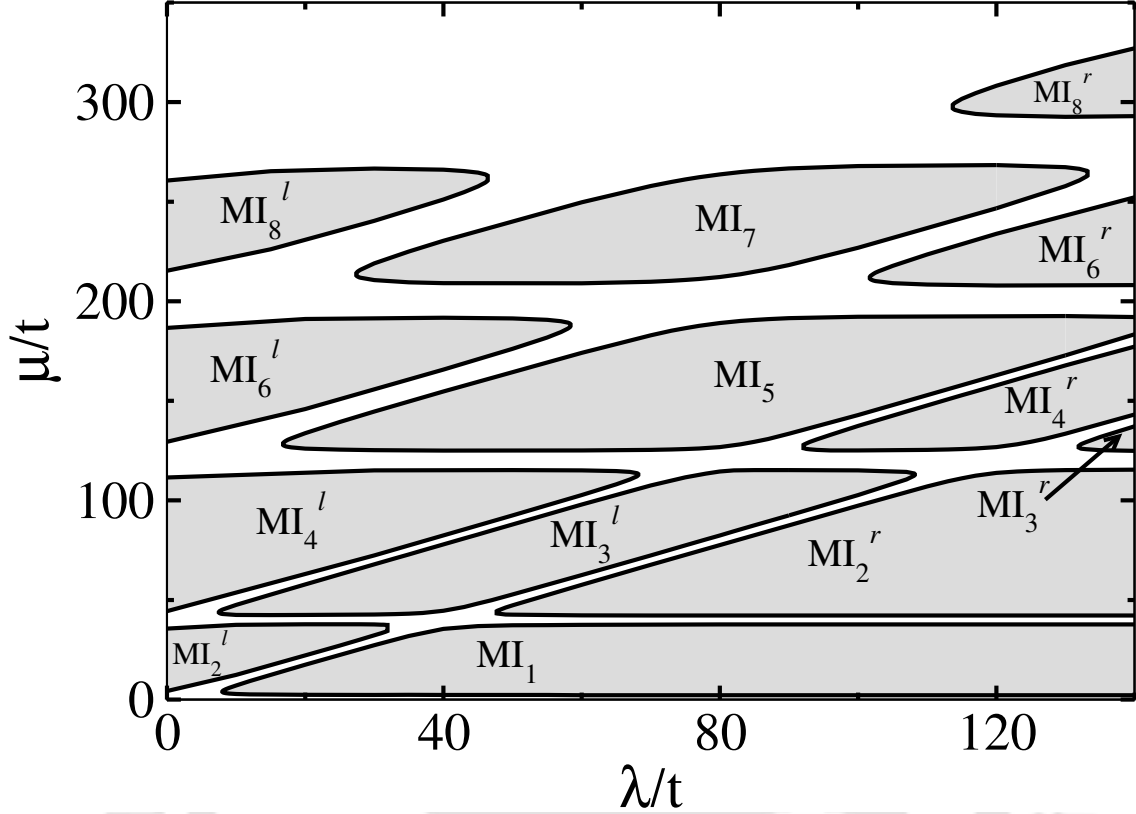


**Figure 3.2:** The CMFT phase diagram when bosons in layer-A are softcore and in layer-B are HCBs. Here  $U_A = 80$  and  $U_{AB} = 40$ .

chemical potentials for bosons in both the layers by making  $\mu_A = \mu_B = \mu$  in our calculation. By fixing the values of  $U_A$ ,  $U_B$  (in case of TBCs) and  $U_{AB}$  we compute the complete phase diagram in the  $\mu/t$  vs.  $\lambda/t$  plane. We also consider some specific values of lambda and vary the interactions to obtain the phase diagram as done in Ref. [122].

Further we analyse the system in one dimension by considering a two-leg ladder which can be viewed as two superlattice chains coupled via the dipole-dipole interaction. We study the model(Eq. (3.1)) by using the DMRG method based on MPS. In our DMRG calculation we assume system sizes up to 100 sites and bond dimension of 500. The cluster and system size considered in our calculation are found to be sufficient to capture the physics we are interested in.

## 3.3 Results and Discussion

### 3.3.1 Hardcore constraint for bosons in layer-B

In this part, we discuss the case when the bosons in layer-B are hardcore in nature. In the decoupled layer limit i.e.  $U_{AB} = 0$ , both the layers behave as independent two dimensional ( $2d$ ) systems. It is well known that there exists a critical value of  $\lambda$  for which the system undergoes an SF to MI transitions at half filling for both hardcore and softcore bosons in  $2d$  [73, 115, 125]. Therefore, it is expected that the first Mott lobe would appear in the system after a critical value of  $\lambda$  for density  $\rho = 1/4$  where any one of the layers attains half filling. At this stage the inter-layer interaction  $U_{AB}$  has no role on the phase diagram as the particles reside in any one of the layer. However, with the increase in the chemical potential  $\mu$  both the layers get populated and one may see interesting interplay between  $U_A$ ,  $U_{AB}$  and  $\lambda$  which leads to various gapped phases and transitions to the SF phase at different integer and non integer fillings of individual layers as shown in Fig. 3.2. In this chapter we call all the gapped phases the MI phases although the ones at non integer densities are different from the usual MI phase where each site is occupied with same integer number of bosons [111]. However, in the case of superlattices, one can consider the density with respect to the unit-cell (the periodicity of the superlattice) so that the gapped phases at non integer densities can be called as the MI phases for those particular densities.

The phase diagram of Fig. 3.2 is obtained by self consistently diagonalizing the Hamiltonian shown in Eq. (5.3) to obtain the ground state wave function and then the superfluid order parameter  $\psi$  as discussed in the previous section. By considering a large onsite interaction  $U_A = 80$  and  $U_{AB} = U_A/2$  which is sufficient to establish various gapped phases for the softcore bosons in one layer and by varying  $\lambda$  for a wide range of values, we obtain the entire phase diagram which consists of the gapped MI lobes and the intermediate SF phases. Here we define the superfluid density  $\rho_s = \frac{1}{4} \sum_{i,\sigma} |\psi_{i\sigma}|^2$ , where  $\psi_{i\sigma}$  is the layer dependent superfluid order parameter as discussed in the previous section. The gapped phases are obtained by looking up the regions in which the total superfluid density vanishes in the  $\rho_s$  vs  $\mu/t$  plot for several values of  $\lambda$ . In Fig. 3.3 we show  $\rho$  (solid blue line) and  $\rho_s$  (dashed green line) with respect to  $\mu/t$  for  $\lambda = 10, 70, 140$  which cut through the gapped phases in Fig. 3.2 parallel to the  $\mu/t$  axis. It can be seen that for a particular  $\lambda$ , as  $\mu$  increases the plateaus in  $\rho$  appear and at the same time  $\rho_s$  vanishes corresponding to the MI phases. We denote the MI phases as  $MI_n$  where the subscript  $n$  indicates the

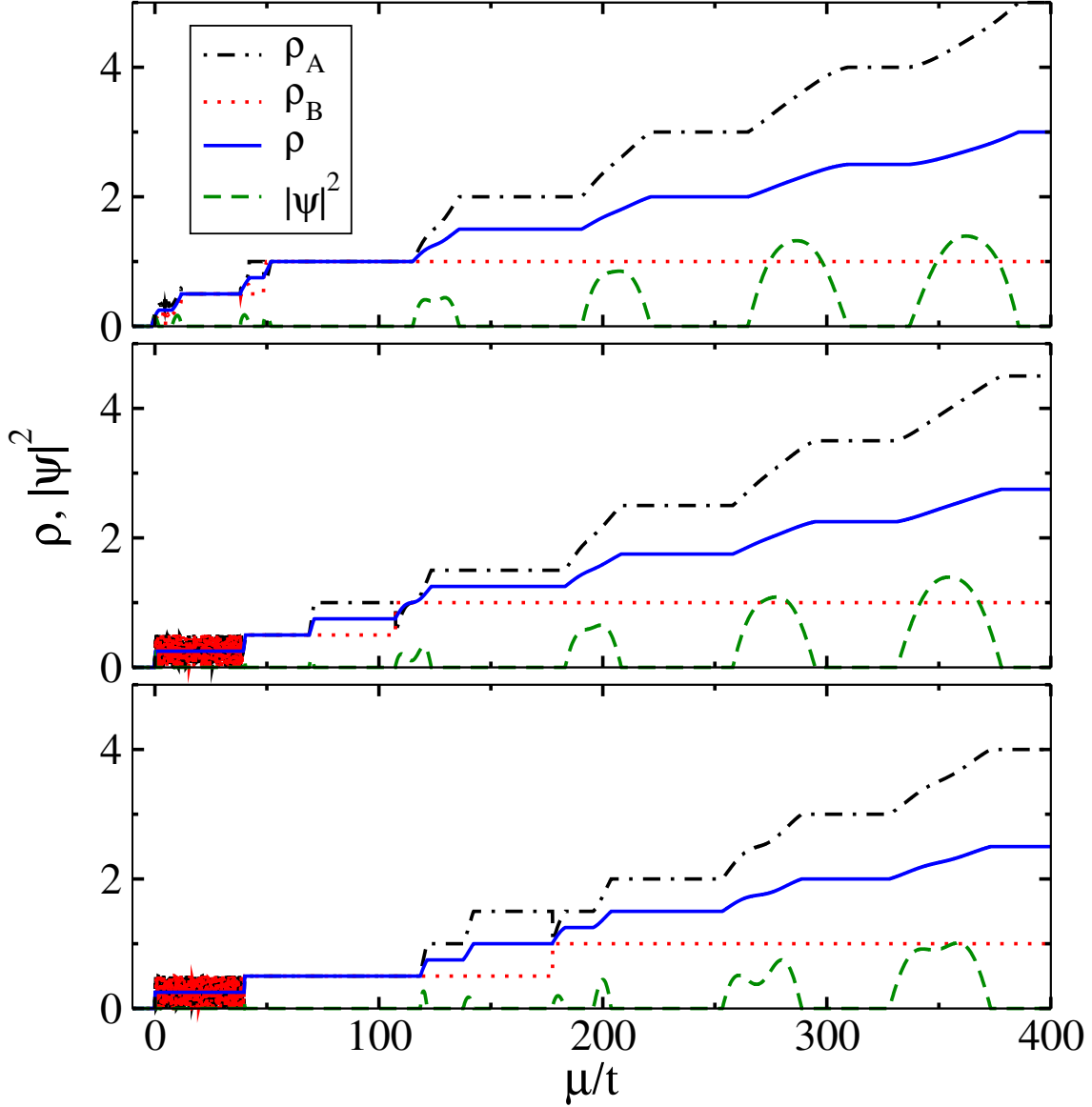


**Figure 3.3:** Variation of  $\rho$  (solid blue curve) and  $|\psi|^2$  (dashed green curve) with respect to  $\mu/t$  for  $\lambda = 10, 70, 140$  shows the gapped and gapless phases when layer-B has HCBs. The plateaus in  $\rho$  correspond to the gap in the MI phases whereas the shoulders around the plateaus (where the values of  $|\psi|^2$  are finite) indicate the gapless SF phase. We also plot the individual layer densities as  $\rho_A$  (dot dashed curve) and  $\rho_B$  (dotted curve) for clarity. Due to the hardcore nature  $\rho_B$  saturates at one. The fluctuations in  $\rho_A$  and  $\rho_B$  are due to the degenerate states in the CMFT calculation.

total number of particles i.e.  $n_A + n_B$  in a supercell. The possible supercell atom distribution for all the MI phases are presented in Table. I.

It can be seen from Fig. 3.2 that the first lobe which corresponds to the  $MI_1$  appears after a critical  $\lambda \sim 8$  at  $\rho = 1/4$  as discussed before. The gap continues to be finite and the lobe expands as  $\lambda$  increases further. Upon increasing the value of  $\mu$

**Table 3.1:** Table depicting various MI states when atoms in layer-B are HCBs. Each state shows the density distribution in the supercell corresponding to a particular MI state for a given  $n$  and  $\rho$ .

Boson distribution in the unit cell		
n	$\rho$	Supercell Configuration
1	0.25	$MI_1 = \begin{vmatrix} 0 & 1 \\ 0 & 0 \end{vmatrix} \rangle$ or $MI_1 = \begin{vmatrix} 0 & 0 \\ 0 & 1 \end{vmatrix} \rangle$
2	0.5	$MI_2^l = \begin{vmatrix} 0 & 1 \\ 1 & 0 \end{vmatrix} \rangle$ or $MI_2^l = \begin{vmatrix} 1 & 0 \\ 0 & 1 \end{vmatrix} \rangle$ and $MI_2^r = \begin{vmatrix} 0 & 1 \\ 0 & 1 \end{vmatrix} \rangle$
3	0.75	$MI_3^l = \begin{vmatrix} 1 & 1 \\ 0 & 1 \end{vmatrix} \rangle$ and $MI_3^r = \begin{vmatrix} 0 & 2 \\ 0 & 1 \end{vmatrix} \rangle$
4	1.0	$MI_4^l = \begin{vmatrix} 1 & 1 \\ 1 & 1 \end{vmatrix} \rangle$ and $MI_4^r = \begin{vmatrix} 1 & 2 \\ 0 & 1 \end{vmatrix} \rangle$
5	1.25	$MI_5 = \begin{vmatrix} 1 & 2 \\ 1 & 1 \end{vmatrix} \rangle$
6	1.5	$MI_6^l = \begin{vmatrix} 2 & 2 \\ 1 & 1 \end{vmatrix} \rangle$ and $MI_6^r = \begin{vmatrix} 1 & 3 \\ 1 & 1 \end{vmatrix} \rangle$
7	1.75	$MI_7 = \begin{vmatrix} 2 & 3 \\ 1 & 1 \end{vmatrix} \rangle$
8	2.0	$MI_8^l = \begin{vmatrix} 3 & 3 \\ 1 & 1 \end{vmatrix} \rangle$ and $MI_8^r = \begin{vmatrix} 2 & 4 \\ 1 & 1 \end{vmatrix} \rangle$

or in other words by increasing the particle number in the system, the other gapped phases start to appear, which are seen as plateaus in the  $\rho$  vs.  $\mu/t$  plot shown in Fig. 3.3. For total density  $\rho = 1/2$  (half filling of both the layers), there exists two gapped lobes separated by the SF phase as a function of  $\lambda$ . The appearance of large gap at vanishing  $\lambda$  can be attributed to the effect of  $U_{AB}$  which prevents the atoms in layer-A and layer-B to occupy the same sites. Hence, one may expect a gapped phase which is similar to the checker-board solid for the Bose-Fermi mixture on a square lattice [126]. We call this phase as the  $MI_2^l$  phase. As discussed in Ref. [126], the stability of this gapped phase depends on the ratio  $U_{AB}/U_A$ . In our case  $U_{AB}/U_A = 0.5$ , which is sufficient to open a gap in the system. However, the gap gradually decreases as the value of  $\lambda$  increases and as a result the system enters into the SF phase. This is because of the increase in the effective onsite potential in every alternate sites on both the layers which results in a smaller ratio  $U_{AB}/U_A$ . Increasing the value of  $\lambda$  further, the gapped phase reappears after a critical  $\lambda \sim 47.6$ . At this stage, the superlattice potential is very strong compared to the ratio  $U_{AB}/U_A$  and the bosons reside in the deep lattice sites. We call this gapped phase the  $MI_2^r$  phase which is similar to the striped phase for the  $2d$  case.

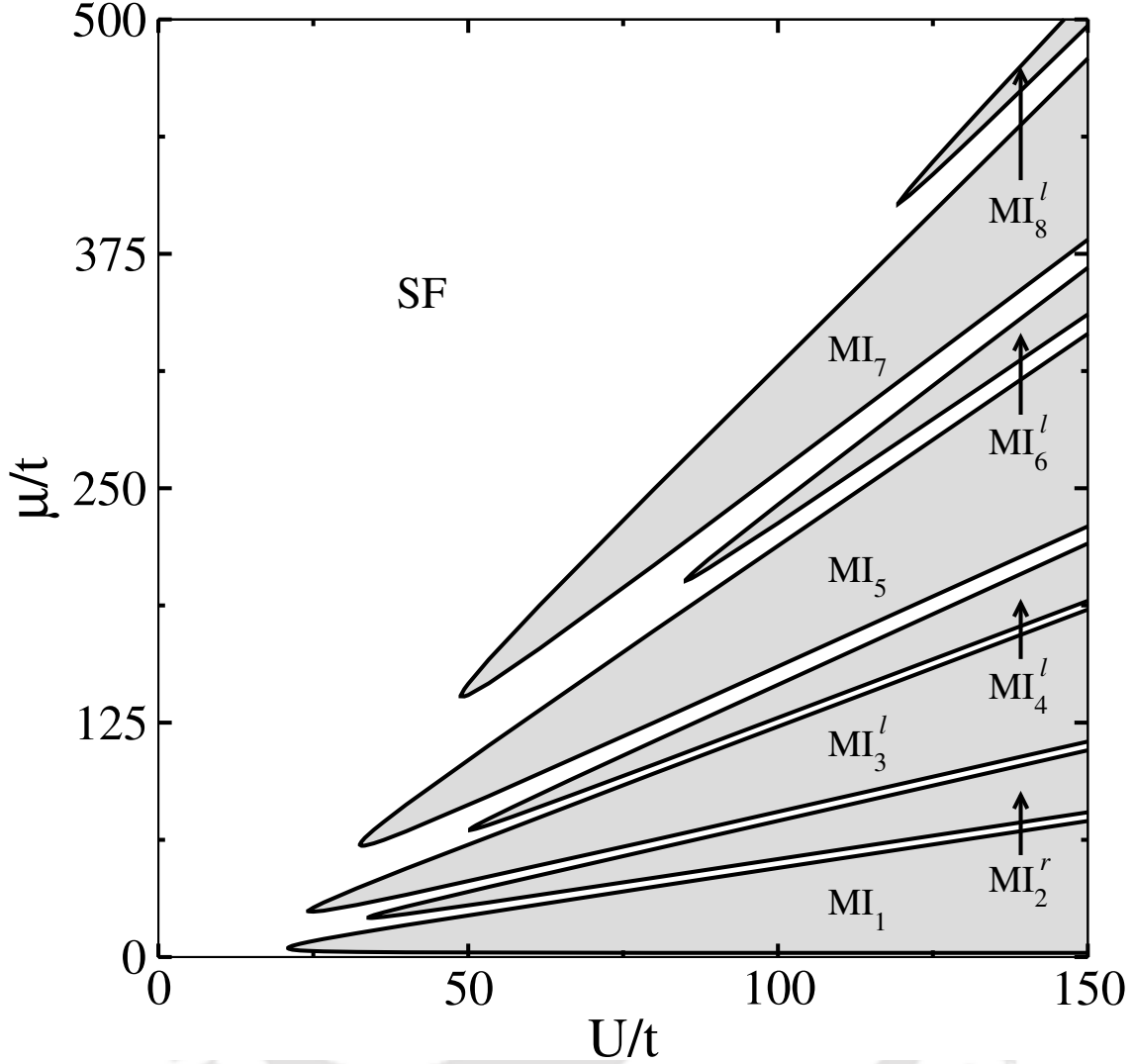


**Figure 3.4:** CMFT phase diagram in the  $\mu/t$  vs.  $U/t$  plane when bosons in layer-A are softcore and in layer-B are hardcore in nature. Here  $U_A = U = 80, U_{AB} = 40$  and  $\lambda = 60$ . Since  $U_A$  is fixed in the case, we vary  $t$  in order to tune the ratio  $U/t$ .

The density distribution can be seen from the  $\rho$  vs.  $\mu/t$  plot as shown in Fig. 3.3(see figure for detail).

At this stage further increase in density results in the next gapped phases at  $\rho = 3/4$ . The situation at this density is completely different from the case of half density. Here we find that the system is initially in the gapless SF phase for a range of  $\lambda$  starting from  $\lambda = 0$  and there exists a gapped island for some intermediate range of  $\lambda$  and then a gapped phase for the large values of  $\lambda$ . The physics at this density can be understood by the following analysis. For  $\lambda = 0$ , as  $\mu$  increases the layer-A will start to get populated first due to the softcore nature and all the sites are occupied by one atom each giving rise to unit filling and the layer-B remains

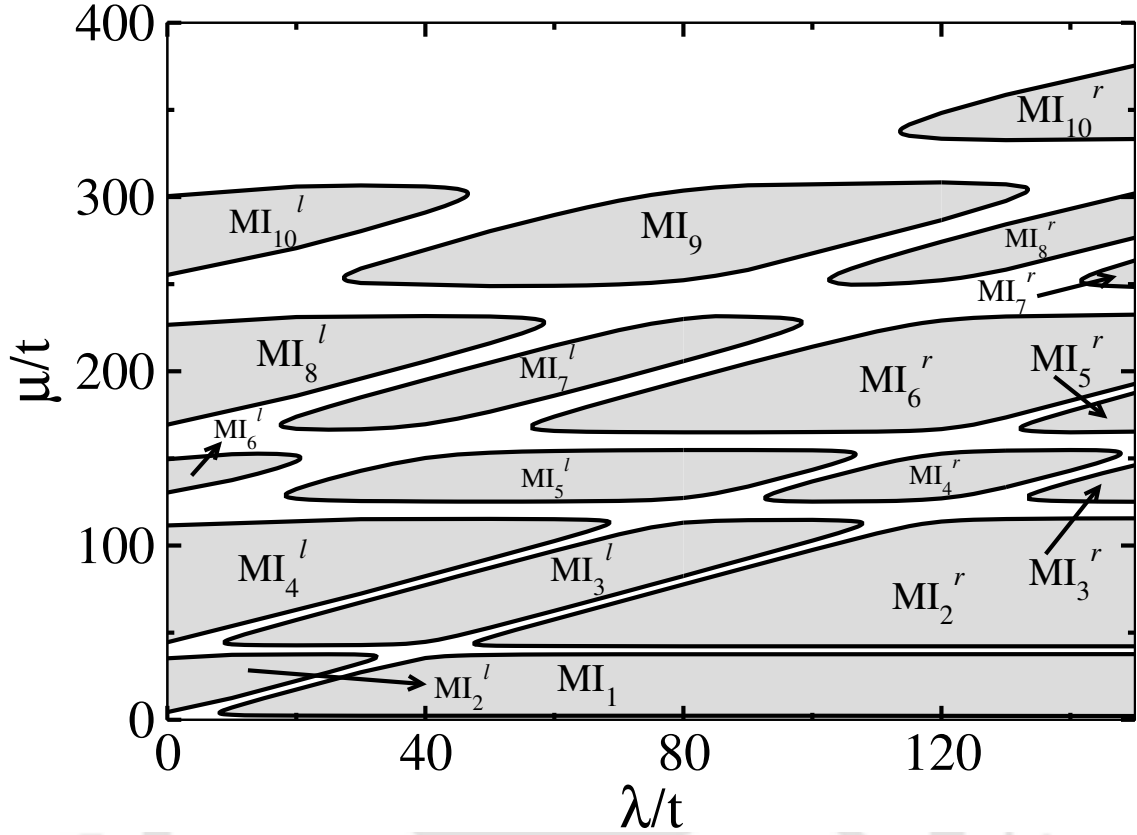


**Figure 3.5:** CMFT phase diagram when bosons in layer-A are softcore and in layer-B are TBCs. Here  $U_A = U_B = 80$  and  $U_{AB} = 40$ .

at half filling. At unit filling the layer-A is in the MI phase as  $U_A$  is sufficiently strong. As a result, the atoms in layer-B will experience equal repulsion  $U_{AB}$  from all the sites of layer-A and hence they can move freely giving rise to the SF phase of layer-B. Therefore, the system as a whole is gapless although layer-A is in the MI state. The increase in  $\lambda$ , however, introduces the gap in the system by localising the hardcore bosons into the deep sites of layer-B while the layer-A remains in the MI phase. The resulting system is therefore, a gapped phase. This phase is called the  $MI_3^l$  phase which lies between  $\lambda \sim 7.5$  and  $\lambda \sim 108.4$ . Further increase in  $\lambda$  leads to increase in particle-hole fluctuation and the gapped MI phase starts to melt and the SF phase reappears in the system. Eventually, the system enters into another gapped phase after a critical value of  $\lambda \sim 131.10$  where in layer-A two bosons are localized in the deep lattice sites. We call this phase as the  $MI_3^r$  phase as depicted in the phase diagram of Fig. 3.2.

At this stage, further increase in the value of  $\mu$  will facilitate addition of bosons in layer-B which saturates at unit filling due to the hardcore nature of bosons where

all the sites are occupied by one boson each. This situation corresponds to the  $MI_4$  phases in the phase diagram where the total density of the system is  $\rho = 1$ . When  $\lambda$  is small, we have every sites in both the layers occupied by one atom each and this phase is called the  $MI_4^l$ . When  $\lambda$  increases, the  $MI_4^l$  phase melts and the system enters into the SF phase and eventually leading to the  $MI_4^r$  phase where the atoms in layer-A occupy the deep sites while the layer-B maintains the uniform density due to the hardcore nature. In such a situation the layer-A is like the striped phase and layer-B is saturated. These features can be clearly seen from the individual layer densities as shown in Fig. 3.3.

Similar situation arises for the other integer and non-integer densities where two distinct gapped phases appear at two limits of the superlattice potential which are separated by the SF phase as depicted in the phase diagram of Fig. 3.2. The corresponding boson distributions are shown in Table.I for clarity. For quarter-integer densities, the gapped islands appear for a range of intermediate values of  $\lambda$  separated by the SF phase. It is to be noted that the tip of the right lobes shift towards larger values of  $\lambda$  as  $\rho$  increases. However, there occurs an interesting pattern for the left lobes where the tips first shifts towards larger  $\lambda$  up to  $MI_4^l$  and then shift left for higher densities. The appearance of this feature is attributed to the presence of bosons in layer-B in all the lattice sites after a critical density  $\rho \geq 1$ . At these densities, the bosons in layer-A does not get affected by the presence of the bosons in layer-B as it experiences uniform repulsion which is equal to  $U_{AB}$  from all sites. Therefore, the physics of the system is governed only by the properties of bosons in layer-A as discussed in Ref. [73]. The  $MI^l$ -SF transitions happens for smaller and smaller values of  $\lambda$  as the density increases because the increase in density leads to the decrease in the effective onsite interactions on the shallow lattice sites. Therefore, the  $MI^l$  lobes melt into the SF phases due to the hopping  $t$  which dominates over the interactions. On the other hand the SF- $MI^r$  transition points shift towards the larger values of  $\lambda$  at higher densities because of the increase in number of particles in the deep wells which results in an increase in  $U_{AB}$ . Therefore, a stronger  $\lambda$  is necessary to introduce the  $MI^r$  phases as can be seen from the phase diagram.

To further understand the role of various interactions in our model, we study the phase diagram in  $\mu/t$  vs.  $U/t$  plane as well. For this purpose we consider a cut across the phase diagram of Fig.3.2 at  $\lambda = 60$  which corresponds to  $U = 80$  and  $U_{AB} = 40$ . In this case we vary  $t$  to obtain a range of  $U/t$  ratios and the resulting phase diagram in this case is shown in Fig.3.4. We obtain a very interesting pattern of staggered

MI lobes in this case. It can also be seen that the size of the MI lobes with odd integers in the subscript is larger as compared to the MI lobes with even integers in the subscript. We follow the nomenclature of density distributions given in Table-3.1 and discuss the phase diagram in the following text. As we increase  $\mu$  (bottom to top) the particle number increases and there are two possibilities for each newly added particle: (i) it is added on top of a density distribution wherein the particle arrangement is identical in both the layers, that is, vacuum state,  $MI_2^r$ ,  $MI_4^l$ ,  $MI_6^l$ , and  $MI_8^l$ , or (ii) the particle is added on top of an uneven density configuration, that is,  $MI_1$ ,  $MI_3^l$ ,  $MI_5$ , and  $MI_7$ . In case (i), the particle always ends up in the deeper potential well with a fewer number of particles. Such a rearrangement is expected, as the value of superlattice potential  $\lambda$  is sufficiently large. In case (ii), the particle entering the system avoids the densely occupied sites and prefers a site with lower occupancy. In this manner the contribution from  $U$  and  $U_{AB}$  terms is minimized and the system tends to attain a more uniform density distribution. The lobes with an even density distribution are less stable compared to the lobes with uneven density distribution and readily accept a new particle. Consequently, lobes of the former type are smaller in size with respect to the later.

### 3.3.2 Three-body constraint for bosons in layer-B

Now we discuss the case in which we replace the bosons in layer-B with the TBCs. As discussed before, the effect of three-body constraint is a result of large three-body onsite repulsion i.e.  $W \rightarrow \infty$ . In such a situation the maximum number of bosons allowed per lattice site is two i.e.  $(a^\dagger)^3 = 0$ . Such constrained bosons may impart significant effects on the overall phase diagram of bosons in optical superlattice. Note that, in this case we have finite values of two-body interaction  $U_B$  in layer-B. similar to the previous section, we numerically solve the mean-field Hamiltonian given in Eq. (5.3) and with  $U_A = U_B = 80$  and  $U_{AB} = 40$  and varying  $\lambda$  we obtain various gapped phases. The ground state phase diagram is shown in Fig. 3.5 and the particle distributions are shown in Table-II.

It can be seen that the phase diagram for this case exhibits distinct features along with some similarities compared to the one obtained when bosons in layer-B was hardcore in nature(compare with Fig. 3.2). Although the appearance of the MI phases for the odd (total)densities show similar behavior as the previous case, the even lobes exhibit different features with respect to their tip positions. It can be easily seen that the features in the part of the phase diagram from  $n = 6$  onwards

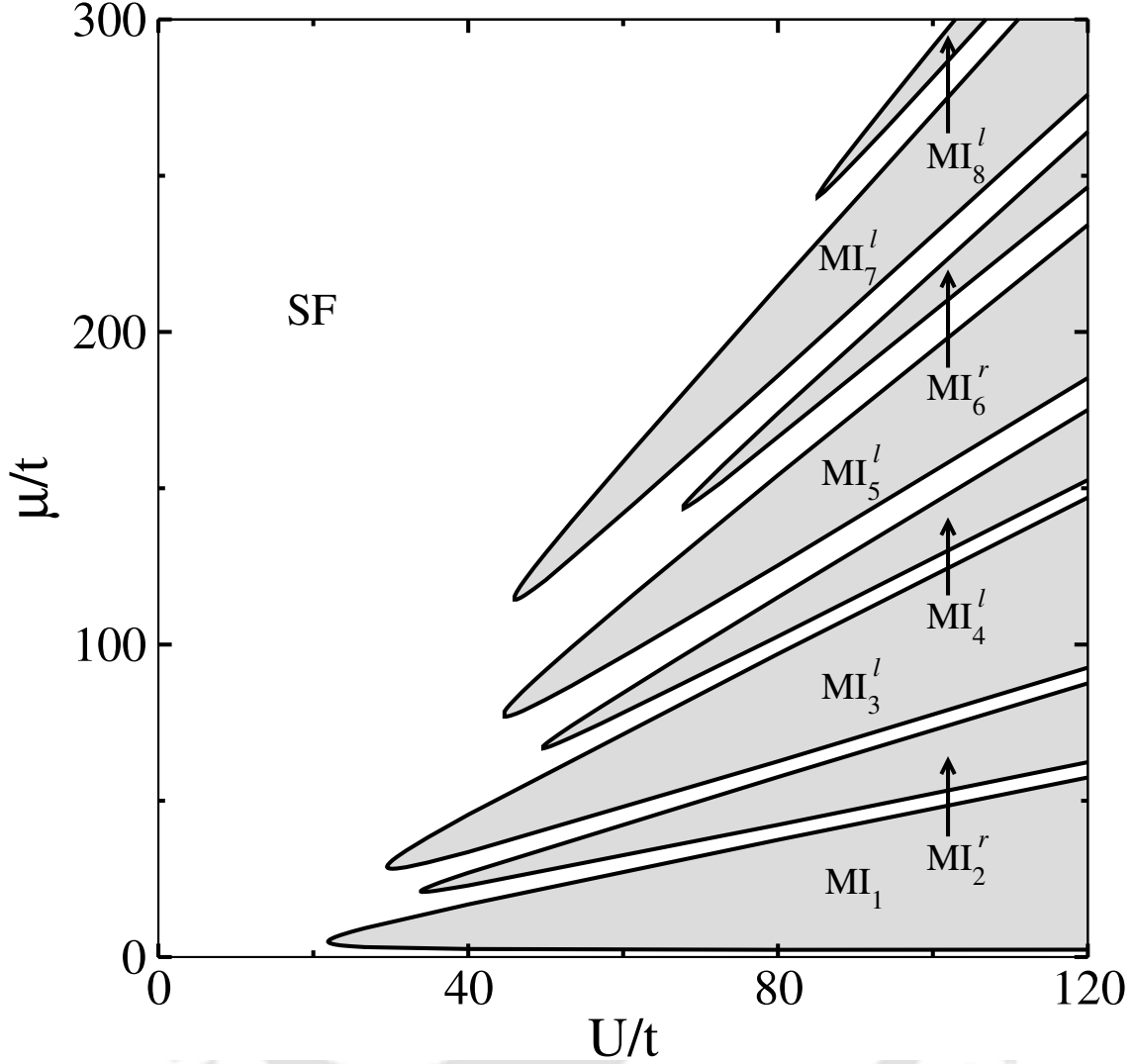


**Figure 3.6:** CMFT phase diagram in the  $\mu/t$  vs.  $U/t$  plane when bosons in layer-A are softcore and in layer-B are three-body constrained. Here  $U_A = U_B = U = 80, U_{AB} = 40$  and  $\lambda = 60$ . Since  $U_A$  is fixed in the case, we vary  $t$  in order to tune the ratio  $U/t$ .

matches well with the phase diagram of the previous case (when the layer-B was hardcore) except the first lobe at  $n = 1$  of Fig. 3.2. This can be understood as follows. Let's consider the  $\lambda = 0$  case for simplicity. As the layer-B is occupied by TBCs now, for  $n = 6$  the density of the supercell is 1.5. This means, there are two extra particles on top of the  $\rho = 1$  lobe ( $MI_4^l$ ). At  $\rho = 1$ , each sites of both the layers are occupied by one particle because of large onsite interactions  $U_A$  and  $U_B$ . Therefore, any extra particle which gets added to layer-B containing the TBCs will behave like hardcore bosons on top of the uniform particle distribution. Hence, the effective system becomes equivalent to the one considered in the previous section. However, there exists different gapped phases at low density regimes i.e. up to

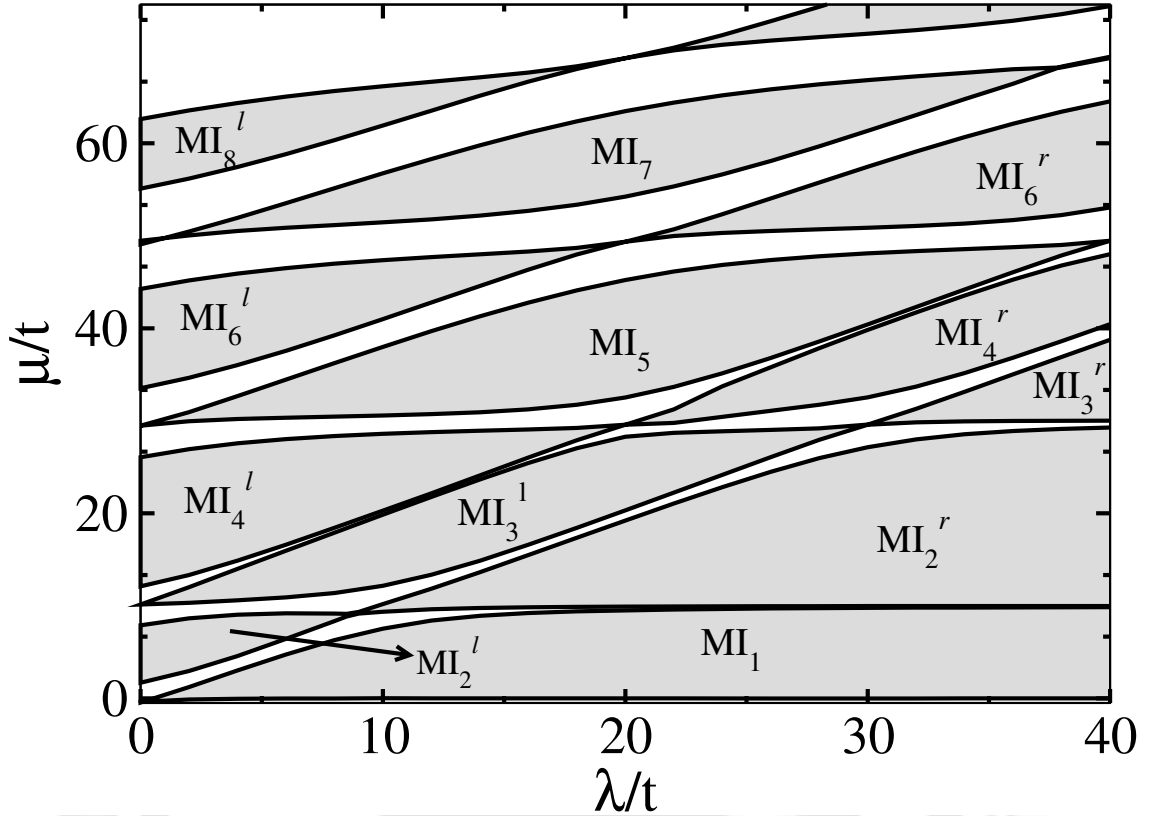


**Figure 3.7:** DMRG phase diagram when bosons in leg-A are softcore in nature and bosons in leg-B are HCBs.

$n = 6$  lobes. For  $n = 1$  ( $\rho = 0.25$ ) we get the  $MI_1$  phase which is similar to the one in Fig.3.2 which starts after finite value of  $\lambda \sim 8$ . As the number of particles increases, the second gapped phase  $MI_2^l$  appears at  $n = 2$  ( $\rho = 0.5$ ) for  $\lambda = 0$  and this survives up to a critical value of  $\lambda \sim 32$  and after this the system becomes gapless. In this case, each layer is occupied by one boson. Further increase in  $\lambda$  leads to the  $MI_2^r$  phase, where the particles live in the deep sites. Similarly, the  $MI_4$  phases appear for  $n = 4$  ( $\rho = 1$ ) in the beginning when  $\lambda = 0$  and the system is a proper Mott insulator at unit filling. Increase in  $\lambda$  will melt the gap and the SF phase appears and further increase in  $\lambda$  will re-introduce the gap and the system gets into the  $MI_4^r$  phase. In this phase, there can be two possible particle distributions in the lattice where two particles populate the deep sites of layer-A while sites of layer-B are uniformly filled by one particle in each site and vice-versa. This gapped phase vanishes at  $\lambda \sim 148$  and further increase in  $\lambda$  may lead to another gapped phase where the deep sites of both the layers will be occupied by two particles (not in the range of  $\lambda$  considered here). The physics of odd integer lobes can also be understood from the similar analogies discussed above.

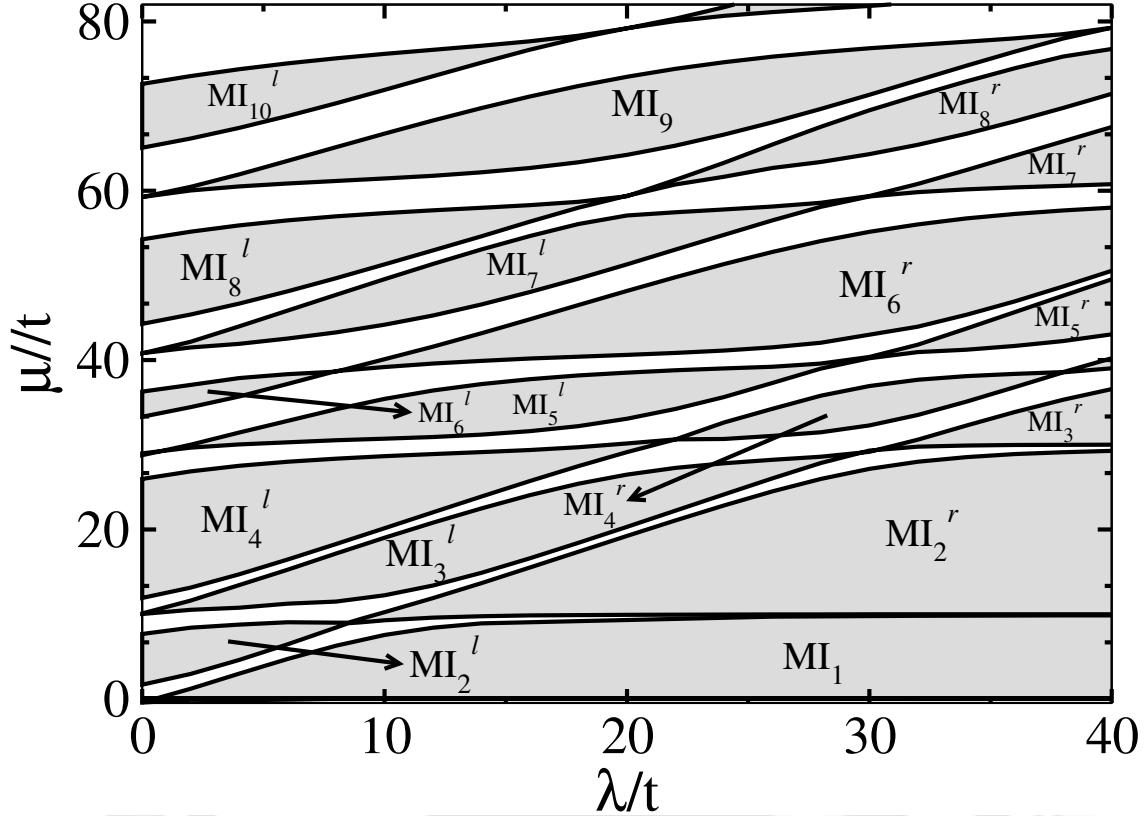


**Figure 3.8:** DMRG phase diagram when bosons in leg-A are softcore in nature and bosons in leg-B are TBCs.

Like before, in this case also we study the phase diagram in  $\mu/t$  vs.  $U/t$  plane. The various parameter values are fixed as follows,  $U_A = U_B = 80, U_{AB} = 40$  and  $\lambda = 60$ . The phase diagram obtained in this case is shown in Fig.3.6 and it can be readily seen that it has features similar to those obtained previously, Fig.3.4. Our discussion for the previous case holds mostly true in this case as well. However, there are two major differences between the two phase diagrams: (i) in the present case SF-MI transition critical points are in general higher than those found in the previous case. A straight forward explanation is, that because of increased density fluctuations SF region gets enlarged and MI phases sets in relatively later. This can be seen by comparing the position of the tips of the  $MI_1$  lobes in Fig.3.4 and Fig.3.6 (and other lobes as well), and (ii) by introducing three-body constrained bosons in the present case, we allow more number of particles to accommodate in layer B and make room for more degenerate states to set in. This can be seen in Table-3.2, in the density configurations for  $n = 3, 6$ , and so on. This degeneracy has a significant effect on the phase diagram, as it tends to make the corresponding MI states less stable. If vice-versa is true then we have stable MI phases, hence larger lobes.

**Table 3.2:** Table depicting various MI states when atoms in layer-B are TBCs. Each state shows the density distribution in the supercell corresponding to a particular MI state for a given  $n$  and  $\rho$ .

Boson distribution in the unit cell		
n	$\rho$	Supercell Configuration
1	0.25	$MI_1 = \begin{vmatrix} 0 & 1 \\ 0 & 0 \end{vmatrix} \rangle$ or $MI_1 = \begin{vmatrix} 0 & 0 \\ 0 & 1 \end{vmatrix} \rangle$
2	0.5	$MI_2^1 = \begin{vmatrix} 0 & 1 \\ 1 & 0 \end{vmatrix} \rangle$ or $MI_2^2 = \begin{vmatrix} 1 & 0 \\ 0 & 1 \end{vmatrix} \rangle$ and $MI_2^3 = \begin{vmatrix} 0 & 1 \\ 0 & 1 \end{vmatrix} \rangle$
3	0.75	$MI_3^1 = \begin{vmatrix} 1 & 1 \\ 0 & 1 \end{vmatrix} \rangle$ or $MI_3^2 = \begin{vmatrix} 0 & 1 \\ 1 & 1 \end{vmatrix} \rangle$ and $MI_3^3 = \begin{vmatrix} 0 & 2 \\ 0 & 1 \end{vmatrix} \rangle$ or $MI_3^4 = \begin{vmatrix} 0 & 1 \\ 0 & 2 \end{vmatrix} \rangle$
4	1.0	$MI_4^1 = \begin{vmatrix} 1 & 1 \\ 1 & 1 \end{vmatrix} \rangle$ and $MI_4^2 = \begin{vmatrix} 1 & 1 \\ 0 & 2 \end{vmatrix} \rangle$ or $MI_4^3 = \begin{vmatrix} 0 & 2 \\ 1 & 1 \end{vmatrix} \rangle$
5	1.25	$MI_5^1 = \begin{vmatrix} 1 & 2 \\ 1 & 1 \end{vmatrix} \rangle$ and $MI_5^2 = \begin{vmatrix} 1 & 2 \\ 0 & 2 \end{vmatrix} \rangle$
6	1.5	$MI_6^1 = \begin{vmatrix} 2 & 1 \\ 2 & 1 \end{vmatrix} \rangle$ or $MI_6^2 = \begin{vmatrix} 1 & 2 \\ 1 & 2 \end{vmatrix} \rangle$ $MI_6^3 = \begin{vmatrix} 2 & 1 \\ 1 & 2 \end{vmatrix} \rangle$ or $MI_6^4 = \begin{vmatrix} 1 & 2 \\ 2 & 1 \end{vmatrix} \rangle$ and $MI_6^5 = \begin{vmatrix} 1 & 2 \\ 1 & 2 \end{vmatrix} \rangle$
7	1.75	$MI_7^1 = \begin{vmatrix} 2 & 2 \\ 1 & 2 \end{vmatrix} \rangle$ and $MI_7^2 = \begin{vmatrix} 1 & 3 \\ 1 & 2 \end{vmatrix} \rangle$
8	2.0	$MI_8^1 = \begin{vmatrix} 2 & 2 \\ 2 & 2 \end{vmatrix} \rangle$ and $MI_8^2 = \begin{vmatrix} 1 & 3 \\ 2 & 2 \end{vmatrix} \rangle$
9	2.25	$MI_9 = \begin{vmatrix} 2 & 3 \\ 2 & 2 \end{vmatrix} \rangle$
10	2.5	$MI_{10}^1 = \begin{vmatrix} 3 & 3 \\ 2 & 2 \end{vmatrix} \rangle$ and $MI_{10}^2 = \begin{vmatrix} 2 & 4 \\ 2 & 2 \end{vmatrix} \rangle$

### 3.3.3 Phase diagram in one dimension

In this section we complement our CMFT results presented above by analyzing the situation in one dimension. The one dimensional analogue of bilayer geometry is a two-leg ladder where the layer-A(B) is replaced by leg-A(B) as shown in Fig. 3.1(c). The one dimensional ladder geometries are extremely important in the context of condensed matter systems as it resembles to several structures of compounds of interest. The ladder geometries has been discussed in great detail in terms of Hubbard model [127–139] and Bose-Hubbard model [57, 86, 140–143]. Analogous to the 2d case we assume only inter-leg dipole-dipole interactions by aligning the dipoles at magic angle with each other along the leg direction. The physics of this system will be similar to the two dimensional case due to the construction of the bilayer

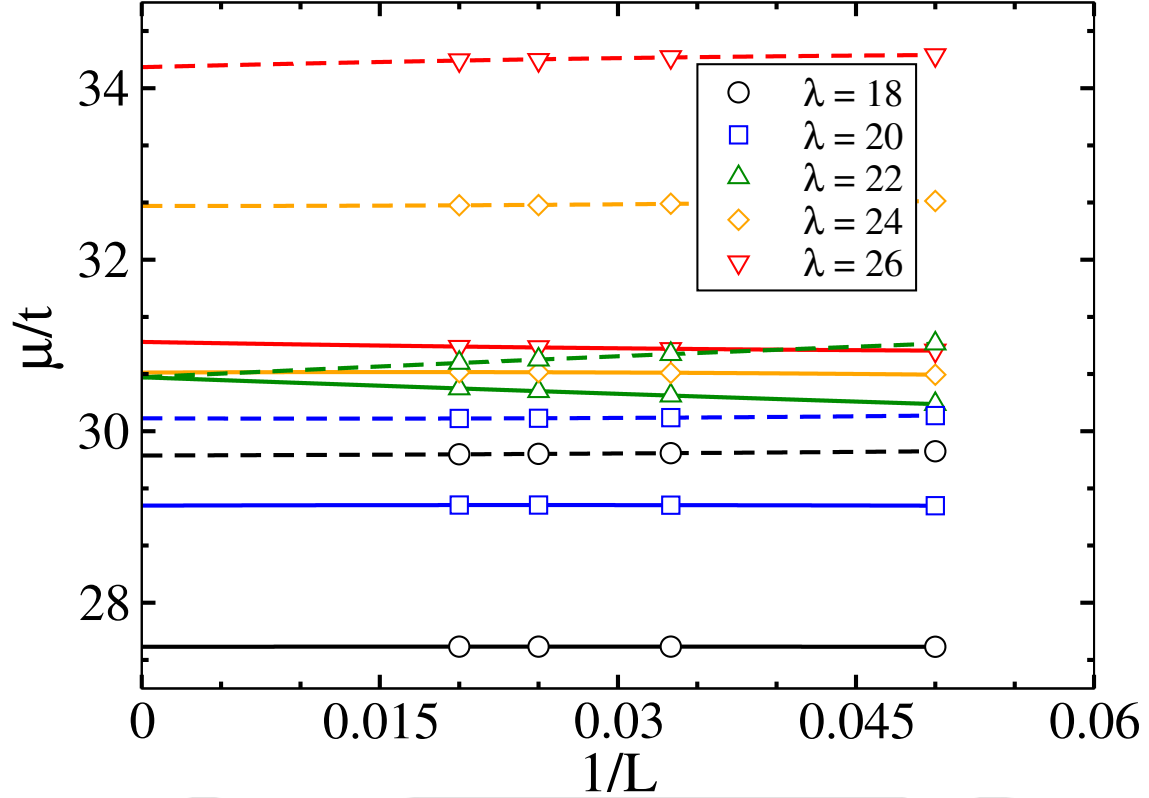


**Figure 3.9:** Finite size scaling of chemical potentials for  $\rho = 1.5$  for different values of  $\lambda$  corresponding to the phase diagram of Fig. 3.7 when bosons in leg-A are softcore in nature and bosons in leg-B are HCBs. The solid and dashed lines represent the fitted functions to  $\mu^+$  and  $\mu^-$  respectively.

lattice in our case as discussed earlier. We employ the DMRG method to solve the model(Eq. (3.1)) in the canonical ensemble to compute the ground state energy and wave function. To separate the gapped and gapless regions we calculate the single particle gap which is defined as

$$G_L = \mu^+ - \mu^-, \quad (3.4)$$

with  $\mu^+ = E_L(N + 1) - E_L(N)$  and  $\mu^- = E_L(N) - E_L(N - 1)$  are the chemical potentials and  $E_L(N)$  is the the ground state energy of a system of length  $L$  and  $N = N_A + N_B$  is the total number of particles in the system . We obtain the ground state phase diagram for both the cases with bosons of leg-B separately being HCBs and TBCs while bosons in leg-A are softcore in nature which are shown in Fig. 3.7( $U_A = 20$  and  $U_{AB} = 10$ ) and Fig. 3.8( $U_{A,B} = 20$  and  $U_{AB} = 10$ ) respectively. One can easily see that the phase diagrams of Fig. 3.7 and Fig. 3.8 qualitatively match fairly well with the ones obtained using the CMFT method i.e. Fig. 3.2

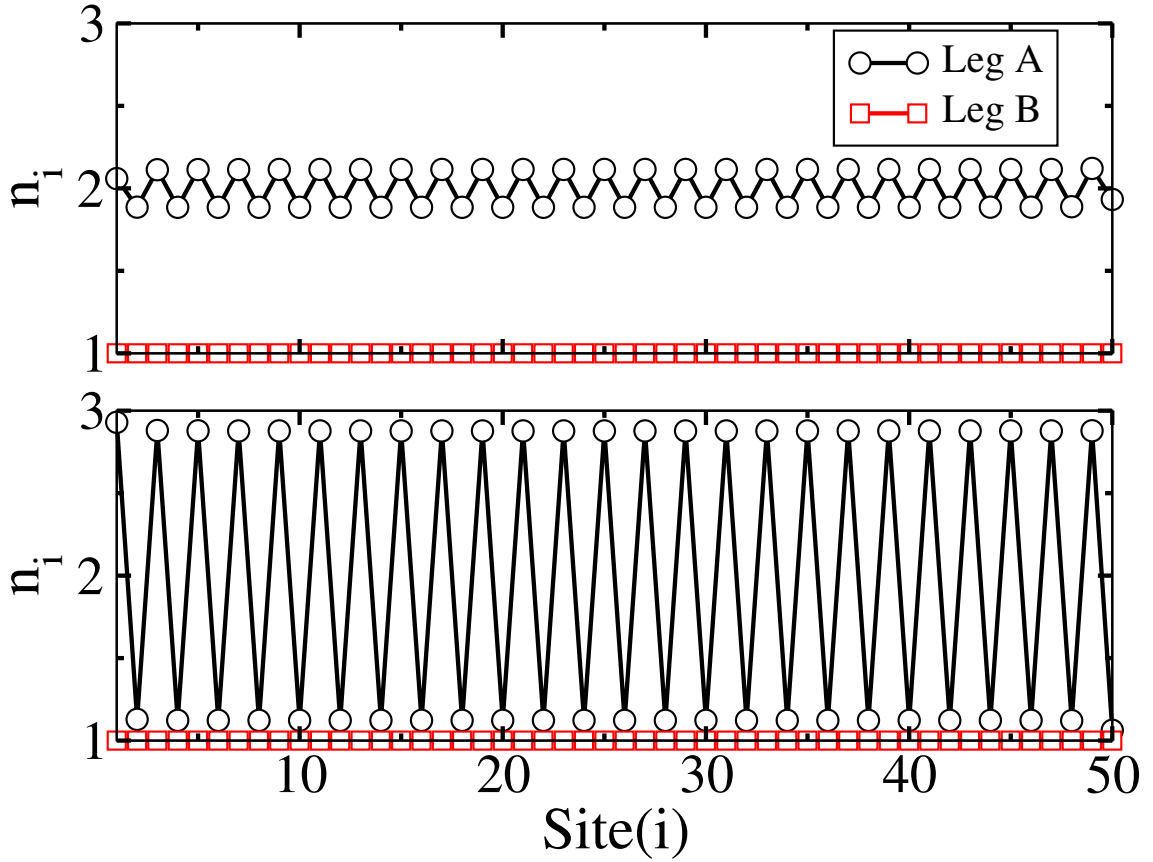


**Figure 3.10:** Density distribution of the system when  $\lambda = 12$ (top) and  $\lambda = 28$ (bottom) for  $\rho = 1.5$  corresponding to the phase diagram of Fig. 3.7. The black circles and red squares represent the density distribution of leg-A and leg-B respectively.

and Fig. 3.5 respectively. When bosons in leg-B are HCBs, we observe the MI tip positions first increase and then decrease as shown in Fig. 3.7 while there is an alternating increase and decrease of the tip positions when the bosons in leg-B are TBCs as plotted in Fig. 3.8. The boundaries of the MI lobes are computed by extrapolating the  $\mu$  values across the MI plateaus to thermodynamic limit by quadratic fitting. In Fig. 3.9, we show the finite size extrapolation of  $\mu^+$ (dashed) and  $\mu^-$ (solid) for  $\lambda = 18, 20, 22, 24$  and  $26$ . This clearly shows that  $G_{L \rightarrow \infty}$  remains finite in the gapped phase and vanishes in the gapless region which clearly distinguishes between the gapped and gapless phases in the phase diagrams.

Further, to understand the particle distribution in real space we compute the expectation value of the number operator as

$$\langle n_i \rangle = \langle \Psi_0 | n_i | \Psi_0 \rangle \quad (3.5)$$

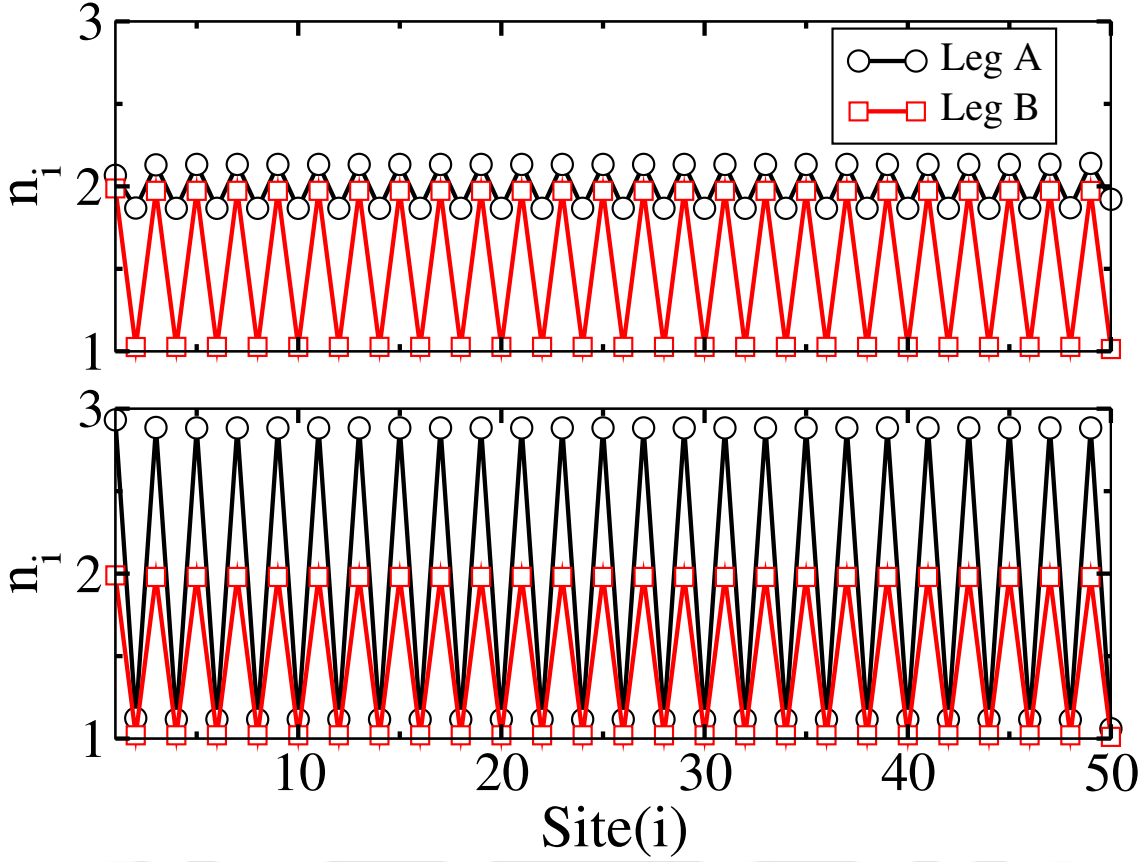


**Figure 3.11:** Density distribution of the system when  $\lambda = 22$ (top) and  $\lambda = 38$ (bottom) for  $\rho = 1.75$  corresponding to the phase diagram of Fig. 3.8. The black circles and red squares represent the density distribution of leg-A and leg-B respectively.

where  $|\Psi_0\rangle$  is the ground state wave function of the system. As an example, in Fig. 3.10 we plot  $\langle n_i \rangle$  w.r.t. site index  $i$  for  $\lambda = 12$ (top) and  $\lambda = 28$ (bottom) corresponding to the  $MI_6^l$  and  $MI_6^r$  phases respectively of the phase diagram shown in Fig. 3.7. It can be clearly seen that for  $\lambda = 12$  the leg-B is occupied by one hardcore boson in each site whereas in leg-A, each site is occupied by two atoms. However, for  $\lambda = 28$ , the leg-B is unaffected and leg-A shows  $|\dots 3 1 3 1 \dots\rangle$  type of distribution corresponding to the  $MI_6^r$  phase. A similar  $\langle n_i \rangle$  vs  $i$  plot is shown in Fig. 3.11 for the  $MI_7$  phase of Fig. 3.8. Here we consider  $\lambda = 22$ (top) and  $38$ (bottom) which fall in two regions of the  $MI_7^l$  and  $MI_7^r$  phases respectively. For  $\lambda = 22$ , all the sites of leg-A are occupied by two particles each whereas leg-B exhibits a finite density oscillation corresponding to  $|\dots 2 1 2 1 \dots\rangle$  type of distribution. However, for large  $\lambda = 38$ , the density distribution of leg-A becomes  $|\dots 3 1 3 1 \dots\rangle$  while the leg-B remains unaffected. It is to be noted that for the parameters considered here, the gapless regions between two gapped phases are very small compared to

ones obtained using the CMFT method.

### 3.4 Conclusions

We analyse the ground state properties of a system of interacting bosons in bilayer superlattice with inter-layer repulsion which can be introduced by the dipole-dipole interactions. Considering the bosons in one layer as softcore in nature and separately allowing two and three-body hardcore constraints in the other layer we obtain the ground state phase diagram using the CMFT approach. The phase diagrams exhibit various gapped MI phases at integer and half-integer densities. Due to the competition between the superlattice potential, intra- and inter-layer interactions and the constraints on the bosons of layer-B leads to interesting features in the phase diagram. It is shown that within the range of  $\lambda$  considered, we obtain two types MI lobes ( $MI_n^l$  and  $MI_n^r$ ) separated by the SF region for a particular total number of particles in the supercell equal to  $n$ . Interestingly, when the hardcore constraint is applied in one layer, the tips of the  $MI_n^l$  lobes first shift towards higher values of  $\lambda$  and then gradually recede to the lower values of  $\lambda$ . At the same time the tips of the  $MI_n^r$  lobes shift towards the higher  $\lambda$  values with increase in density of the system. The situation is completely different when the three-body constraint is considered in one layer. The tips of MI lobes first oscillate and then after a critical density follows the trend similar to the one for the hardcore constraint. We further complement our findings by repeating the calculations in an one dimensional non-locally coupled ladder superlattice using the DMRG method and show that the quantum phase diagrams qualitatively agree with the CMFT method. The physics obtained in this work deals with the system of bosons in two-layer systems with different types of on-site interactions in a superlattice. The results provide detailed analysis of the effect of constrained bosons on the overall phase diagram of the bilayer system which is also equivalent to a two-component atomic system. With the experimental progress in controlling local and dipole-dipole interactions in recent years, these findings can be experimentally observed with the existing quantum gas setups.



## Chapter 4

# Constrained bosons in two-leg Bose-Hubbard ladder

### 4.1 Introduction

In the previous chapter we studied the phase transition in a system of non-locally coupled lattice. This refers to two different lattices such as bilayer system of two-leg ladder systems where the individual layer or legs are not coupled through any tunneling. The addition of coupling between the two subsystems results in interesting physics which has been explored in great detail in the context of optical lattices.

In the last few decades, the low-dimensional bosonic systems are a topic of paramount interest of research. In particular, the one-dimensional (1D) or quasi-1D systems are a subject of great importance for the realization of novel quantum phases [133, 144]. For a simple model like BH ladder [140, 141, 143], the extra coupling along the rung influences a remarkable change in the quantum phase transitions (QPTs). Also several intriguing quantum phases have been predicted for other ladder systems [114, 142, 145–151] in presence of the rung hoppings and other interactions. It has been shown that a system of hardcore bosons on a two leg ladder exhibits signature of rung-insulator phase at half filling due to the influence of inter-leg hopping [129]. Finite onsite interaction on both the legs (i.e. with softcore bosons) leads to a modified SF-MI phase transition critical point and it has been shown that for large inter-leg hopping the system exhibits the properties of a single BH chain [140, 141]. On the other hand recent studies on three-body constrained bosons on a two leg ladder with finite inter-leg interaction have revealed the dimer rung-insulator phase [147]. Recent study on two- and three-body constrained dipolar bosons in a pair of one-dimensional optical lattices coupled to each other by

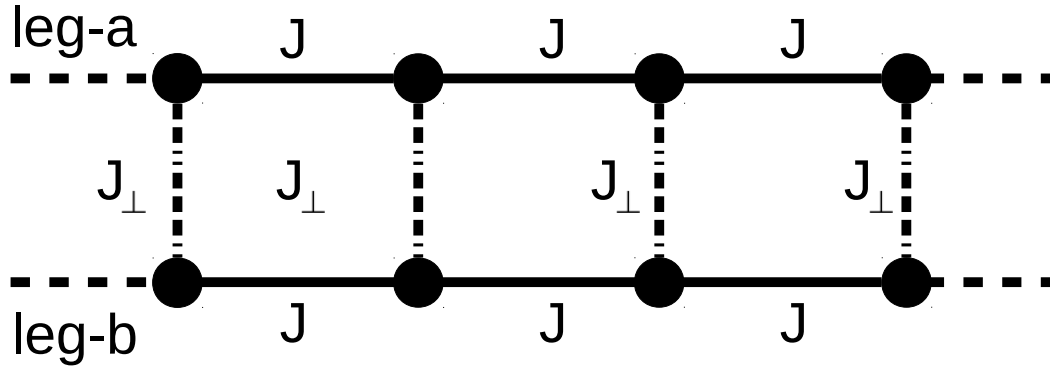


**Figure 4.1:** Schematic diagram of a BH ladder with intraleg and interleg hoppings.

nonlocal dipole-dipole interactions has predicted the existence of trimer and dimer superfluids in presence of attractive onsite interactions [87].

In this chapter we consider a two-leg Bose-Hubbard ladder as depicted in Fig. 4.1 and impose hardcore constraint in one leg and three-body constraint in the other leg. By allowing attractive onsite interactions for the three-body constrained bosons, we study the effect of rung-hopping on the system.

## 4.2 Model and approach

The system under consideration is represented by the schematic diagram as shown in Fig. 4.1 and can be described by a modified Bose-Hubbard (BH) model as

$$\begin{aligned}
 \mathcal{H}_{BH} = & -J \sum_{\langle i,j \rangle, \alpha} (a_{i\alpha}^\dagger a_{j\alpha} + H.c.) - J_\perp \sum_i (a_{ia}^\dagger a_{ib} + H.c.) \\
 & + \sum_{i,\alpha} \frac{U_\alpha}{2} n_{i\alpha} (n_{i\alpha} - 1) - \sum_{i,\alpha} \mu_\alpha n_{i\alpha}.
 \end{aligned} \tag{4.1}$$

Here  $a_{i\alpha}^\dagger$  ( $a_{i\alpha}$ ) is the bosonic creation (annihilation) operator at the  $i^{th}$  site of the  $\alpha^{th}$  leg, where  $\alpha$  ( $= a, b$ ) represents the leg index of the ladder.  $U_\alpha$  represents the local two-body intra-leg onsite interactions and  $\mu_\alpha$  is the leg-dependent chemical potential.  $J$  and  $J_\perp$  are the hopping rate of bosons along the legs and rungs of the ladder respectively.  $n_{i\alpha}$  is the number operator corresponding to the  $i^{th}$  site and  $\alpha^{th}$  leg. First we consider three-body constrained bosons (TBCs) in leg-a and hardcore bosons (HCBs) in leg-b. The two- and three-body constraints in the legs

are achieved by considering  $(a^\dagger)^2 = 0$  and  $(a^\dagger)^3 = 0$  respectively. It is to be noted that for the HCBs in leg-b,  $U_{\alpha=b} \rightarrow \infty$  and due to the hardcore constraint the terms associated to  $U_{\alpha=b}$  vanish in Eq. (4.1). The TBC is achieved by considering the three-body onsite interaction  $W \rightarrow \infty$  in leg-a.

For the exploration of quantum phases we employ both the CMFT and the DMRG methods (Chapter 2) and obtain the ground state properties of this model.

Using the CMFT approach discussed in Chapter 2 we can write

$$H = H_C + H_{MF}, \quad (4.2)$$

where,  $H_C$  ( $H_{MF}$ ) is the cluster (mean-field) part of the Hamiltonian.  $H_C$  is same as Eq. 4.1 limited to the cluster size.

Introducing the leg-dependent SF order parameter and the superfluid density given by

$$\psi_{i\alpha} = \langle a_{i\alpha}^\dagger \rangle = \langle a_{i\alpha} \rangle \quad (4.3)$$

and

$$\rho_s = \frac{1}{4} \sum_{i=1}^2 \sum_{\alpha \in [a,b]} |\psi_{i\alpha}|^2 \quad (4.4)$$

respectively, we write  $H_{MF}$  as

$$H_{MF} = -J \sum_{\alpha, \langle i,j \rangle} [(a_{i\alpha}^\dagger + a_{i\alpha})\psi_{j\alpha} - \psi_{i\alpha}^* \psi_{j\alpha}]. \quad (4.5)$$

The DMRG simulations are performed in canonical ensemble with a fixed boson number and hence the Hamiltonian in Eq. 4.1 is explicitly independent of  $\mu$ . We apply the MPS based DMRG algorithm using an open boundary condition on a system of length up to  $L = 240$  and bond dimensions up to 400.

Our studies are focused on attractive onsite interaction for the TBCs. To ensure an attractive onsite interaction between the particles the results are obtained by considering  $U = -1$  which also sets the energy scale that makes all the physical parameters dimensionless. We also assume equal chemical potentials for bosons in both the legs by making  $\mu_a = \mu_b = \mu$  for the CMFT calculations.

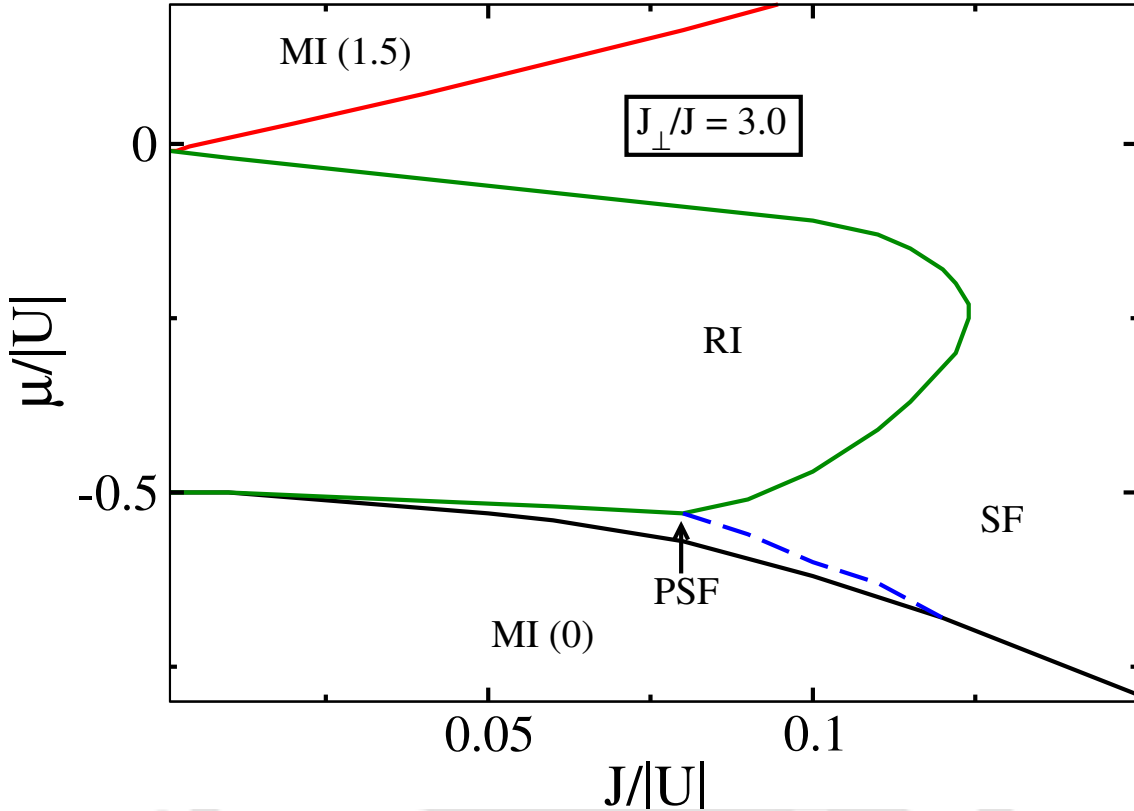


**Figure 4.2:** Phase diagram for HCB-TBC system in  $\mu/|U| - J/|U|$  plane using the CMFT method for  $J_{\perp}/J = 3.0$ .

## 4.3 Results

In this section we discuss the results in detail. First we will present the ground state properties of the HCBs+TBCs system and then we will highlight the case of TBCs+TBCs.

### 4.3.1 The HCB-TBC system

#### 4.3.1.1 CMFT results

The phase diagram obtained using the CMFT approach and by assuming  $J_{\perp}/J = 3$  is depicted in Fig. 4.2. The phase diagram exhibits a gapped lobe at  $\rho = 1$  separated from the gapless regions by the green curve. The gapped and gapless regions are extracted by comparing the behaviour of  $\rho$  and  $\rho_s$  as a function of  $\mu/|U|$ . In Fig. 4.3(a) we plot  $\rho$  (red circles) and  $\rho_s$  (black squares) as a function of  $\mu/|U|$  for a cut through the phase diagram at  $J/|U| = 0.04$ . A finite plateau at  $\rho = 1$  associated with  $\rho_s = 0$  clearly indicates the gap in the system. By tracing out the

$\mu$  values from the end points of the plateaus for different values of  $J/|U|$  we obtain the boundary of the gapped lobe at  $\rho = 1$ . We find that for small  $J/|U|$ , the leg-a with TBCs gets populated first and approaches a maximum density  $\rho_a \sim 2$  (green diamonds in Fig. 4.3(a)) due to attractive onsite interactions. At the same time  $\rho_b$  (blue cross) remains vanishingly small as can be seen from Fig. 4.3(a). The situation is similar even before the plateau is reached. In this region,  $\rho_a$  increases in steps of two particles at a time and  $\rho_b$  remains zero. As a result, the total density of the system i.e.  $\rho$  also exhibits jumps in steps of two particles as a function of  $\mu/|U|$  which is a signature of the pair superfluid (PSF) phase [57]. For larger values of  $\mu/|U|$ , the density of leg-b starts to increase and the entire system exhibits a single particle SF phase which can be characterized by a finite value of  $\rho_s$  (see Fig. 4.3(a)). Further increase in  $\mu/|U|$  leads to saturation at  $\rho = 1.5$ . Note that the plateaus at  $\rho = 0$  and  $\rho = 1.5$  correspond to the empty and full states that are marked by black and red curves respectively in the phase diagram of Fig. 4.2.

To examine the nature of these gapped and gapless phases we define different correlation functions such as

$$\begin{aligned} C^{m,a} &= \langle (a_{ia}^\dagger)^n (a_{ja})^n \rangle \\ C^{m,b} &= \langle (a_{ib}^\dagger)^n (a_{jb})^n \rangle \\ C^{m,\perp} &= \langle (a_{ia}^\dagger)^n (a_{ib})^n \rangle \end{aligned} \quad (4.6)$$

Here  $n = 1$  (2) represents the single (pair) correlations and the superscripts  $a$ ,  $b$  and  $\perp$  represent correlations along leg-a, leg-b and the rung of the ladder, respectively. Note that due to finite size of the cluster considered here (i.e. four sites) the correlation functions are computed with only two sites. In Fig. 4.3(b) and (c) we plot the single and pair correlation functions as a function of  $\mu/|U|$  and for  $J/|U| = 0.04$ . It can be seen from Fig. 4.3(b) that when the system is gapped (plateau region in Fig. 4.3(a)), the value of  $C^{1,\perp}$  (blue triangles) is finite and large whereas  $C^{1,a}$  (red circles) and  $C^{1,b}$  (black squares) remain vanishingly small. These features indicate that the particle's motion along the legs are seized due to almost full and almost empty states of leg-a and leg-b respectively at very small  $J/|U|$ . However, there exists a finite rung correlation due to strong rung coupling  $J_\perp = 3$  - a signature that corresponds to the rung insulator (RI) phase. On the other hand all the single particle correlations remain finite in the SF phase although  $C^{1,a}$  is comparatively smaller than the other two (Fig. 4.3(b)). The reason behind this is the following. When in the SF phase, due to the TBC nature of the particles, the leg-a gets populated first

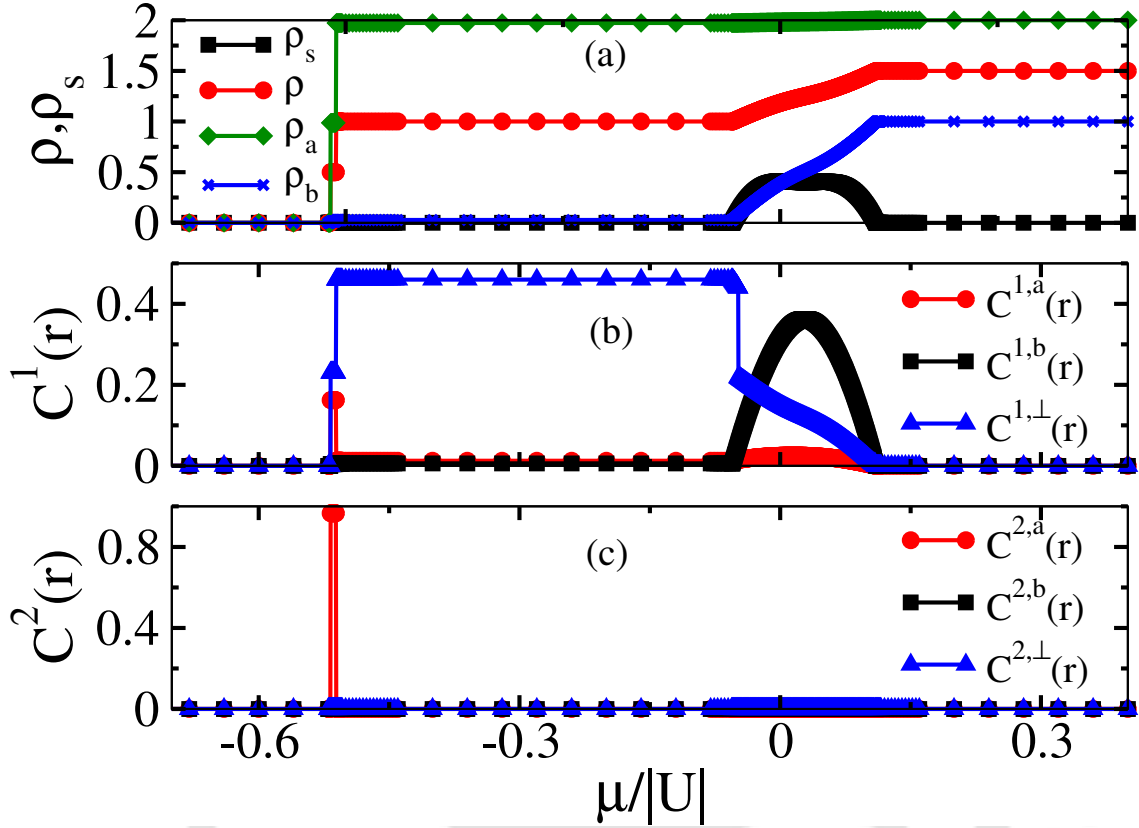


**Figure 4.3:** (a)  $\rho, \rho_s$  vs  $\mu$  plot, (b) and (c) are the single and pair correlations for bosons respectively along legwise and rungwise direction in a BH ladder using CMFT method for  $J/|U|=0.04$ .

leading to a larger value of  $\rho_a$  (green diamonds) as compared to  $\rho_b$  (blue crosses) as can be seen from Fig. 4.3(a). Hence, the particle's motion in leg-a is restricted leading to small values of  $C^{1,a}$ . However, when the system is in the PSF phase, the  $C^{1,b}$  vanishes whereas the other two correlations remain finite. This is because, due to the softcore nature of the TBCs, all the particles prefer to populate the leg-a in the regime of small  $\mu/|U|$ . Interestingly, all the two particle correlations such as  $C^{2,a}$ ,  $C^{2,b}$  and  $C^{2,\perp}$  vanish in the RI and SF phases. However, in the PSF phase the  $C^{2,a}$  remains finite in the regime  $-0.518 < \mu/|U| < -0.511$ . This indicates that due to attractive nature of  $U$ , the particles in leg-a form pairs in the limit of small  $\mu/|U|$  or small density.

Now we analyse the dependence of the RI phase on  $J_{\perp}/J$  ratio within the limitations of the CMFT approach. In Fig. 4.4 we plot the RI lobes at  $\rho = 1$  for different values of  $J_{\perp}/J$ . Interestingly, we see that the RI lobe expands and eventually for large value of  $J_{\perp}/J = 6$ , the gap remains open forever as a function of  $J/|U|$ . This indicates that the RI-SF transition ceases to occur after a certain  $J_{\perp}/J$  ratio. To

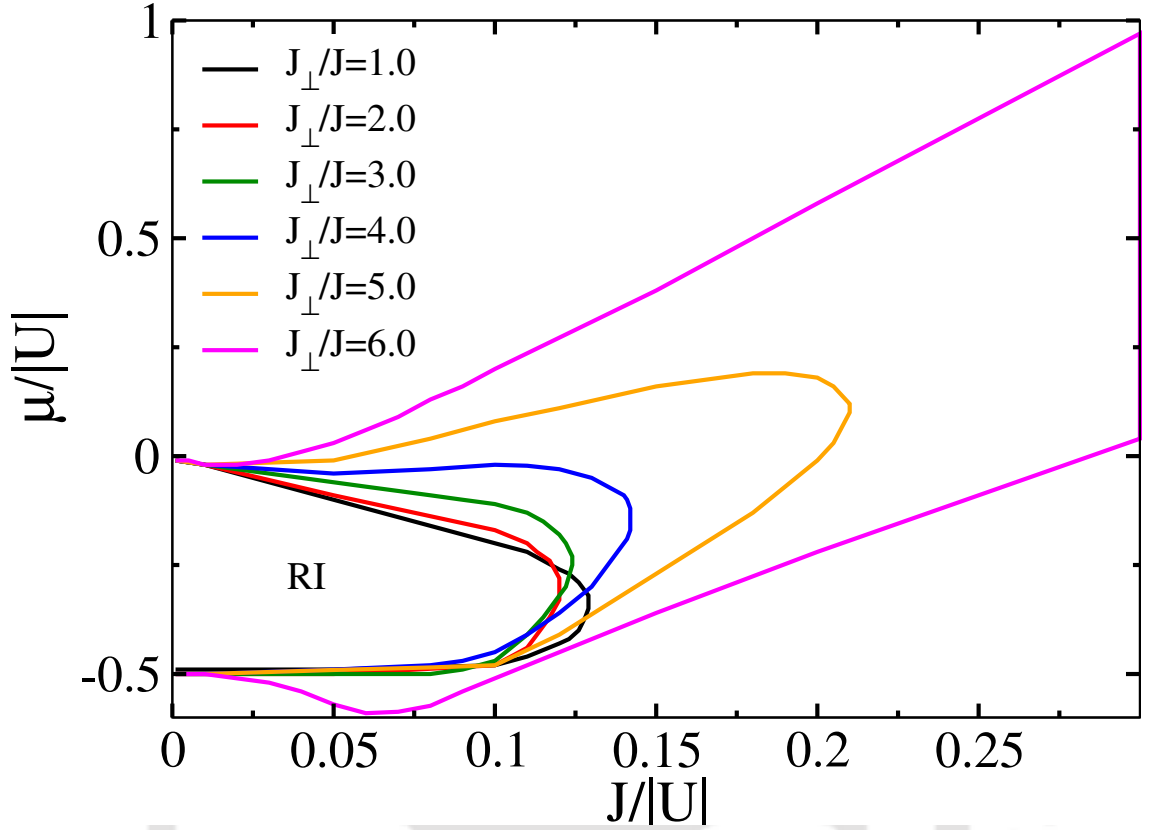


**Figure 4.4:** Phase diagram of HCB-TBC system in  $\mu/|U| - J/|U|$  plane for different  $J_{\perp}/J$  ratios.

further investigate these interesting features we utilize the DMRG approach in the following section.

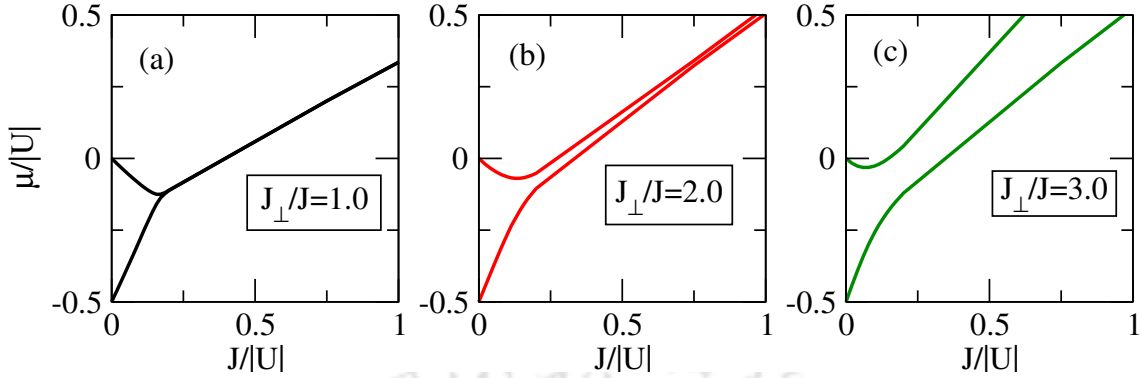
#### 4.3.1.2 DMRG results

In this subsection, we focus on the analysis based on the DMRG simulations of the model shown in Eq. 4.1 for HC-TBC system. The primary focus of our DMRG simulation is to examine the fate of these gapped phases that arise at  $\rho = 1$  in our CMFT analysis. To this end we first consider the case of  $J_{\perp}/J = 3$  and obtain the boundaries of the gapped phase as shown in Fig. 4.5 (c). The boundaries are obtained by using the different chemical potentials computed from the energies as

$$\mu^+ = E_{N+1} - E_N \text{ and } \mu^- = E_N - E_{N-1} \quad (4.7)$$

where  $E_N$  is the ground state energy of the system with  $N$  bosons. Contrary to the CMFT method, the gap i.e.

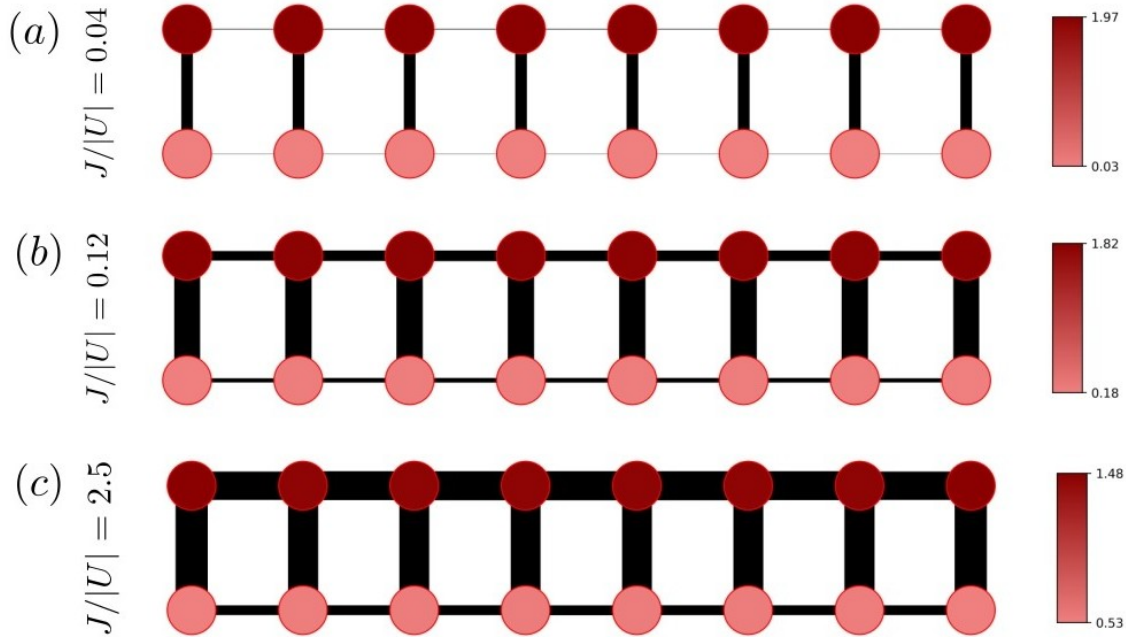
$$G = \mu^+ - \mu^- \quad (4.8)$$



**Figure 4.5:** DMRG phase diagrams for (a)  $J_{\perp}/J = 1.0$ , (b)  $J_{\perp}/J = 2.0$  and (c)  $J_{\perp}/J = 3.0$ . The phase boundaries represent the extrapolated values of  $\mu^+$  and  $\mu^-$  (see text) with  $L = 40, 80, 120$  and  $160$ .

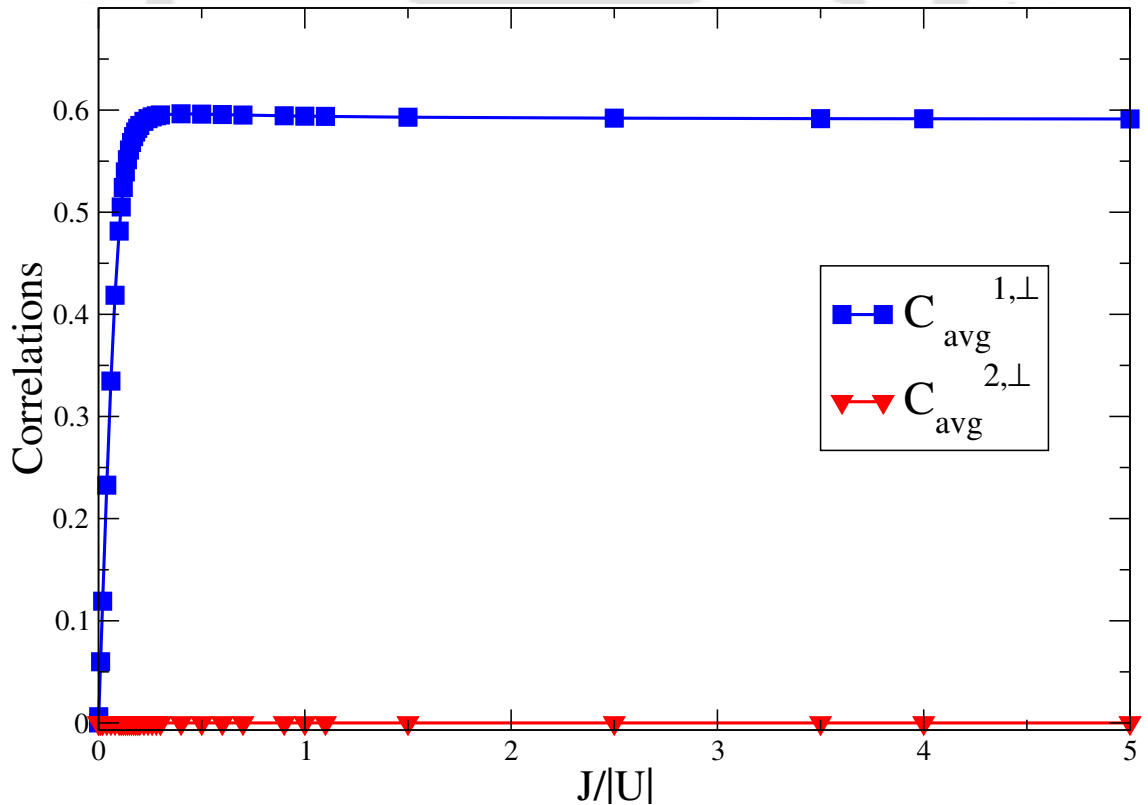
in this case does not close after a critical point, rather it remains finite throughout. However, the gap  $G$  shrinks up to a certain point with increase in  $J/|U|$  and expands again for stronger hopping strengths.

To understand the behaviour of the gapped phase at  $\rho = 1$  further we compute various correlation functions across the bonds along the legs as well as rungs as defined in Eq. 4.6. Figure 4.6 depicts the plot of onsite particle densities and bond



**Figure 4.6:** A TBCs+HCBs ladder consisting of  $L = 16$  sites showing the single-particle correlation along each bond (represented by its thickness) and density of particles corresponding to each lattice site (represented by the colorbar on the right) for  $J_{\perp}/J = 3$ .

correlations for different values of  $J/|U|$  and  $J_{\perp}/J = 3$ . The color bar denotes the onsite particle densities represented as circles and the thickness of the bonds indicate the values of correlation functions. It can be seen that when  $J/|U| = 0.04$  (Fig. 4.6(a)), the onsite particle densities are close to 2 (0) in leg-a (leg-b). At the same time the rung (leg) correlations become finite (zero). This is an indication of the RI phase as discussed in the previous section. These features can be understood from the limiting situation when  $J/|U| \rightarrow 0$ . In this limit all the bosons occupy leg-a and form tightly bound bosonic pairs which are effective hardcore bosons and we call them dimers. Moreover, as  $\rho = 1$ , the leg-a is fully occupied by a dimer at each site. In such a situation, due to strong rung hopping i.e.  $J_{\perp} = 3$ , addition of any extra particle costs extra energy which leads to a finite gap. However, as  $J/|U|$  starts to increase but small i.e.  $J/|U| = 0.04$ , the gap tends to decrease and rung correlation starts to become finite leading to a RI phase as depicted in Fig. 4.6(a). This continues for certain values of  $J/|U|$  where the gap becomes minimum. At these intermediate values of  $J/|U|$ , the correlations along the rung become more stronger although a finite correlations develop along the bonds on the legs as depicted in



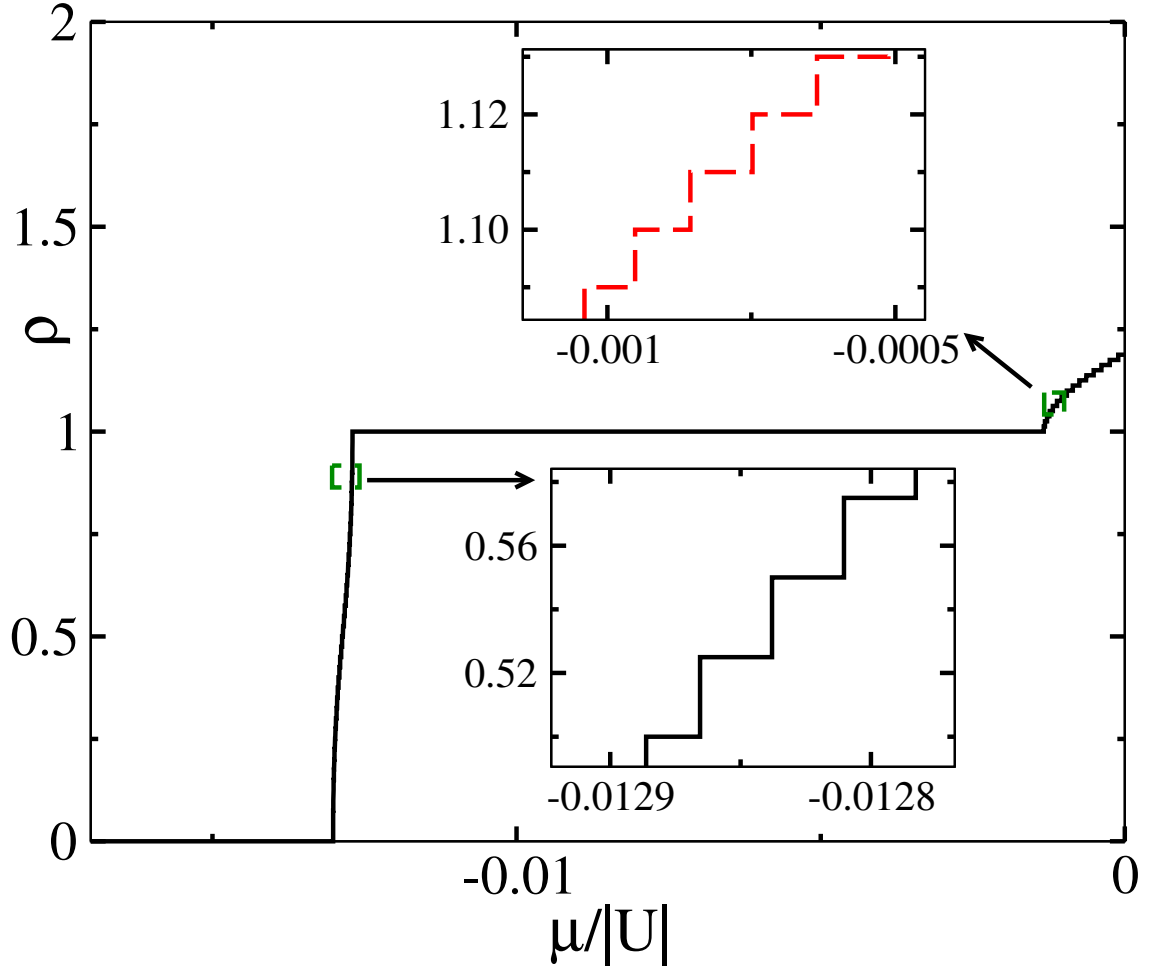
**Figure 4.7:** Single- and two-particle correlations averaged over all the rungs on a system of size  $L = 240$  for  $J_{\perp}/J = 3$ .

Fig. 4.6(b). Note that in this case the densities on both the legs are incommensurate. Further increase in  $J/|U|$  leads to opening of the gap. However, in this limit the hopping strengths dominate over the interaction and one gets finite correlation both along the legs and rungs as shown in Fig. 4.6(c) for  $J/|U| = 2.5$ .

The existence of finite a gap and finite correlations in the limit of small  $U$  are two contradicting characters. However, one can understand the origin of this gap by looking at the onsite densities which are  $n_a^i \sim 1.5$  and  $n_b^i \sim 0.5$  as shown in Fig. 4.6(c). These values indicate the densities of leg-a and leg-b as  $\rho_a = 1.5$  and  $\rho_b = 0.5$  respectively. At this density, the sites in leg-a, due to TBC will be occupied by one particle each and the rest of the particle will behave like hardcore bosons at half filling. As a result the entire system is now a two-leg ladder of hardcore bosons at half filling which exhibits a RI phase for finite values of rung hopping [129]. The RI phase in this case is found to possess finite rung as well as leg correlations which can be seen from Fig. 4.6(c). From our analysis we obtain that although the entire gapped phase exhibits signatures of the RI phase which is characterised by the single particle rung correlations. This can be clearly seen from Fig. 4.7 where we plot the average values of single and two particle rung correlations as  $C_{avg}^{1,\perp}$  (blue squares) and  $C_{avg}^{1,\perp}$  (red triangles) as a function of  $J/|U|$ . Note that as discussed already, the RI phase originates from two different scenarios in the small and large  $J/|U|$  limits. Based on this we denote them as RI<sub>1</sub> and RI<sub>2</sub> in the small and large  $J/|U|$  limits respectively. The possible transition or crossover between these two phases will require further analysis.

We also analyse the gapped phases for other values of  $J_{\perp}/J$  ratios as shown in Fig. 4.5. We obtain that when  $J_{\perp}/J = 1$  (Fig. 4.5(a)), a transition from a gapped phase to a gapless SF phase via a critical point is seen at  $J/|U| \sim 0.2$ . In this case the gap never opens up even for larger values of  $J/|U|$ . However, the situation becomes interesting when  $J_{\perp}/J = 2$  (Fig. 4.5(b)) where the gap shrinks and attains its minimum value at a critical point near  $J/|U| \sim 0.75$  and expands again for higher  $J/|U|$  values.

Now we concretely establish the PSF phase obtained from our CMFT simulations. To this end we first plot the particle density  $\rho$  as a function of  $\mu/|U|$  in Fig. 4.8 for a cut through the phase diagram in Fig. 4.5 (c). As indicated by the plateau in the curve, the system is gapped at  $\rho = 1$ . However, below  $\rho = 1$  plateau, the density of the system increases in steps of two particles as a function of  $\mu/|U|$  indicating the PSF phase (lower inset in Fig. 4.8). However, above the  $\rho = 1$  plateau, the system is in the SF phase where the density increases in steps of single-particle



**Figure 4.8:** DMRG data showing the  $\rho$  vs  $\mu/|U|$  plot for  $J/|U| = 0.04$  indicating the PSF and SF regions for  $L=80$ . The regions marked by the green squares are enlarged in the insets which show the signatures of the SF phase (upper inset) and the PSF phase (lower inset).

which is depicted in the upper inset of Fig. 4.8. To substantiate the PSF phase we plot the single- and two-particle correlations as a function of distance between the lattice sites  $r = |i - j|$  along leg-a for  $\rho = 0.875$  in Fig. 4.9. As expected, the two-particle correlation function ( $\Gamma_2(r) = \langle a_i^\dagger \rangle^2 \langle a_j \rangle^2$ ) exhibits a power-law decay and the single-particle correlation function ( $\Gamma_1(r) = \langle a_i^\dagger a_j \rangle$ ) decays exponentially .

From the above discussion we observe that the DMRG approach is more reliable to study the ground state properties of such low-dimensional systems. Nonetheless, both the CMFT and DMRG methods capture the underlying behaviour that when the hopping along the rung dominates over the hopping along the legs as well as the effective interaction strength, the system becomes a RI phase in the TBCs+HCBs system.

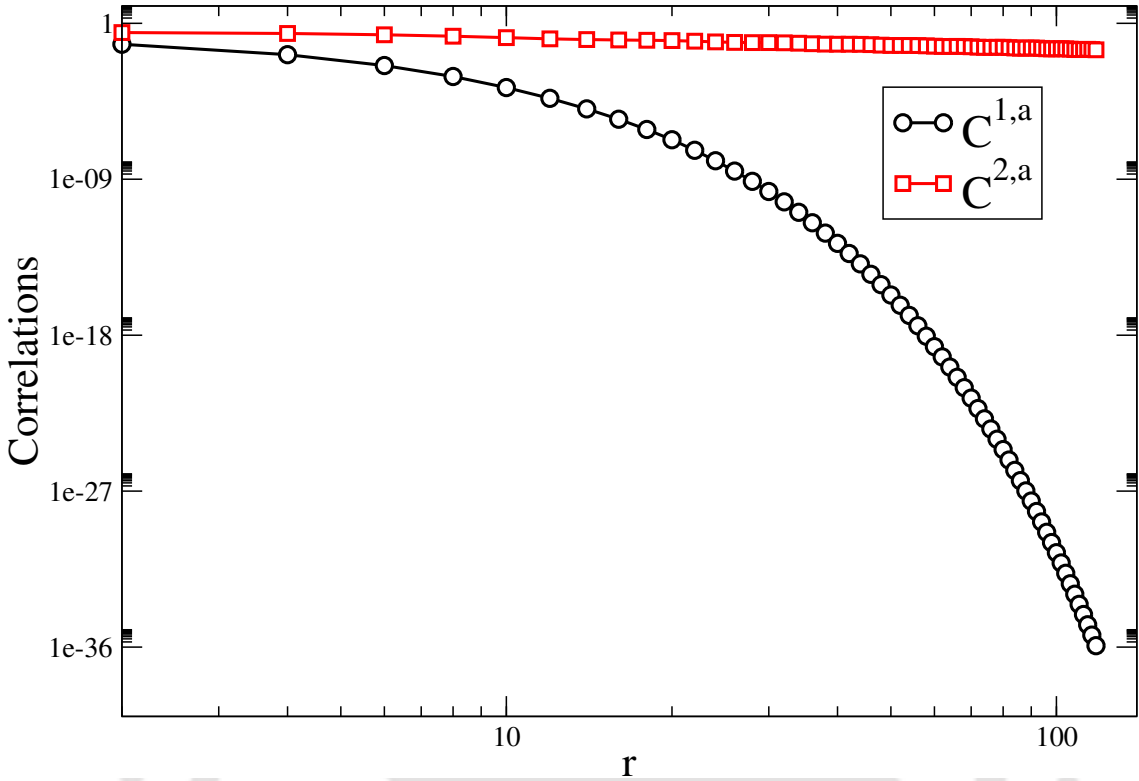


**Figure 4.9:**  $\Gamma_1(r)$  and  $\Gamma_2(r)$  for leg-a are plotted as a function of  $r = |i - j|$  in log-log scale at  $\rho = 0.833$  for  $J/|U| = 0.04$ . We consider the lattice sites in the range  $L/4$  to  $3L/4$  on a system of size  $L = 240$ .

### 4.3.2 The TBCs-TBCs system

In this section we extend our DMRG studies for a system when TBC imposed in both the legs of the ladder. In this case  $U$  is finite in both the legs and because of its attractive nature, dimers tend to form in each leg for stronger values of  $|U|$ . Due to the presence of finite  $J_\perp$  we get signatures of gapped dimer rung insulator phase or DRI phase where one gets dimers residing on the rungs through a second order tunneling process. To confirm these findings we plot  $\rho$  as a function of  $\mu/U$  for  $J/|U| = 0.04$  in Fig. 4.10. The plateau at  $\rho = 1$  indicates the gapped DRI phase. We find that the gapped DRI phase in this case undergoes a transition to the SF phase as  $J/|U|$  becomes stronger. In Fig. 4.11 we plot the extrapolated values of  $\mu^+$  and  $\mu^-$  as a function of  $J/|U|$  which clearly indicates a gapped DRI to gapless SF phase transition at  $J/|U| \sim 0.1$ . This transition can also be discerned by plotting the average rung correlations for the single and dimer correlations as shown in Fig. 4.12. It can be seen that the  $C_{avg}^{1,\perp}$  and  $C_{avg}^{2,\perp}$  intersect at a point  $J/|U| \sim 0.1$  after which the latter dominates over the former indicating the phase

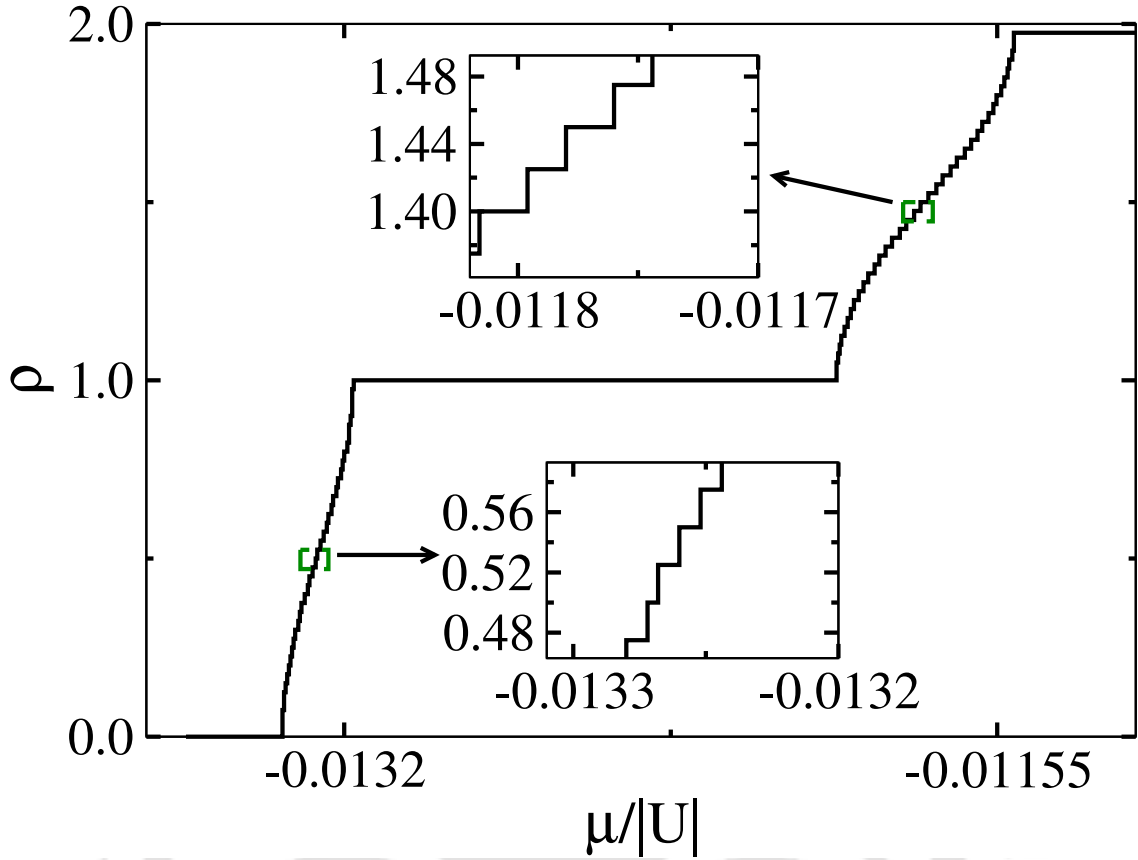


**Figure 4.10:** DMRG data shows the  $\rho$  vs  $\mu/|U|$  plot for  $J/|U| = 0.04$  indicating the PSF and DRI regions for  $L=80$  sites. The regions marked by the green squares are enlarged in the insets indicating the PSF phases.

transition. Note that the finite values of  $C_{avg}^{2,\perp}$  in the SF phase is expected due to finite single particle hopping strengths. Moreover, in this case we find that in the regions below and above  $\rho = 1$ , the density jumps in steps of two particles as a function of  $\mu/|U|$  (see insets of Fig. 4.10). This confirms the existence of the PSF phases before the system enters into the full and empty states. A detailed analysis of the phase diagram and transitions will be carried out elsewhere.

## 4.4 Conclusions

In this chapter we considered constrained bosons on a two-leg attractive Bose-Hubbard ladder with one leg having three-body constraints and the other one having hardcore constraints. By applying the CMFT method we obtained a gapped RI phase to gapless SF phase transition as a function of the leg hopping for some particular ratios of rung to leg hopping. The two-particle jump in the particle density

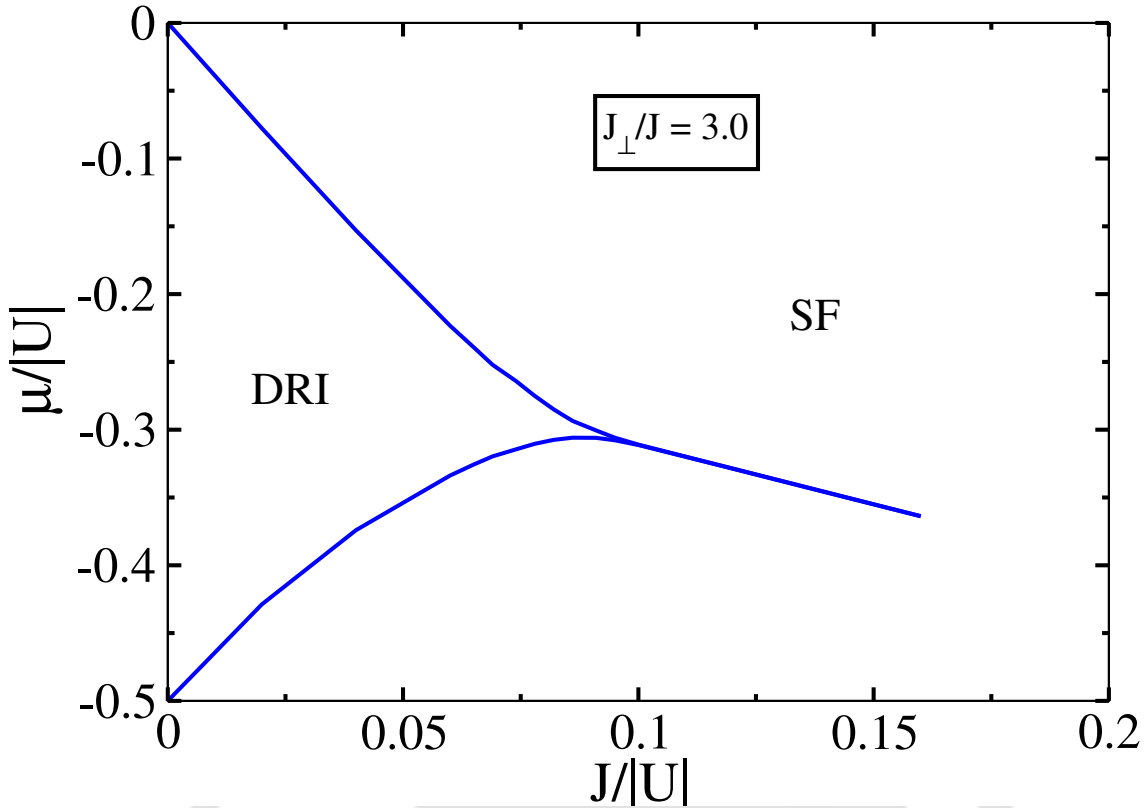


**Figure 4.11:** DMRG phase diagram of a TBCs+TBCs system showing a gapped-gapless transition from DRI phase to SF phase. The phase boundaries are obtained by extracting the extrapolated values of  $\mu^+$  and  $\mu^-$  with system sizes  $L = 40, 80, 120$  and  $160$ .

as a function of chemical potential and the finite two-particle hopping correlations indicate the existence of a PSF as well. Interestingly, for very large hopping ratios we observed that the gap of the RI phase does not close even for very strong hopping strengths. On the other hand the DMRG phase diagram shows a RI-SF phase transition via a critical point when the rung hopping is equal to the leg hopping. However, the gap does not close at all when the hopping along the rung is nearly twice or more than that of the leg. Instead, we get a transition/crossover from one gapped ( $RI_1$ ) phase to another gapped ( $RI_2$ ) phase through a region where the gap is minimum. By analysing the particle density and correlations we validated the existence of the PSF phase using DMRG.

We extended our investigations further and considered a system where both the legs have TBCs. Due to the attractive interaction between the particles, in this case we see the formation of dimers (bound bosonic pairs) which reside on the rungs of the ladder. As a result we obtain a dimer rung insulator (DRI) phase in the limit of small leg hopping. By utilizing the DMRG approach we show a phase transition

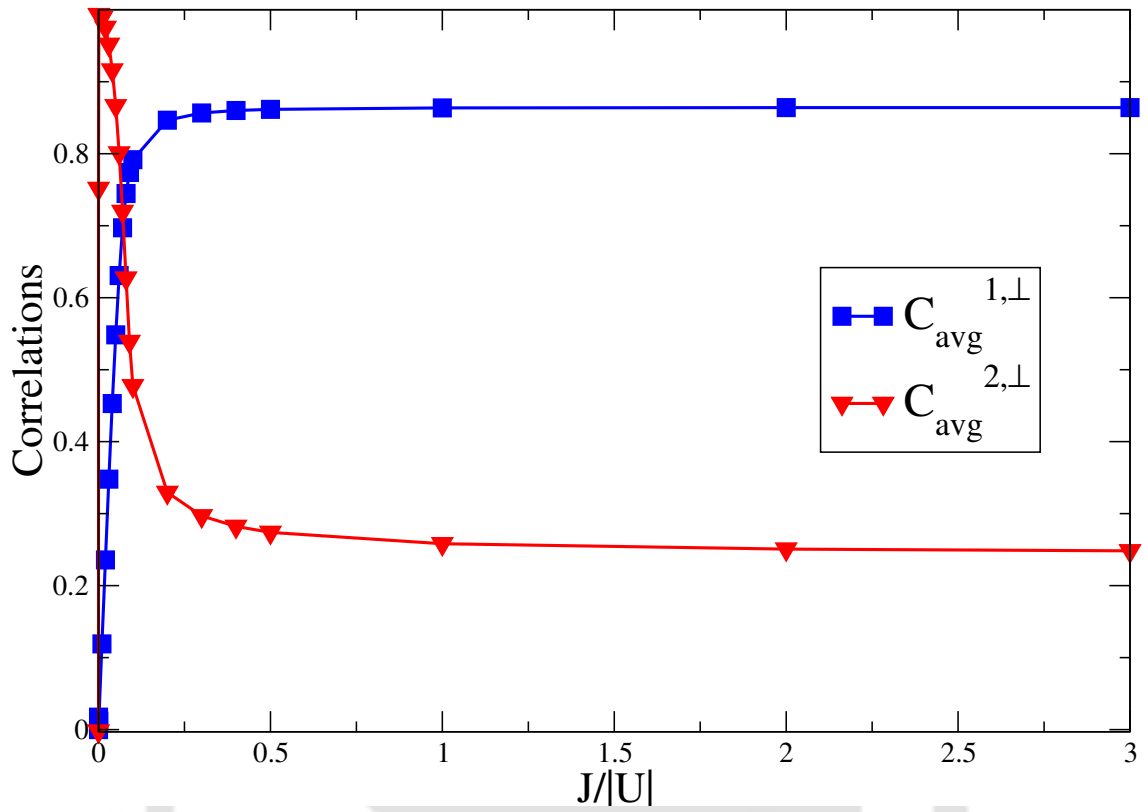


**Figure 4.12:** Single- and two-particle correlations averaged over all the rungs on a system of size  $L = 240$  for  $J_{\perp}/J = 3$ .

of the gapped DRI to gapless SF phase transition as a function of the leg hopping strength. In this case also we find signatures of the PSF phases.



## Chapter 5

# Correlated photon pair propagation in circuit QED with superconducting processors

### 5.1 Introduction

The phenomenon of pairing plays significant roles in different areas of fundamental physics ranging from condensed matter to atomic, molecular, and nuclear physics. Typically, in such systems, the two body attractions lead to the formation of bound states of constituent particles. However, in some specific cases, the bound pairs can be formed even in the presence of two-particle repulsion e.g., the cooper pairs of electrons [152] or in a superconductor. The two-body interactions whether attractive or repulsive lead to the formation of bound states of constituent particles. These pairs under proper conditions, may have significant contributions in establishing novel and exotic physical phenomena and contribute to technological applications. In recent years the simplest such pair formations(attractive and repulsive) have been predicted and experimentally observed in the context of interacting ultracold atomic systems in optical lattices [56, 77, 153]. These observations rely on the sophisticated control over the parameters associated with the optical lattice strength and/or the technique of Feshbach resonance [154]. Although, the atomic or molecular systems provide promising platforms to simulate several complex quantum many-body phenomena, there are certain limitations that can not be avoided due to various reasons. In particular, the formation of attractive pairs will require a three-body hardcore constraint which involves three-body inelastic losses [77] resulting in an extremely small lifetime of the atomic pairs. On the other hand, the formation of

Feshbach molecules are rovibrationally unstable and can reduce to the lower levels very easily. At this point, it is believed that the interacting photons can form stable bound pairs which can provide a promising platform to explore various fundamental phenomena and further the scope for technological applications. Several successful attempts have been made to create bound states of photons under different conditions [155–157]. The primary thrust and interest in creating photonic bound states rests not only to understand the fundamental physics of nature but also on possible practical applications in waveguide QED experiments [158, 159] and quantum simulation [160–163].

The realization of strong interaction between photons has been a topic of paramount interest in last several decades. The interaction which is believed to exist in optical non-linear media however, does not possess enough non-linearity to ensure strong interactions between photons. The field of quantum optics has paved the path in achieving strong non-linearity in various exciting platforms such as the optical cavities and superconducting circuits [164–166]. Several path breaking achievements have been made with cavity and circuit QED in recent years using the two-level artificial atoms(also known as qubits). In the many-body context, an array of such artificial atoms coupled by photons have shown to exhibit novel scenarios in the framework of the celebrated Jaynes-Cummings-Hubbard(JCH) model [30, 167–173]. The quantum phase transition between the superfluid(SF) and the Mott insulator(MI) of polaritons (the quasi-particles composed of atomic excitations and cavity photons) is an important revelation of the competing photon-atom interactions inside the cavity and the photon hopping between different cavities [30, 174]. Following this, many interesting quantum phenomena have been analyzed in the framework of the JCH model [175]. The phenomenal progress in understanding the many-body aspects of strongly correlated photons and the demand to fulfill the requirements necessary for quantum technologies have attracted enormous attention towards the study of the cavity and circuit QED [176]. Although, primarily the atom-photon interactions in such systems are of two-body repulsive and attractive in nature [167], recent progress in manipulating three- and higher-level systems have provided opportunities to explore novel scenarios in quantum simulations with multi-level systems [177–182].

Although the systems of atoms in optical cavities are well established to understand the physics of light-matter interaction, the rapid developments in fabricating superconducting circuits have evolved as one of the most suited test bed for quantum simulations in recent years. The versatility of these systems arises from the

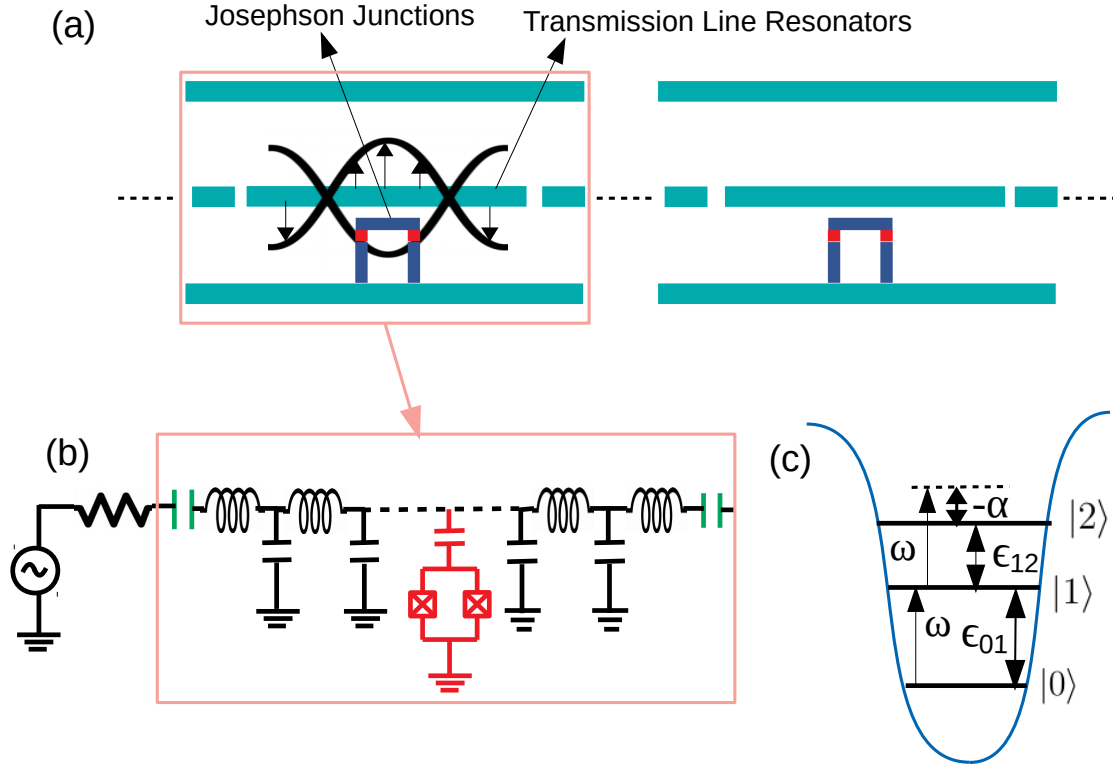


**Figure 5.1:** (a) Schematic layout of an array of coupled cavity QED system using transmons (not to scale) [3–6]. (b) Equivalent lumped circuit representation of a single transmon coupled to a single transmission line resonator by the coupling capacitors. (c) Shows the energy levels with only one driving frequency  $\omega$ . We set  $\omega = \epsilon_{01}$  ( $\hbar=1$ ) and  $\alpha = \epsilon_{12} - \omega$ .

flexibility to control the anharmonicity generated by the Josephson junctions which indirectly controls the interaction between the polaritons [183]. Motivated by all the recent developments we analyze the circuit QED of superconducting processor and propose a method to create photon pair propagation. Here we propose to use transmon [4, 184, 185] qubits truncated to the first three energy levels to create the bound photonic states.

## 5.2 Model and method

In this Chapter, we propose to use an array of transmission line resonators (TLRs) with capacitive coupling between two nearest neighbors and also each resonator coupled to a single transmon qubit truncated to the first three energy levels (known as qutrits). In Fig. 5.1 we present the case of a single transmon coupled to a single TLR via coupling capacitors and the TLRs are connected capacitively with one another. Here we consider the transmon mimicking an artificial three-level atomic

system in cascade( $\Xi$ ) configuration with unequal energy spacing's as depicted in Fig. 5.1(b). The energy difference between the levels  $|0\rangle$  and  $|1\rangle$  is denoted as  $\varepsilon_{01}$  and between  $|1\rangle$  and  $|2\rangle$  as  $\varepsilon_{12}$ . Here we consider the transmons and resonators are degenerate and therefore we set the cavity resonance frequency  $\omega = \varepsilon_{01}$ . While  $\omega$  represents the cavity resonance frequency,  $\Delta = \omega - \varepsilon_{12}$ , stands for the anharmonicity associated to the 2nd excited level. We define  $\alpha = \varepsilon_{12} - \varepsilon_{01}$  as the anharmonicity associated with the transmon. The cavity resonance frequency  $\omega$  is chosen in such a way that it will drive the transmons between the levels  $|0\rangle$  to  $|1\rangle$  and  $|1\rangle$  to  $|2\rangle$  and all transitions to the higher excited levels are suppressed [186, 187]. Employing the rotating wave approximation [4], the many-body physics of this system of coupled-cavity array(CCA) can be analyzed in the context of the modified JCH model [6] given as;

$$\begin{aligned} \mathcal{H}_{JCH} = & \sum_i \hbar[\alpha\sigma_{2i}^\dagger\sigma_{2i} + \beta_{12}(\sigma_{2i}^\dagger a_i + H.c.) \\ & + \beta_{01}(\sigma_{1i}^\dagger a_i + H.c.)] - \hbar\kappa \sum_{\langle i,j \rangle} (a_i^\dagger a_j + H.c.) \end{aligned} \quad (5.1)$$

Here,  $a_i^\dagger(a_i)$  is the photonic creation(annihilation) operator,  $\sigma_{1i}^\dagger(\sigma_{2i})$  is the atomic raising(lowering) operator which takes the atom from  $|0\rangle_i$  to  $|1\rangle_i$ ( $|2\rangle_i$  to  $|1\rangle_i$ ) levels,  $n_i = n_i^p + \sigma_{1i}^\dagger\sigma_{1i} + \sigma_{2i}^\dagger\sigma_{2i}$  is the total polariton number at the  $i^{th}$  cavity and  $n_i^p = a_i^\dagger a_i$  denotes the number operator of the photonic excitations.  $\beta_{01}(\beta_{12})$  represents the atom-photon coupling strength between level  $|0\rangle$  and  $|1\rangle$ ( $|1\rangle$  and  $|2\rangle$ ). The nearest neighbor inter-cavity photon tunneling amplitude is denoted by  $\kappa$ . For our analysis, we define the polariton density as  $\rho = N/L$ , where  $N = \sum_i n_i$  and  $L$  is the total number of polaritons and the total number of sites in the system respectively. Here we consider the transmons and resonators are degenerate and therefore we set the cavity resonance frequency  $\omega = \varepsilon_{01}$ .

As mentioned before in Section 5.1, the two-level JCH model exhibits SF-MI phase transition as a function of the ratio  $\kappa/\beta_{01}$ . There exist the MI phases at integer polariton densities when  $\kappa/\beta_{01}$  ratio is small and these phases are represented as  $MI(\rho)$ . In the limit  $\kappa \gg \beta_{01}$  the MI phases melt and a phase transition to the SF phase occurs due to the delocalization of photons. On the other hand, a recent mean-field study on a three-level atomic system with equally spaced levels in optical cavity arrays predicts the complete suppression of the  $MI(1)$  lobe after a critical  $\beta_{12}/\beta_{01} = \sqrt{2}$  [188]. In this limit, the  $MI(2)$  lobe is shown to overlap with the vacuum state and this signature is speculated to be of a pair-superfluid(PSF)

phase of polaritons in analogy with the attractive Bose-Hubbard model. The key requirement to achieve this phenomenon is that the two transitions,  $|0\rangle \rightarrow |1\rangle$  and  $|1\rangle \rightarrow |2\rangle$  should be near resonantly driven by the same photon (including the polarization) which demands equally spaced three-level  $\Xi$  system. However, we would like to stress that this condition is not satisfied by the natural atoms in optical cavities. Note that for the  $\Lambda$  and  $V$ -systems the frequency of two transitions can be the same but requires different polarizations of the photons.

Interestingly, this condition can be easily satisfied in transmon which plays the role of an artificial atom provided the higher energy levels except the first three are removed or truncated. The removal of the higher energy levels can be implemented by using strong anharmonicity to the system [4?] as depicted in Fig. 5.1(b). Therefore, in our studies we consider a more realistic system of three-level artificial atoms by considering a transmon with unequal spacings which will circumvent the practical issues associated with equal spacing  $\Xi$  system. Note that the anharmonicity naturally introduces the detuning for  $|1\rangle \rightarrow |2\rangle$  transition. To understand the effects of the strong correlations, we analyze the ground state properties of the model given in Eq. 5.1 for one and two dimensional arrays of transmons using the density matrix renormalization group(DMRG) [59, 60, 62] method and the self-consistent cluster mean-field theory(CMFT) approach [53, 56] respectively.

## 5.3 Results

### 5.3.1 Phase diagram in 1D

In this part, we discuss about the results in a one-dimensional circuit QED array with an experimentally realistic three-level  $\Xi$  system by considering  $\beta_{12}/\beta_{01} = \sqrt{2}$  [4] and finite detuning anharmonicity  $\alpha/\beta_{01} = -0.4$ . Note that the ratio  $\beta_{12}/\beta_{01}$  is smaller than  $\sqrt{2}$  due to the anharmonicity,  $\alpha$ . However, we have verified that the PSF phase exists for a wide range of  $\beta_{12}/\beta_{01}$  ratio. It is to be noted that there is no particular reason behind this choice of  $\alpha/\beta_{01} = -0.4$ . To get a clear numerical picture, we keep the value of  $\alpha/\beta_{01}$  close to the experimentally accessible regime [?]. By utilizing the DMRG method we compute the ground-state phase diagram in the plane of  $\kappa/\beta_{01}$  and  $\mu/\beta_{01}$  as shown in Fig. 5.2 where  $\mu$  is the chemical potential of the system. Note that the DMRG simulations are done in the canonical ensemble with fixed polariton number and hence the Hamiltonian of Eq. 5.1 is explicitly independent of  $\mu$ . It can be clearly seen from the phase diagram that the MI(2) lobe (red solid curve) appears

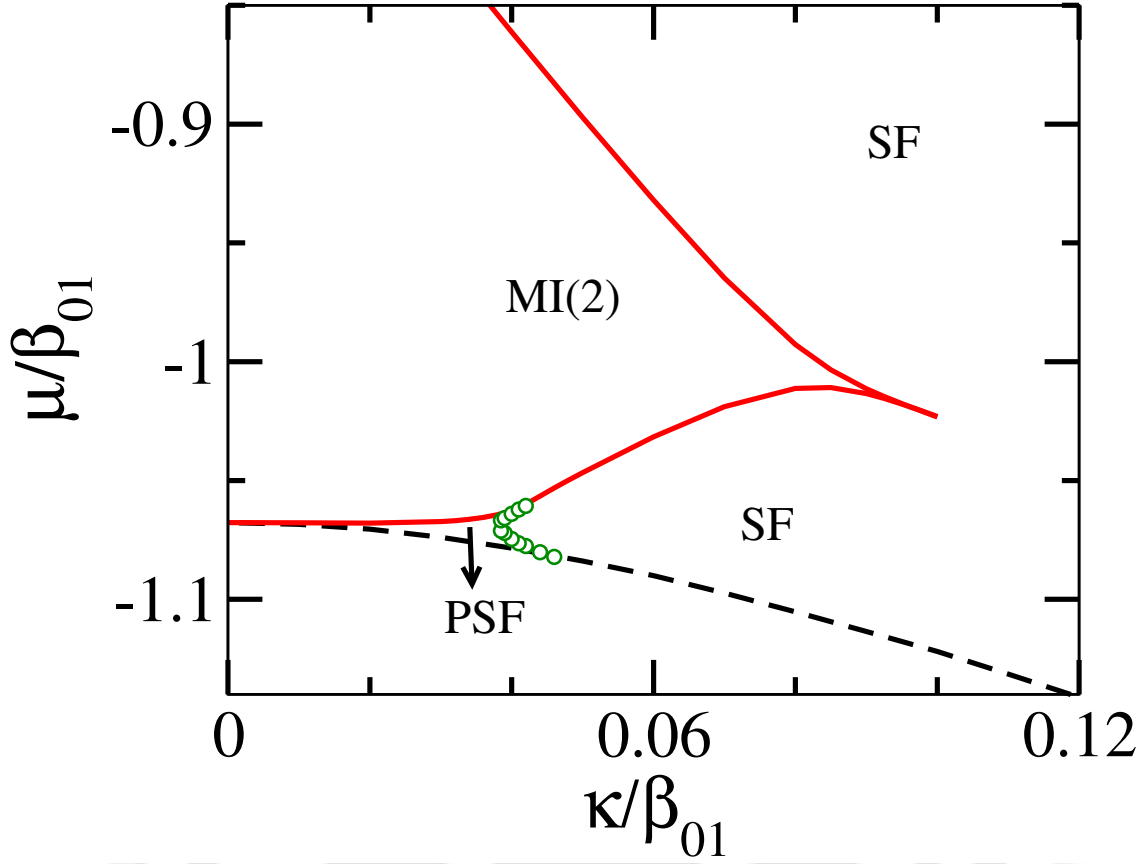


**Figure 5.2:** Phase diagram of the JCH model using the DMRG method in  $1d$  for the anharmonicity  $\alpha/\beta_{01} = -0.4$ . In this figure the red solid curve demarcates the boundary of the MI(2) phase, the green circles show the PSF-SF phase boundary and the black dashed curve is the vacuum state or the MI(0) phase. For the DMRG method in Fig. 5.2 all boundaries are calculated by extrapolating the chemical potential to thermodynamic limit using maximum system size of  $L = 80$  cavities.

immediately after the vacuum state (black dashed line) by completely suppressing the MI(1) lobe which usually appears in the phase diagram of the JCH model of two-level systems [30]. Moreover, in this case, there is no overlap of the vacuum and the MI(2) lobe as opposed to the MFT results shown in Ref. [188] in the absence of any anharmonicity. Interestingly there exists a PSF phase of polaritons in the gapless region bounded by the green circles for small values of  $\kappa/\beta_{01}$ . Before going to the details of this PSF phase we first discuss about the phase diagram in the following.

First of all, we trace out the phase transition from the gapped MI(2) phase to the SF phase of polaritons by looking at the energy gaps in the system. The signature of the gapped MI(2) phase is seen as the plateaus in the  $\rho$  vs  $\mu/\beta_{01}$  plot at  $\rho = 2$  as shown in Fig. 5.3(a) which is a signature of the gap in the system.

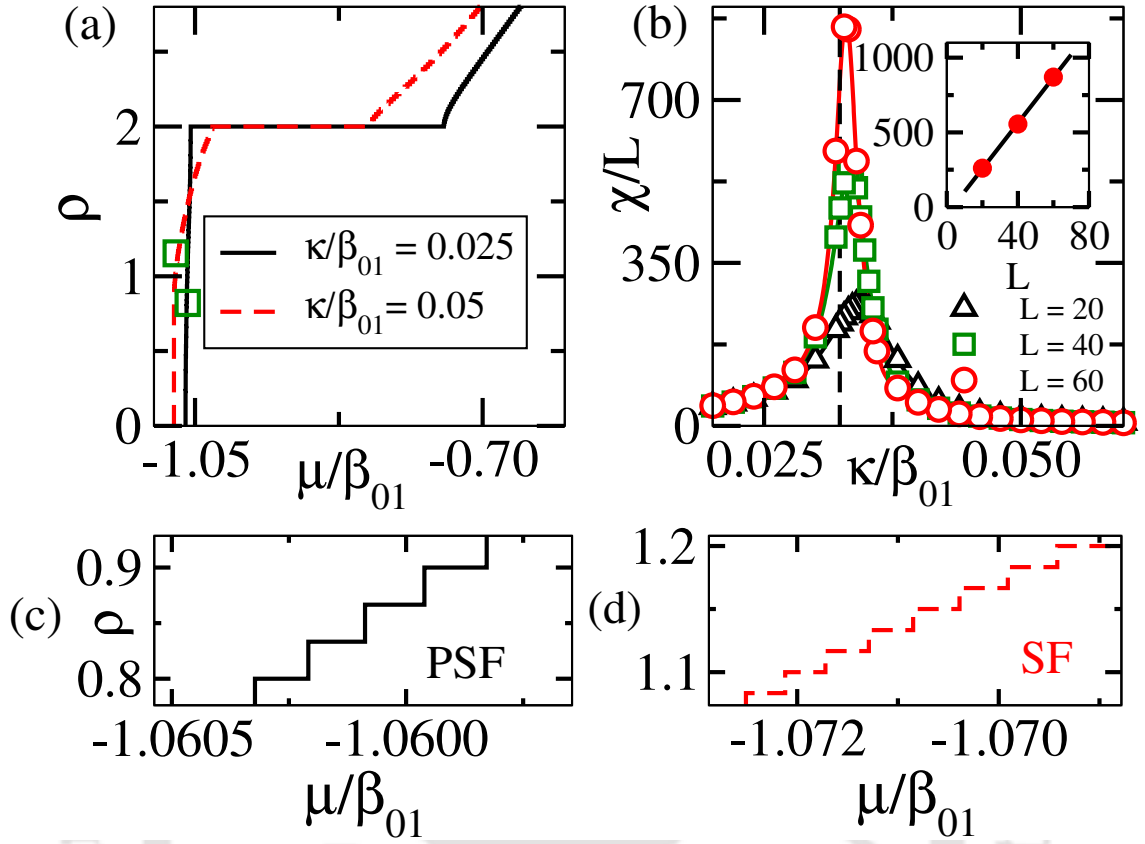


**Figure 5.3:** (a) DMRG data shows the  $\rho$  vs  $\mu/\beta_{01}$  plot for parameters  $\kappa/\beta_{01} = 0.025$  and  $\kappa/\beta_{01} = 0.05$  when  $\alpha/\beta_{01} = -0.4$  indicating the SF and PSF regions for  $L = 60$  sites. The regions marked by the green boxes are enlarged in Figs. 5.3(c) and (d) which shows the signatures of the PSF and the SF phases respectively. (b)  $\chi_{FS}(\vec{k})$  vs.  $\kappa/\beta_{01}$  plots for different system sizes of  $L = 20, 40$  and  $60$  to see the phase transition point. (Inset) Shows that the peak heights diverge with system size indicating the phase transition. The dashed vertical line corresponds to the critical point of transition determined by extrapolating the peak position to thermodynamic limit.

The phase boundaries are obtained by computing the extrapolated values of the endpoints of the plateaus which are the chemical potentials of the systems defined as  $\mu^+ = E_{N+1} - E_N$  and  $\mu^- = E_N - E_{N-1}$  in the thermodynamic limit for different values of  $\kappa/\beta_{01}$ . Here,  $E_N$  is the ground state energy with  $N$  polaritons. Now we systematically analyze the signatures of the pair formation in the system. The immediate information can be obtained by analyzing the dependence of  $\rho$  with respect to  $\mu/\beta_{01}$  for different values of  $\kappa/\beta_{01}$ . In Fig. 5.3(a) we plot  $\rho$  vs  $\mu/\beta_{01}$  correspondings to two different values of  $\kappa/\beta_{01} = 0.025$  (black solid) and  $0.05$  (red dashed) of the phase diagram in Fig. 5.2. Note that when  $\kappa/\beta_{01} = 0.05$ , the value of  $\rho$  increases in steps of one particle, indicating the SF phase. However, for  $\kappa/\beta_{01} = 0.025$ , the value of  $\rho$  increases in steps corresponding to the change in polariton

number  $\Delta n = 2$  up to the MI(2) plateau from the bottom. This can be clearly seen from the zoomed-in regions plotted in Figs. 5.3(c) and (d) corresponding to the green boxes shown in Fig. 5.3(a). This indicates the quasiparticle excitations in terms of polariton pairs which is a typical signature of the pair formation [56, 189, 190]. This phenomenon happens in the gapless region between the vacuum and the MI(2) phase in the regime of small  $\kappa/\beta_{01}$  and therefore can be called as a PSF phase of polaritons. As a result, there exists a phase transition from the SF phase to the PSF phase as a function of  $\kappa/\beta_{01}$  which is indicated by the green circles in Fig. 5.2. We compute the PSF-SF phase boundary from the  $\rho$  vs  $\mu/\beta_{01}$  plot and complement it by looking at the divergence of the fidelity susceptibility [56, 191] across the phase transition defined as:

$$\chi_{FS}(\tilde{\kappa}) = \lim_{\tilde{\kappa} - \tilde{\kappa}' \rightarrow 0} \frac{-2 \ln |\langle \Psi_0(\tilde{\kappa}) | \Psi_0(\tilde{\kappa}') \rangle|}{(\tilde{\kappa} - \tilde{\kappa}')^2}, \quad (5.2)$$

at  $\rho = 1.5$ . Here  $\tilde{\kappa} = \kappa/\beta_{01}$ ,  $|\Psi_0\rangle$  is the ground-state wave function and  $\tilde{\kappa}'$  is a small change in the rescaled hopping amplitude. From Fig. 5.3(b), we observe a diverging stable maximum with increasing system sizes which shows the PSF-SF phase transition point at  $\kappa/\beta_{01} = 0.03237$ .

Although, the  $\rho$  vs.  $\mu/\beta_{01}$  behavior allows us to identify the PSF phase of polaritons, it does not provide any insight about the underlying mechanism behind this.

### 5.3.2 The PSF phase

We devote this part of the chapter to provide a detailed analysis of the physics of photon pair propagation and the PSF phase of polaritons. To understand the pairing phenomena we rely on the behavior of various single and pair correlation functions. In Fig. 5.4 we plot all the correlation functions with respect to the distance  $|i - j|$  for a system of length  $L = 80$  and  $\kappa/\beta_{01} = 0.01$ . Interestingly, it can be seen in Fig. 5.4(a) that the correlation functions associated with the photon pairs which is defined as  $\Gamma_{\text{photon-pair}}(i, j) = \langle b_i^\dagger b_j^\dagger \rangle$  (black dots) exhibits algebraic decay, whereas the single-photon correlation i.e.  $\Gamma_{\text{photon}}(i, j) = \langle b_i^\dagger b_j \rangle$  (blue dot-dashed) decays exponentially. This is a clear indication of the existence of the long-range coherence of photon pairs in the system and the single-particle motion is completely suppressed in the thermodynamic limit. At the same time, the atom-pair correlation defined as  $\Gamma_{\text{atom-pair}}(i, j) = \langle \sigma_{02,i}^\dagger \sigma_{02,j} \rangle$  (green solid) also remains finite whereas the single atom correlation  $\Gamma_{\text{atom}}(i, j) = \langle \sigma_{01,i}^\dagger \sigma_{01,j} \rangle$  (red dashed) vanishes exponentially across the ar-

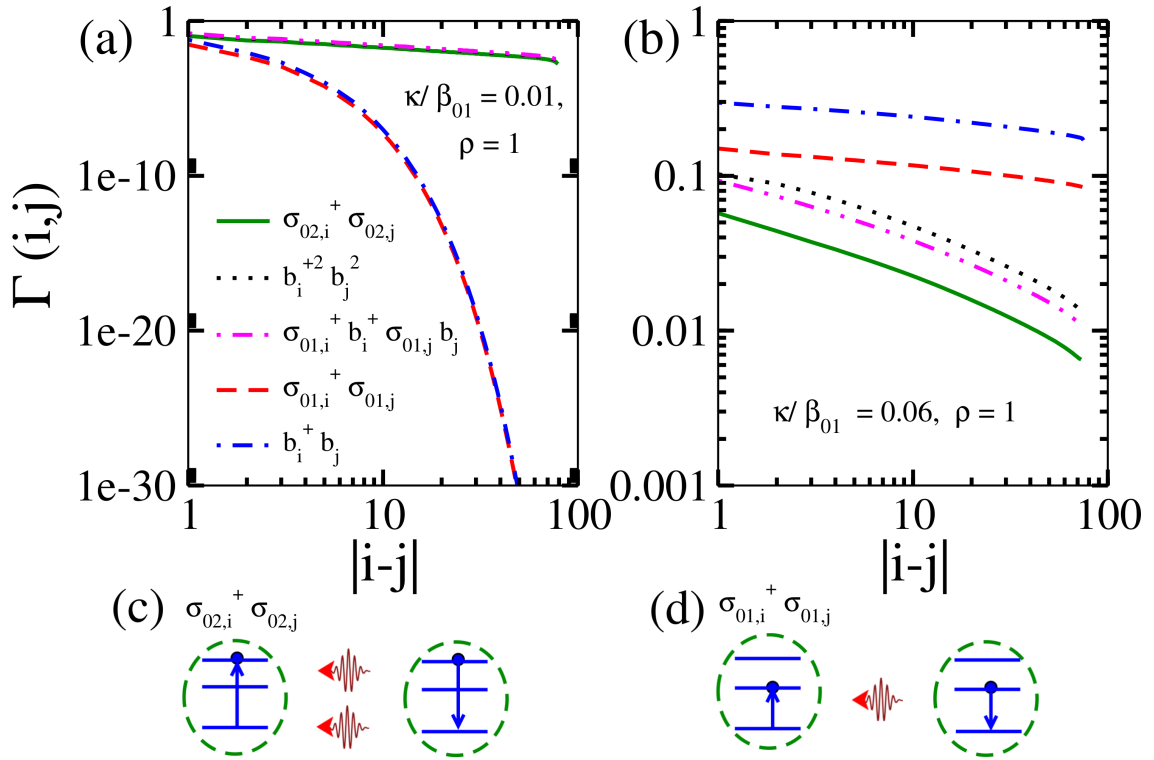


**Figure 5.4:** Figure shows the pair and single polariton correlation functions  $\Gamma(i, j)$  with distance  $|i - j|$  for  $\rho = 1$  with (a)  $\kappa/\beta_{01} = 0.01$  and (b)  $\kappa/\beta_{01} = 0.06$ . Figs. (c) and (d) shows the two photon and single photon tunneling processes respectively.

ray. This implies that a pair of photon gets spontaneously emitted from a cavity and gets absorbed by the nearest neighbor cavity and excite the atom sitting there. This process continues resulting in the superfluid of photon pairs. Here  $\sigma_{01,i}$  ( $\sigma_{02,i}$ ) are the annihilation operators associated with the atomic excitations from the ground state to the first and second levels respectively. On the other hand for large values of  $\kappa/\beta_{01}$  we have verified that the single-particle correlation functions dominate over the pair ones justifying the SF phase as depicted in Fig. 5.4(b). The physical process which may arise from this single and pair photon propagations is depicted in Figs. 5.4 (d) and (c) respectively. Interestingly, we also find that in the limit of two-photon propagation there exists finite correlation corresponding to the single-photon and an atomic excitation that is  $\Gamma_{atom-photon}(i, j) = \langle \sigma_{01,i}^\dagger b_i^\dagger \sigma_{01,j} b_j \rangle$ . Hence in the present case, we can have three different scenarios such as (a)  $|n_p = 2, n_a = 0\rangle$ , (b)  $|n_p = 1, n_a = 1\rangle$  and (c)  $|n_p = 0, n_a = 2\rangle$  which can facilitate the photon pair propagation between the SQCs for small  $\kappa/\beta_{01}$  values. The physics behind such photonic pair creation or photon pair propagation can be understood by analyzing the energies associated with the system as done in Ref. [188]. In the SF regime where

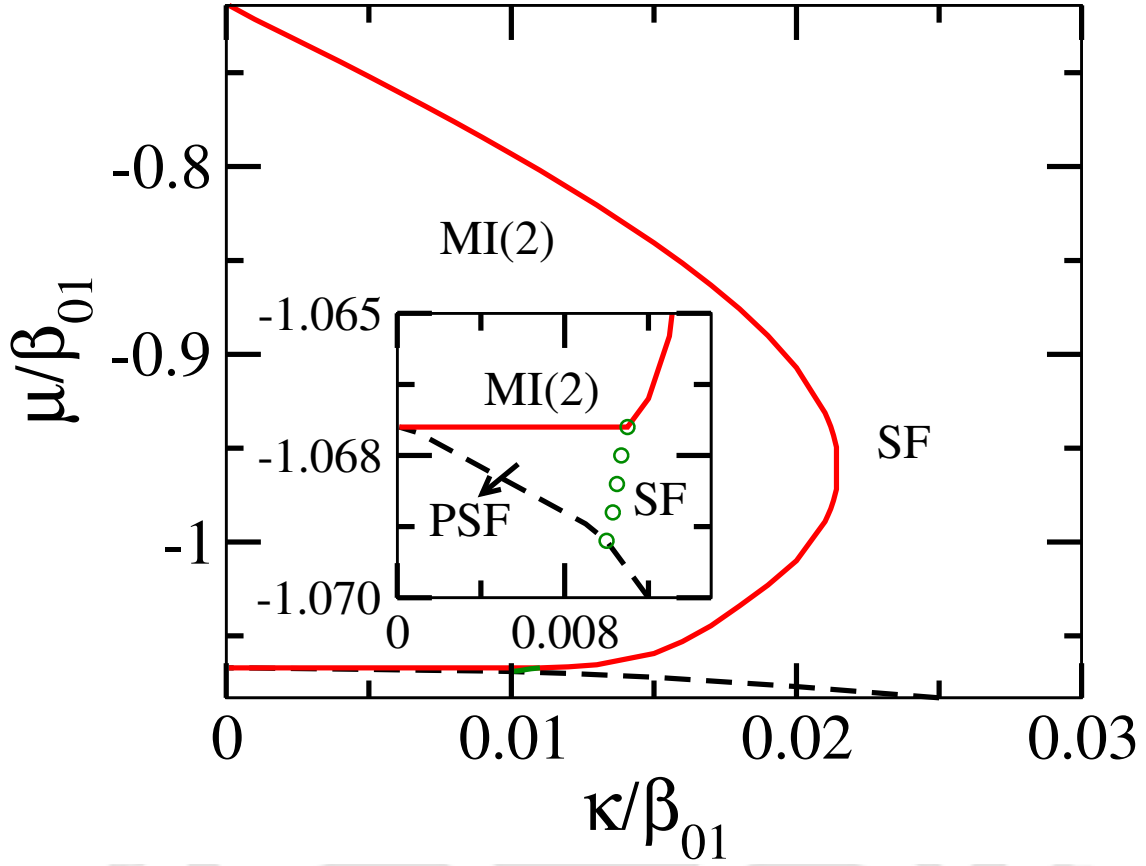


**Figure 5.5:** Phase diagram of the JCH model using the CMFT method in  $2d$  for the anharmonicity  $\alpha/\beta_{01} = -0.4$ . In this figure the red solid curve demarcates the boundary of the MI(2) phase, the green circles show the PSF-SF phase boundary and the black dashed curve is the vacuum state or the MI(0) phase. In the inset of Fig. 5.5 we show the enlarged PSF region.

the single-photon processes take place, the artificial atom can go from  $|n_a = 0\rangle$  to  $|n_a = 1\rangle$  or  $|n_a = 1\rangle$  to  $|n_a = 0\rangle$  or  $|n_a = 1\rangle$  to  $|n_a = 2\rangle$  or  $|n_a = 2\rangle$  to  $|n_a = 1\rangle$  as shown in Fig. 5.4(d).

We show in Fig. 5.7 that for  $\alpha/\beta_{01} = -0.4$ , the cavity excitation energy corresponding to two-photon becomes negative, whereas the energy corresponding to other higher polaritonic excitation remains positive well before  $\beta_{12}/\beta_{01} = \sqrt{2}$ . This promotes the formation of two polaritons in the transmons and indirectly the photon pair propagation. Therefore, the photon pair propagation and the associated polaritonic PSF phase in the three-level JCH model is not identical to the atomic PSF phase in the BH model due to the attractive interaction between bosons.

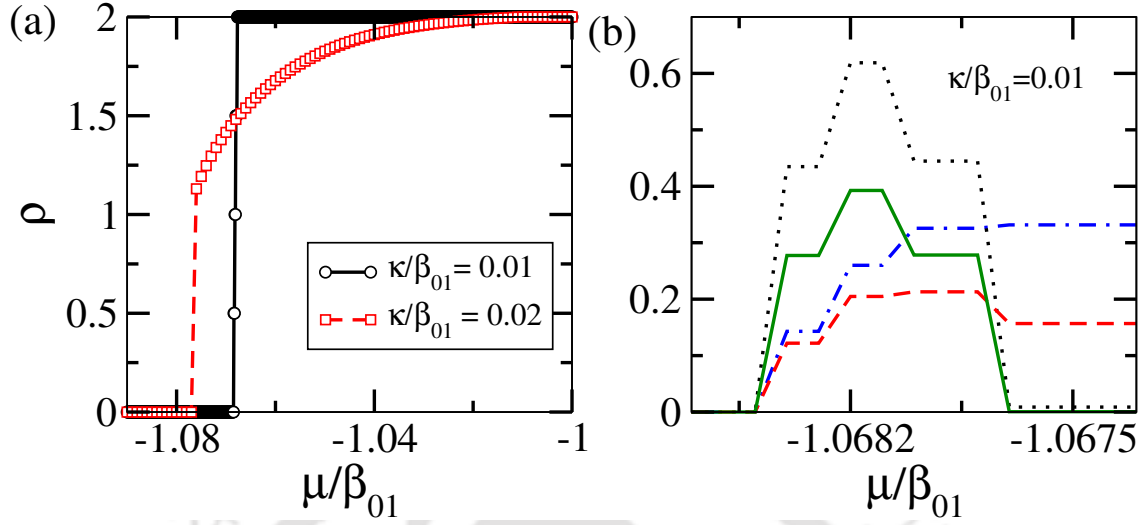


**Figure 5.6:** (a)  $\rho - \mu/\beta_{01}$  plot at  $\kappa/\beta_{01} = 0.01$  and  $0.02$  of Fig. 5.5. (b) Different correlation functions such as  $\Gamma_{atom-pair}(i, j)$  (Green solid),  $\Gamma_{photon}(i, j)$  (blue dot-dashed),  $\Gamma_{photon-pair}(i, j)$  (black dots) and  $\Gamma_{atom}(i, j)$  (red dashed) are plotted for  $\kappa/\beta_{01} = 0.01$  (see text).

### 5.3.3 Phase diagram in 2D

After obtaining the signature of the photon pair propagation in the one dimensional circuit QED setup, we analyze the physics of the JCH model using the CMFT approach by going to two dimensions. Note that the CMFT approach works in the grand canonical ensemble, and hence we explicitly include the term associated to the chemical potential as  $\mu \sum_i n_i$  in the JCH model given in Eq. 5.1. In this method, the entire system is divided into identical clusters of a limited number of sites which can be treated precisely and then the coupling between different clusters are treated in a mean-field way. The accuracy of this method improves by increasing the number of sites in the cluster. With this approximation the original Hamiltonian of Eq. 5.1 can be written as

$$\begin{aligned} \mathcal{H}_{CMF} &= \mathcal{H}_C + \mathcal{H}_{MF} \\ &= \mathcal{H}_C - \kappa \sum_{\langle i, j \rangle} [(a_i^\dagger + a_i)\psi_j - \psi_i^* \psi_j] \end{aligned} \quad (5.3)$$

where,  $\mathcal{H}_C$  ( $\mathcal{H}_{MF}$ ) is the cluster (mean-field) part of the Hamiltonian and  $\psi_i = \langle a_i^\dagger \rangle = \langle a_i \rangle$  is the SF order parameter. The form of  $\mathcal{H}_C$  is same as Eq. 5.1 and is limited to the cluster only.

The self-consistent solution of the CMFT Hamiltonian yields the ground-state phase diagram in two dimension as depicted in Fig. 5.5. It can be seen that the

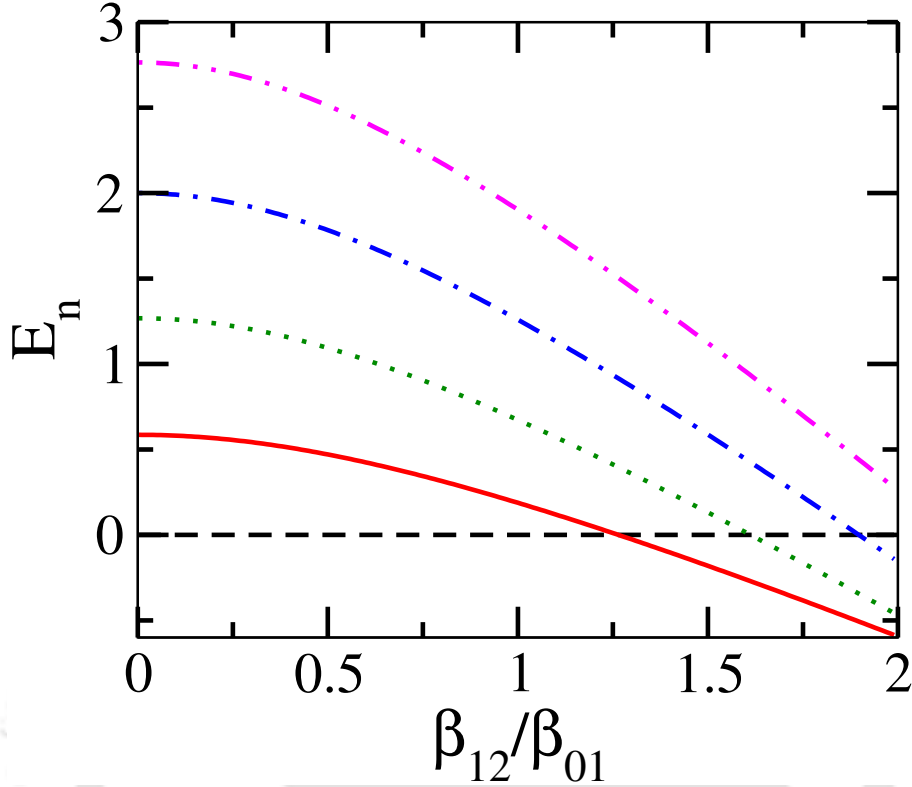


**Figure 5.7:** The polariton energies  $E_n$ (bottom to top for  $n = 1 \rightarrow 5$  at the origin) for  $\mu/\beta_{01} = -1$  with respect to  $\beta_{12}/\beta_{01}$  for  $\alpha/\beta_{01} = -0.4$ .

phase diagram in  $2d$  is qualitatively similar to the one obtained for the  $1d$  case (Fig. 5.2). The phase diagram of Fig. 5.5 is obtained by looking at the behavior of the density  $\rho = \frac{1}{L} \sum_i n_i = \frac{1}{L} \sum_i (n_i^p + n_i^a)$  with respect to  $\mu$  for different values of  $\kappa/\beta_{01}$ . In Fig. 5.6(a), we plot the values of  $\rho$  vs.  $\mu/\beta_{01}$  along with the cuts through the CMFT phase diagram of Fig. 5.5 at  $\kappa/\beta_{01} = 0.01$  and  $\kappa/\beta_{01} = 0.02$  which passes through different phases. The discrete jumps in the  $\rho - \mu/\beta_{01}$  plot (black circles) in steps of two particles is an indication of the PSF phase as discussed before in Section 5.3.2 and the plateaus at  $\rho = 2$  corresponds to the MI(2) phase. We also plot the correlation functions for a single photon, a pair of photons, a single atom, and a pair of atoms, as shown in Fig. 5.6(b). As the cluster is of four sites only, the correlations are computed between the nearest neighbors and averaging them over the entire cluster. This clearly shows the dominant pair correlation functions as compared to the single-particle ones(see figure caption for details).

In the experimentally realizable regime, the value of  $\beta_{12}/\beta_{01}$  must be less than  $\sqrt{2}$  due to the finite anharmonicity of the transmon. Here we consider the case where  $\beta_{12}/\beta_{01} = 1.35$ ,  $\kappa/\beta_{01} = 0.01$  and  $\alpha/\beta_{01} = -0.4$  and obtained the signature of

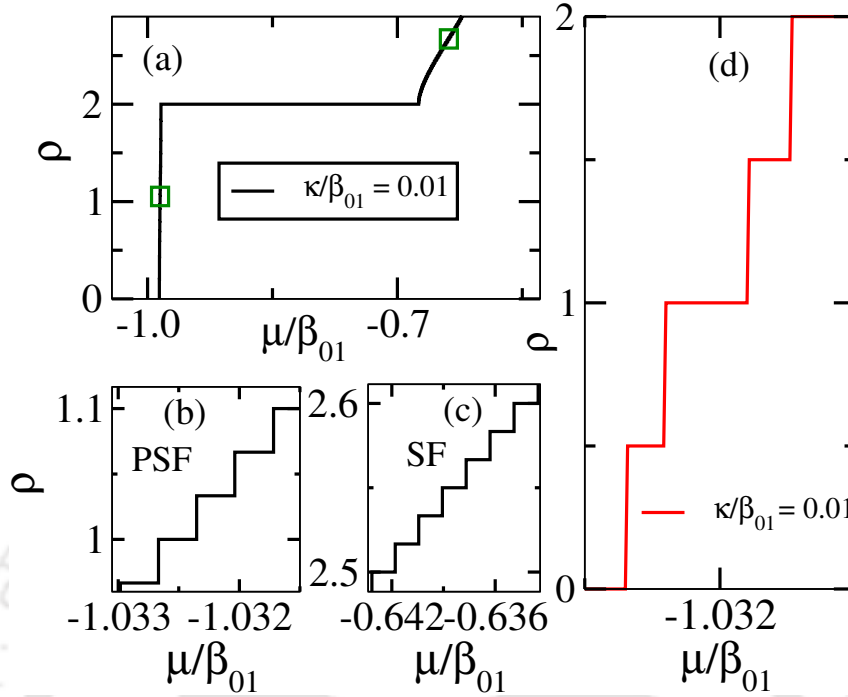


**Figure 5.8:** (a) DMRG data shows the  $\rho$  vs.  $\mu/\beta_{01}$  plot (black solid) for parameters  $\kappa/\beta_{01} = 0.01$  when  $\alpha/\beta_{01} = -0.4$  indicating the PSF and SF regions for  $L = 60$  sites in 1d. The regions marked by the green boxes are enlarged in Figs. 5.8 (b) and (c) which shows the signatures of the PSF and the SF phases respectively. (d) CMFT data for the  $\rho$  vs  $\mu/\beta_{01}$  plot (red solid) for  $\kappa/\beta_{01} = 0.01$  and  $\alpha/\beta_{01} = -0.4$  indicating the PSF phase for 4 sites in 2d.

PSF phase for both 1d and 2d systems using the DMRG and the CMFT methods respectively, as shown in Fig. 5.8. In Fig. 5.8(a), we plot the  $\rho$  vs.  $\mu/\beta_{01}$  data obtained using the DMRG method. In the PSF region, the discrete jumps in density  $\rho$  correspond to the change in polariton number  $\Delta n = 2$ , whereas in the SF region, the polariton number changes in steps of  $\Delta n = 1$  as indicated in the zoomed-in regions plotted in Figs. 5.8(b) and (c), respectively. In Fig. 5.8 (d) we plot the  $\rho$  vs.  $\mu/\beta_{01}$  data obtained using the CMFT method for  $\kappa/\beta_{01} = 0.01$  showing the discrete jumps in steps of two particles, which indicates the PSF phase of polaritons.

## 5.4 Conclusions

In this work, we propose a scheme for spontaneous photon pair creation and propagation in an array of coupled transmons. Considering the three-level artificial atoms of  $\Xi$  type instead of the usual two-level qubit systems, we analyze the corresponding Jaynes-Cummings Hubbard model in one and two-dimensional arrays using the

DMRG and the CMFT approach to establish the emergent photon pair propagation in the system. We show that for the suitable ratio of the coupling strengths between different levels, the single-photon tunneling is suppressed, and photons tend to move in pairs. This two photon propagation leads to the formation of polaritonic pair superfluid phase, which is located in between the vacuum and the MI(2) phases of the polaritonic phase diagram. This finding is obtained by considering a more realistic setup of the transmons of a three-level atom with unequal level spacings that are experimentally more feasible than the optical cavity-atom arrangements. We would like to note that in this case, there exists no overlap between the vacuum state and the MI(2) phase or the first-order type phase transition as predicted earlier using the MFT approach [188]. This inconsistency can be attributed to the artifact of the simple mean-field theory approach using which it is difficult to capture all the relevant physics arising due to the off-site correlations as rightly mentioned in Ref. [188].

This analysis provides a promising platform to observe the pairing phenomena of bosons in general as compared to its atomic and molecular counterparts. Moreover, this finding in the three-level system can possibly be made useful for quantum communications [160–163, 192–195] in the future as a bound state of photons is believed to carry more information than the individual photon. This work can shed light on the controlled creation and manipulation of boson pairs and can be extended to create higher-order photonic bound states(trimers etc.) in an array of multi-level artificial atoms.

## Chapter 6

# Conclusions and Future Directions

In this thesis, we have studied the quantum phases of constrained bosons in low dimensions such as in one, quasi-one and two dimensional lattices. In this regard we have explored the ground state properties of such constrained bosons in presence of different interactions using numerical methods such as the CMFT and the DMRG method.

Motivated by the theoretical and experimental developments in systems of ultracold atoms in optical lattices to access multi-body onsite interactions, we have analyzed the ground-state properties of a system of interacting bosons in a bilayer superlattice with interlayer repulsion which can be introduced by the dipole-dipole interactions <sup>3</sup>. Considering the bosons in one layer as soft core in nature and separately allowing two- and three-body hard-core constraints in the other layer, we obtained the ground-state phase diagram using the CMFT approach. The phase diagrams are found to exhibit various gapped MI phases at integer and half-integer densities. Due to the competition between the superlattice potential, intra- and interlayer interactions and the constraints on the bosons of layer B lead to interesting features in the phase diagram revealing the MI phases at different incommensurate densities.

In Chapter 4, we discuss the quantum phase transitions of a two leg ladder system with one leg having hardcore constraint and the other leg having three body constraints imposed in the regime of attractive on-site interaction. We have investigated the role of inter-leg (rung) hopping with the other energy scales such as the onsite interaction and the leg-hoppings in the system at different densities. We have found that in the limit of weak rung hopping, the system exhibits a phase transition from a gapped rung-insulator phase to a gapless superfluid phase as a function of the leg hopping at unit filling. However, when the rung hopping is strong, the system

always remains gapped and exhibits signatures of a rung-insulator phase. However, in our DMRG analysis we show that the nature of the rung-insulator for weak hopping is different from that of the strong hopping case. While the former is found to arise due to the onset of the full state of the leg having three-body constraint, the latter is due to the onset of an effective hardcore nature of the three-body constrained bosons. By moving away from unit filling, we have found signatures of the pair superfluid phase in one leg. We have extended this analysis for a system having three-body constrained bosons in both the legs and found the signatures of dimer-rung-insulator phase.

Finally, in Chapter 5 we propose a scheme for spontaneous photon pair creation and propagation in an array of coupled transmons. Considering the three-level artificial atoms of  $\Xi$  type instead of the usual two-level qubit systems we analyze the corresponding Jaynes-Cummings Hubbard model in one and two dimensional arrays using the DMRG and the CMFT approach to establish the emergent photon pair propagation in the system. We show that for the suitable ratio of the coupling strengths between different levels, the single photon tunneling is suppressed and photons tend to move in pairs. This two photon propagation leads to the formation of polaritonic pair superfluid phase.

## 6.1 Future Directions

The topics covered in the thesis deals with some of the timely problems which are of current importance in the context of strongly correlated low dimensional systems. The outcome of the thesis promises several possible extension which can be addressed immediately. We list some of them in the following.

The prediction of the quantum phases on a two-leg ladder Bose-Hubbard model can be explored in the context of superconducting circuits. This will enable to achieve the features of strongly correlated photons in such complex systems. The role of longer range interactions can be investigated which may reveal the possible existence of the charge density wave ordering and the supersolid phases.

On the other hand low dimensional systems are extremely useful to study the topological phase transitions. In this context, it will be worthwhile to address the topological properties of such constrained systems by allowing dimerized hopping in such coupled systems. This may allow for the study of symmetry protected topological phases of interacting bosons in two leg ladder systems.

Apart from these immediate extensions, it will be possible to address the quan-

tum phases of bosons on a two-leg ladder system in presence of artificial gauge fields using attractive onsite interactions. Earlier the physics of a two leg ladder system having repulsive two body interactions have been already studied in this context [196–198]. These have resulted in many interesting phases like the Meissner phases, vortex fluids, vortex lattices, charge density waves, and the biased-ladder phase. Similar analysis can be performed in the case of attractive constrained bosons in quasi-one dimensional systems.





# Bibliography

- [1] I. Bloch, *Nature* **453**, 1016 (2008).
- [2] M. Greiner, O. Mandel, T. Esslinger, T. W. Hänsch, and I. Bloch, *Nature* **415**, 39 (2002).
- [3] A. Blais, R.-S. Huang, A. Wallraff, S. M. Girvin, and R. J. Schoelkopf, *Phys. Rev. A* **69**, 062320 (2004).
- [4] J. Koch et al., *Phys. Rev. A* **76**, 042319 (2007).
- [5] A. Blais, J. Gambetta, A. Wallraff, D. I. Schuster, S. M. Girvin, M. H. Devoret, and R. J. Schoelkopf, *Physical Review A* **75**, 032329 (2007).
- [6] A. A. Houck, H. E. Türeci, and J. Koch, *Nature Physics* **8**, 292 (2012).
- [7] C. Gross and I. Bloch, *Science* **357**, 995 (2017).
- [8] T. Stöferle, H. Moritz, C. Schori, M. Köhl, and T. Esslinger, *Phys. Rev. Lett.* **92**, 130403 (2004).
- [9] M. Lewenstein, A. Sanpera, V. Ahufinger, B. Damski, A. Sen(De), and U. Sen, *Advances in Physics* **56**, 243 (2007).
- [10] W. Hofstetter and T. Qin, *Journal of Physics B: Atomic, Molecular and Optical Physics* **51**, 082001 (2018).
- [11] L. Tarruell and L. Sanchez-Palencia, *Comptes Rendus Physique* **19**, 365 (2018).
- [12] R. Grimm, M. Weidemüller, and Y. B. Ovchinnikov, *Optical Dipole Traps for Neutral Atoms*, volume 42, pages 95–170, Academic Press, 2000.
- [13] C. Becker, P. Soltan-Panahi, J. Kronjger, S. Drscher, K. Bongs, and K. Sengstock, *New Journal of Physics* **12**, 065025 (2010).
- [14] W. S. Bakr, J. I. Gillen, A. Peng, S. Fölling, and M. Greiner, *Nature* **462**, 74 (2009).
- [15] M. P. A. Fisher, P. B. Weichman, G. Grinstein, and D. S. Fisher, *Phys. Rev. B* **40**, 546 (1989).
- [16] D. Jaksch, C. Bruder, J. I. Cirac, C. W. Gardiner, and P. Zoller, *Phys. Rev. Lett.* **81**, 3108 (1998).
- [17] H. A. Gersch and G. C. Knollman, *Phys. Rev.* **129**, 959 (1963).
- [18] J. J. Sakurai and J. Napolitano, *Modern Quantum Mechanics*, Cambridge University Press, Cambridge, 2 edition, 2017.
- [19] I. Bloch, J. Dalibard, and W. Zwerger, *Rev. Mod. Phys.* **80**, 885 (2008).
- [20] H. Feshbach, *Annals of Physics* **5**, 357 (1958).
- [21] K. Sheshadri, H. R. Krishnamurthy, R. Pandit, and T. V. Ramakrishnan, *Euro-*

## BIBLIOGRAPHY

---

- physics Letters (EPL) **22**, 257 (1993).
- [22] J. K. Freericks and H. Monien, Europhysics Letters (EPL) **26**, 545 (1994).
- [23] J. F. Sherson, C. Weitenberg, M. Endres, M. Cheneau, I. Bloch, and S. Kuhr, Nature **467**, 68 (2010).
- [24] P. Degenfeld-Schonburg, E. del Valle, and M. J. Hartmann, Phys. Rev. A **85**, 013842 (2012).
- [25] K. J. Vahala, Nature **424**, 839 (2003).
- [26] T. M. Benson, S. V. Boriskina, P. Sewell, A. Vukovic, S. C. Greedy, and A. I. Nosich, Micro-optical resonators for microlasers and integrated optoelectronics, in *Frontiers in Planar Lightwave Circuit Technology*, edited by S. Janz, J. Ctyroky, and S. Tanev, pages 39–70, Dordrecht, 2006, Springer Netherlands.
- [27] G. Khitrova, H. M. Gibbs, M. Kira, S. W. Koch, and A. Scherer, Nature Physics **2**, 81 (2006).
- [28] P. Grangier, G. Reymond, and N. Schlosser, Fortschritte der Physik **48**, 859 (2000).
- [29] M. Bayindir, B. Temelkuran, and E. Ozbay, Phys. Rev. B **61**, R11855 (2000).
- [30] A. D. Greentree, C. Tahan, J. H. Cole, and L. C. L. Hollenberg, Nature Physics **2**, 856 (2006).
- [31] M. J. Hartmann, F. G. S. L. Brandão, and M. B. Plenio, Nature Physics **2**, 849 (2006).
- [32] D. G. Angelakis, M. F. Santos, and S. Bose, Phys. Rev. A **76**, 031805 (2007).
- [33] A. Imamoglu, H. Schmidt, G. Woods, and M. Deutsch, Phys. Rev. Lett. **79**, 1467 (1997).
- [34] P. Grangier, D. F. Walls, and K. M. Gheri, Phys. Rev. Lett. **81**, 2833 (1998).
- [35] K. M. Gheri, W. Alge, and P. Grangier, Phys. Rev. A **60**, R2673 (1999).
- [36] K. M. Birnbaum, A. Boca, R. Miller, A. D. Boozer, T. E. Northup, and H. J. Kimble, Nature **436**, 87 (2005).
- [37] N. Didier, S. Pugnetti, Y. M. Blanter, and R. Fazio, Phys. Rev. B **84**, 054503 (2011).
- [38] D. Hui, W. Gregor, S. Charles, B. Jacqueline, and Y. Yoshihisa, Science **298**, 199 (2002).
- [39] J. Kasprzak et al., Nature **443**, 409 (2006).
- [40]
- [41] A. Amo et al., Nature **457**, 291 (2009).
- [42] A. Amo et al., Nature Physics **5**, 805 (2009).
- [43] M. H. Devoret, A. Wallraff, and J. M. Martinis, Superconducting qubits: A short review, 2004, eprint: arXiv:cond-mat/0411174.
- [44] G. Burkard, R. H. Koch, and D. P. DiVincenzo, Phys. Rev. B **69**, 064503 (2004).
- [45] A. A. Houck, J. Koch, M. H. Devoret, S. M. Girvin, and R. J. Schoelkopf, Quantum Information Processing **8**, 105 (2009).
- [46] J. R. Friedman, V. Patel, W. Chen, S. K. Tolpygo, and J. E. Lukens, Nature **406**, 43 (2000).
- [47] van der Wal Caspar H. et al., Science **290**, 773 (2000).
- [48] J. M. Martinis, S. Nam, J. Aumentado, and C. Urbina, Phys. Rev. Lett. **89**, 117901

- (2002).
- [49] V. Bouchiat, D. Vion, P. Joyez, D. Esteve, and M. H. Devoret, *Physica Scripta* **T76**, 165 (1998).
- [50] Y. Nakamura, Y. A. Pashkin, and J. S. Tsai, *Nature* **398**, 786 (1999).
- [51] J. Clarke and F. K. Wilhelm, *Nature* **453**, 1031 (2008).
- [52] S. M. Girvin, M. H. Devoret, and R. J. Schoelkopf, *Physica Scripta* **T137**, 014012 (2009).
- [53] T. McIntosh, P. Pisarski, R. J. Gooding, and E. Zaremba, *Phys. Rev. A* **86**, 013623 (2012).
- [54] D. Yamamoto, A. Masaki, and I. Danshita, *Phys. Rev. B* **86**, 054516 (2012).
- [55] S. R. Hassan and L. de' Medici, *Phys. Rev. B* **81**, 035106 (2010).
- [56] M. Singh, S. Greschner, and T. Mishra, *Phys. Rev. A* **98**, 023615 (2018).
- [57] M. Singh, T. Mishra, R. V. Pai, and B. P. Das, *Phys. Rev. A* **90**, 013625 (2014).
- [58] K. G. Wilson, *Rev. Mod. Phys.* **47**, 773 (1975).
- [59] S. R. White, *Phys. Rev. Lett.* **69**, 2863 (1992).
- [60] U. Schollwöck, *Rev. Mod. Phys.* **77**, 259 (2005).
- [61] S. Östlund and S. Rommer, *Phys. Rev. Lett.* **75**, 3537 (1995).
- [62] U. Schollwöck, *Annals of Physics* **326**, 96 (2011).
- [63] S. Will, T. Best, U. Schneider, L. Hackermüller, D.-S. Lühmann, and I. Bloch, *Nature* **465**, 197 (2010).
- [64] M. J. Mark, E. Haller, K. Lauber, J. G. Danzl, A. J. Daley, and H.-C. Nägerl, *Phys. Rev. Lett.* **107**, 175301 (2011).
- [65] A. J. Daley and J. Simon, *Phys. Rev. A* **89**, 053619 (2014).
- [66] P. R. Johnson, E. Tiesinga, J. V. Porto, and C. J. Williams, *New Journal of Physics* **11**, 093022 (2009).
- [67] D. S. Petrov, *Phys. Rev. Lett.* **112**, 103201 (2014).
- [68] D. S. Petrov, *Phys. Rev. A* **90**, 021601 (2014).
- [69] B.-l. Chen, X.-b. Huang, S.-p. Kou, and Y. Zhang, *Phys. Rev. A* **78**, 043603 (2008).
- [70] J. Silva-Valencia and A. M. C. Souza, *Phys. Rev. A* **84**, 065601 (2011).
- [71] T. Sowiński, *Phys. Rev. A* **85**, 065601 (2012).
- [72] J. Silva-Valencia and A. M. C. Souza, *The European Physical Journal B* **85**, 161 (2012).
- [73] M. Singh, A. Dhar, T. Mishra, R. V. Pai, and B. P. Das, *Phys. Rev. A* **85**, 051604 (2012).
- [74] S. Ejima, F. Lange, H. Fehske, F. Gebhard, and K. z. Münster, *Phys. Rev. A* **88**, 063625 (2013).
- [75] T. Sowiński, *Open Physics* **12**, 473 (2014).
- [76] T. Sowiński, R. W. Chhajlany, O. Dutta, L. Tagliacozzo, and M. Lewenstein, *Phys. Rev. A* **92**, 043615 (2015).
- [77] A. J. Daley, J. M. Taylor, S. Diehl, M. Baranov, and P. Zoller, *Phys. Rev. Lett.* **102**, 040402 (2009).
- [78] B. Paredes et al., *Nature* **429**, 277 (2004).

## BIBLIOGRAPHY

---

- [79] M. A. Baranov, M. Dalmonte, G. Pupillo, and P. Zoller, *Chemical Reviews* **112**, 5012 (2012).
- [80] S. Baier et al., *Science* **352**, 201 (2016).
- [81] L. Chomaz et al., *Phys. Rev. X* **9**, 021012 (2019).
- [82] L. Tanzi et al., *Phys. Rev. Lett.* **122**, 130405 (2019).
- [83] F. Böttcher, J.-N. Schmidt, M. Wenzel, J. Hertkorn, M. Guo, T. Langen, and T. Pfau, *Phys. Rev. X* **9**, 011051 (2019).
- [84] C. Trefzger, C. Menotti, and M. Lewenstein, *Phys. Rev. Lett.* **103**, 035304 (2009).
- [85] A. Safavi-Naini, S. G. Söyler, G. Pupillo, H. R. Sadeghpour, and B. CapogrossoSansone, **15**, 013036 (2013).
- [86] A. Argüelles and L. Santos, *Phys. Rev. A* **75**, 053613 (2007).
- [87] M. Singh, S. Mondal, B. K. Sahoo, and T. Mishra, *Phys. Rev. A* **96**, 053604 (2017).
- [88] D. S. Hall, M. R. Matthews, J. R. Ensher, C. E. Wieman, and E. A. Cornell, *Phys. Rev. Lett.* **81**, 1539 (1998).
- [89] J. Catani, L. De Sarlo, G. Barontini, F. Minardi, and M. Inguscio, *Phys. Rev. A* **77**, 011603 (2008).
- [90] S. Trotzky et al., *Science* **319**, 295 (2008).
- [91] R. Jördens, N. Strohmaier, K. Günter, H. Moritz, and T. Esslinger, *Nature* **455**, 204 (2008).
- [92] A.-C. Voigt, M. Taglieber, L. Costa, T. Aoki, W. Wieser, T. W. Hänsch, and K. Dieckmann, *Phys. Rev. Lett.* **102**, 020405 (2009).
- [93] M. Endres et al., *Science* **334**, 200 (2011).
- [94] K. Günter, T. Stöferle, H. Moritz, M. Köhl, and T. Esslinger, *Phys. Rev. Lett.* **96**, 180402 (2006).
- [95] G. Roati, F. Riboli, G. Modugno, and M. Inguscio, *Phys. Rev. Lett.* **89**, 150403 (2002).
- [96] T. Best, S. Will, U. Schneider, L. Hackermüller, D. van Oosten, I. Bloch, and D.-S. Lühmann, *Phys. Rev. Lett.* **102**, 030408 (2009).
- [97] A. Richaud and V. Penna, *Condensed Matter* **5**, 2 (2020).
- [98] L. He, Y. Li, E. Altman, and W. Hofstetter, *Phys. Rev. A* **86**, 043620 (2012).
- [99] F. Hébert, G. G. Batrouni, X. Roy, and V. G. Rousseau, *Phys. Rev. B* **78**, 184505 (2008).
- [100] T. Mishra, R. V. Pai, and B. P. Das, *Phys. Rev. A* **76**, 013604 (2007).
- [101] T. Mishra, B. K. Sahoo, and R. V. Pai, *Phys. Rev. A* **78**, 013632 (2008).
- [102] T. Ozaki and T. Nikuni, *Journal of the Physical Society of Japan* **81**, 024001 (2012).
- [103] H. Pu and N. P. Bigelow, *Phys. Rev. Lett.* **80**, 1130 (1998).
- [104] A. Kuklov, N. Prokof'ev, and B. Svistunov, *Phys. Rev. Lett.* **92**, 050402 (2004).
- [105] L. Mathey, *Phys. Rev. B* **75**, 144510 (2007).
- [106] A. Isacsson, M.-C. Cha, K. Sengupta, and S. M. Girvin, *Phys. Rev. B* **72**, 184507 (2005).
- [107] S Sugawa, K Inaba, S Taie, R Yamazaki, M Yamashita, and Y Takahashi, *Nature Physics* **7**, 642 (2011).

- [108] H. Hara, H. Konishi, S. Nakajima, Y. Takasu, and Y. Takahashi, *Journal of the Physical Society of Japan* **83**, 014003 (2014).
- [109] S. Peil et al., *Phys. Rev. A* **67**, 051603 (2003).
- [110] J. Sebby-Strabley, M. Anderlini, P. S. Jessen, and J. V. Porto, *Phys. Rev. A* **73**, 033605 (2006).
- [111] M. Singh and T. Mishra, *Phys. Rev. A* **94**, 063610 (2016).
- [112] A. Dhar, T. Mishra, R. V. Pai, and B. P. Das, *Phys. Rev. A* **83**, 053621 (2011).
- [113] A. Dhar, M. Singh, R. V. Pai, and B. P. Das, *Phys. Rev. A* **84**, 033631 (2011).
- [114] A. Dhar, T. Mishra, M. Maji, R. V. Pai, S. Mukerjee, and A. Paramekanti, *Phys. Rev. B* **87**, 174501 (2013).
- [115] R. Roth and K. Burnett, *Phys. Rev. A* **68**, 023604 (2003).
- [116] F. Schmitt, M. Hild, and R. Roth, *Phys. Rev. A* **80**, 023621 (2009).
- [117] G. Roux, T. Barthel, I. P. McCulloch, C. Kollath, U. Schollwöck, and T. Giamarchi, *Phys. Rev. A* **78**, 023628 (2008).
- [118] P. Cheinet, S. Trotzky, M. Feld, U. Schnorrberger, M. Moreno-Cardoner, S. Fölling, and I. Bloch, *Phys. Rev. Lett.* **101**, 090404 (2008).
- [119] F. Grusdt, M. Höning, and M. Fleischhauer, *Phys. Rev. Lett.* **110**, 260405 (2013).
- [120] S. Nascimbène, Y.-A. Chen, M. Atala, M. Aidelsburger, S. Trotzky, B. Paredes, and I. Bloch, *Phys. Rev. Lett.* **108**, 205301 (2012).
- [121] E. Altman, W. Hofstetter, E. Demler, and M. D. Lukin, *New Journal of Physics* **5**, 113 (2003).
- [122] B.-L. Chen, S.-P. Kou, Y. Zhang, and S. Chen, *Phys. Rev. A* **81**, 053608 (2010).
- [123] I. Danshita, J. E. Williams, C. A. R. Sá de Melo, and C. W. Clark, *Phys. Rev. A* **76**, 043606 (2007).
- [124] Y.-C. Chen and M.-F. Yang, *Journal of Physics Communications* **1**, 035009 (2017).
- [125] B. Yang, H.-N. Dai, H. Sun, A. Reingruber, Z.-S. Yuan, and J.-W. Pan, *Phys. Rev. A* **96**, 011602 (2017).
- [126] M. Lewenstein, L. Santos, M. A. Baranov, and H. Fehrmann, *Phys. Rev. Lett.* **92**, 050401 (2004).
- [127] P. Donohue, M. Tsuchiizu, T. Giamarchi, and Y. Suzumura, *Phys. Rev. B* **63**, 045121 (2001).
- [128] A. E. Feiguin and M. P. A. Fisher, *Phys. Rev. B* **83**, 115104 (2011).
- [129] F. m. c. Crépin, N. Laflorencie, G. Roux, and P. Simon, *Phys. Rev. B* **84**, 054517 (2011).
- [130] M. Okumura, S. Yamada, M. Machida, and H. Aoki, *Phys. Rev. A* **83**, 031606 (2011).
- [131] C. Degli Esposti Boschi, A. Montorsi, and M. Roncaglia, *Phys. Rev. B* **94**, 085119 (2016).
- [132] W.-L. Liu, T.-Z. Yuan, Z. Lin, and W. Yan, *Chinese Physics B* **28**, 020303 (2019).
- [133] T. Giamarchi, *Quantum physics in one dimension*, volume 121, Clarendon press, 2003.

## BIBLIOGRAPHY

---

- [134] M. Fabrizio, A. Parola, and E. Tosatti, *Phys. Rev. B* **46**, 3159 (1992).
- [135] N. Nagaosa, *Solid State Communications* **94**, 495 (1995).
- [136] H. J. Schulz, *Phys. Rev. B* **53**, R2959 (1996).
- [137] L. Balents and M. P. A. Fisher, *Phys. Rev. B* **53**, 12133 (1996).
- [138] R. M. Noack, S. R. White, and D. J. Scalapino, *Physica C: Superconductivity* **270**, 281 (1996).
- [139] S. R. White, I. Affleck, and D. J. Scalapino, *Phys. Rev. B* **65**, 165122 (2002).
- [140] P. Donohue and T. Giamarchi, *Phys. Rev. B* **63**, 180508 (2001).
- [141] M. S. Luthra, T. Mishra, R. V. Pai, and B. P. Das, *Phys. Rev. B* **78**, 165104 (2008).
- [142] E. Orignac and T. Giamarchi, *Phys. Rev. B* **64**, 144515 (2001).
- [143] M. A. Cazalilla, A. F. Ho, and T. Giamarchi, *New Journal of Physics* **8**, 158 (2006).
- [144] M. A. Cazalilla, R. Citro, T. Giamarchi, E. Orignac, and M. Rigol, *Rev. Mod. Phys.* **83**, 1405 (2011).
- [145] A. Dhar, M. Maji, T. Mishra, R. V. Pai, S. Mukerjee, and A. Paramekanti, *Phys. Rev. A* **85**, 041602 (2012).
- [146] A. Dhar, T. Mishra, R. V. Pai, S. Mukerjee, and B. P. Das, *Phys. Rev. A* **88**, 053625 (2013).
- [147] T. Mishra, R. V. Pai, and S. Mukerjee, *Phys. Rev. A* **89**, 013615 (2014).
- [148] T. Mishra, R. V. Pai, S. Mukerjee, and A. Paramekanti, *Phys. Rev. B* **87**, 174504 (2013).
- [149] A. Petrescu and K. Le Hur, *Phys. Rev. Lett.* **111**, 150601 (2013).
- [150] M. P. Zaletel, R. S. K. Mong, and F. Pollmann, *Journal of Statistical Mechanics: Theory and Experiment* **2014**, P10007 (2014).
- [151] W. S. Cole, S. Zhang, A. Paramekanti, and N. Trivedi, *Phys. Rev. Lett.* **109**, 085302 (2012).
- [152] A. W. N. Ashcroft, N. Mermin, N. Mermin, and B. P. Company, *Solid State Physics*, HRW international editions, Holt, Rinehart and Winston, 1976.
- [153] J. P. Covey et al., *Nature communications* **7**, 11279 (2016).
- [154] D. van Oosten, P. van der Straten, and H. T. C. Stoof, *Phys. Rev. A* **63**, 053601 (2001).
- [155] O. Firstenberg, T. Peyronel, Q.-Y. Liang, A. V. Gorshkov, M. D. Lukin, and V. Vuletic, *Nature* **502**, 71 (2013).
- [156] Q.-Y. Liang et al., *Science* **359**, 783 (2018).
- [157] N. Rivera, G. Rosolen, J. D. Joannopoulos, I. Kaminer, and M. Soljacic, *Proceedings of the National Academy of Sciences* **114**, 13607 (2017).
- [158] J. C. F. Matthews, A. Politi, A. Stefanov, and J. L. O'Brien, *Nature Photonics* **3**, 346 (2009).
- [159] N. Matsuda and H. Takesue, *Nanophotonics* **5**, 440 (2016).
- [160] E. Pomarico et al., *New Journal of Physics* **11**, 113042 (2009).
- [161] F. Clausen, C. and Bussi eres, A. Tiranov, H. Herrmann, C. Silberhorn, W. Sohler, M. Afzelius, and N. Gisin, *New Journal of Physics* **16**, 093058 (2014).
- [162] P.-J. Tsai and Y.-C. Chen, *Quantum Science and Technology* **3**, 034005 (2018).

- [163] A. Vepsäläinen, S. Danilin, and G. S. Paraoanu, *Science Advances* **5**, eaau5999 (2019).
- [164] D. E. Chang, V. Vuletic, and M. D. Lukin, *Nature Photonics* **8**, 685 (2014).
- [165] M. J. Hartmann, **18**, 104005 (2016).
- [166] A. Wallraff et al., *Nature* **431**, 162 (2004).
- [167] M. J. Hartmann, F. G. Brandao, and M. B. Plenio, *Nature Physics* **2**, 849 (2006).
- [168] M. I. Makin, J. H. Cole, C. Tahan, L. C. L. Hollenberg, and A. D. Greentree, *Phys. Rev. A* **77**, 053819 (2008).
- [169] A. Mering, M. Fleischhauer, P. A. Ivanov, and K. Singer, *Phys. Rev. A* **80**, 053821 (2009).
- [170] S. Schmidt and G. Blatter, *Phys. Rev. Lett.* **103**, 086403 (2009).
- [171] J. Koch and K. Le Hur, *Phys. Rev. A* **80**, 023811 (2009).
- [172] M. Hohenadler, M. Aichhorn, L. Pollet, and S. Schmidt, *Phys. Rev. A* **85**, 013810 (2012).
- [173] K. Toyoda, Y. Matsuno, A. Noguchi, S. Haze, and S. Urabe, *Phys. Rev. Lett.* **111**, 160501 (2013).
- [174] L.-L. Zheng, K.-M. Li, X.-Y. Lü, and Y. Wu, *Phys. Rev. A* **96**, 053809 (2017).
- [175] J. Zhang and Y. Jiang, **27**, 035203 (2017).
- [176] C. Noh and D. G. Angelakis, **80**, 016401 (2016).
- [177] M. Alexanian, *Phys. Rev. A* **83**, 023814 (2011).
- [178] I. Pietikäinen, S. Danilin, K. S. Kumar, A. Vepsäläinen, D. S. Golubev, J. Tuorila, and G. S. Paraoanu, *Phys. Rev. B* **96**, 020501 (2017).
- [179] I. Pietikäinen, S. Danilin, K. S. Kumar, J. Tuorila, and G. S. Paraoanu, *Journal of Low Temperature Physics* **191**, 354 (2018).
- [180] Y.-H. Luo et al., *Phys. Rev. Lett.* **123**, 070505 (2019).
- [181] X.-M. Hu, C. Zhang, B.-H. Liu, Y.-F. Huang, C.-F. Li, and G.-C. Guo, *arXiv preprint arXiv:1904.12249* (2019).
- [182] I. Pietikäinen, J. Tuorila, D. S. Golubev, and G. S. Paraoanu, *Phys. Rev. A* **99**, 063828 (2019).
- [183] S. Schmidt and J. Koch, *Annalen der Physik* **525**, 395 (2013).
- [184] J. A. Schreier et al., *Phys. Rev. B* **77**, 180502 (2008).
- [185] Y. Chen et al., *Phys. Rev. Lett.* **113**, 220502 (2014).
- [186] M. Baur et al., *Phys. Rev. Lett.* **102**, 243602 (2009).
- [187] R. Bianchetti et al., *Phys. Rev. Lett.* **105**, 223601 (2010).
- [188] S. B. Prasad and A. M. Martin, *Scientific reports* **8**, 16253 (2018).
- [189] T. Mishra, S. Greschner, and L. Santos, *Phys. Rev. A* **91**, 043614 (2015).
- [190] S. Mondal, S. Greschner, and T. Mishra, *Phys. Rev. A* **100**, 013627 (2019).
- [191] S.-J. Gu, *Int. J. Mod. Phys. B* **24**, 4371 (2010).
- [192] C. E. Kuklewicz, F. N. C. Wong, and J. H. Shapiro, *Phys. Rev. Lett.* **97**, 223601 (2006).
- [193] X.-H. Bao, Y. Qian, J. Yang, H. Zhang, Z.-B. Chen, T. Yang, and J.-W. Pan, *Phys. Rev. Lett.* **101**, 190501 (2008).

## BIBLIOGRAPHY

---

- [194] F. Wolfgramm, X. Xing, A. Cerè, A. Predojević, A. M. Steinberg, and M. W. Mitchell, *Optics Express* **16**, 18145 (2008).
- [195] A. Haase, N. Piro, J. Eschner, and M. W. Mitchell, *Optics Letters* **34**, 55 (2009).
- [196] S. Greschner, M. Piraud, F. Heidrich-Meisner, I. P. McCulloch, U. Schollwöck, and T. Vekua, *Phys. Rev. Lett.* **115**, 190402 (2015).
- [197] M. Piraud, F. Heidrich-Meisner, I. P. McCulloch, S. Greschner, T. Vekua, and U. Schollwöck, *Phys. Rev. B* **91**, 140406 (2015).
- [198] S. Greschner, M. Piraud, F. Heidrich-Meisner, I. P. McCulloch, U. Schollwöck, and T. Vekua, *Phys. Rev. A* **94**, 063628 (2016).



## Curriculum Vitae

### Address

Home Address : Habra, North 24 Parganas, West Bengal, India, 743271

Phone : +91 8471854012

Email : sayan12@iitg.ac.in

### Personal profile

Date of Birth : 07/10/1991

Place of Birth : Behala

Gender : Male

Marital Status : Unmarried

Nationality : Indian

Language : Bengali, English, Hindi

### Education

B.Sc (2010-2013) : Barasat Government College, West Bengal State University

M.Sc (2013-2015) : University of Kalyani

Ph.D (Enrolled in 2016) : Indian Institute of Technology Guwahati

Earned the Senior Research Fellowship in 2018 by Indian Institute of Technology Guwahati.

Graduate Aptitude Test in Engineering (GATE) qualified in 2016.